Modélisation des relations microstructure - propriétés de matériaux réfractaire : approche micromécanique par la méthode des éléments discrets

Truong Thi Nguyen

To cite this version:

Truong Thi Nguyen. Modélisation des relations microstructure - propriétés de matériaux réfractaire : approche micromécanique par la méthode des éléments discrets. Matériaux. Université de Limoges, 2019. Français. NNT : 2019LIMO0089 . tel-02464585v1

HAL Id: tel-02464585
https://theses.hal.science/tel-02464585v1

Submitted on 3 Feb 2020 (v1), last revised 3 Feb 2020 (v2)

UNIVERSITÉ DE LIMOGES

ÉCOLE DOCTORALE SIMME n°609

Institut de Recherche sur les Céramiques

Année : 2019 Thèse N °X

Thesis

submitted for the degree of

DOCTOR OF PHILOSOPHY
OF THE UNIVERSITY OF LIMOGES

Discipline: Ceramic Materials and Surface Treatment

Presented by

Truong Thi NGUYEN

03 december 2019

Numerical modeling of microstructure-properties relationships of refractories: micro-mechanical approach with the discrete element method

Supervised by: Marc HUGER and Damien ANDRÉ

JURY:

President
Professor Nicolas SCHMITT, Head of the testing lab, LMT de Cachan, France

Reviewers
Professor Ivan IORDANOFF, Directeur Général Adjoint Recherche et Innovation des Arts et Métiers, i2M Bordeaux, France
Professor Paulo B. LOURENCO, Head of the Structural Group, University of Minho, Portugal

Examiners
Professor Marc HUGER, IRCER UMR 7315, University of Limoges, France
Doctor Damien ANDRÉ, Assistant professor, IRCER UMR 7315, University of Limoges, France
Doctor Sido SINNEMA, Knowledge Group Leader at TataSteel IJmuiden, Netherlands

À ma famille

Acknowledgments

The present work has been accomplished in the Institute of Research for Ceramics (IRCER, formerly SPCTS), Limoges, France. I gratefully acknowledge the Nouvelle-Aquitaine Region (France) for their financial support.

This PhD thesis was realized in the framework of FIRE project D (Federation for International Refractory Research and Education) entitled: “Refractories with enhanced flexibility for thermal shock” through collaboration with RWTH Aachen University (Germany), Montanuniversität Leoben (Austria), Pprime institute of Poitiers (France), Tatasteel (Netherland). I would like to express my thankfulness for all members of the project.

First and foremost, i would like to express my utmost gratitude to my supervisors, Professor Marc Huger and Doctor Damien André (IRCER, Limoges). This study would not have been possible without their great guidance. I want to express a deep sense of thanks to Professor Marc Huger for giving me the opportunity to undertake this research, for his availability and his great advices during my work. His high requirements and his constructive comments have helped me a lot during the writing of the thesis dissertation. I would like to express my deep gratitude to my supervisor Damien André who helps me discover the Discrete Element Method (DEM). His expertise, his guidance and encouragement have been very important for my work.

I also acknowledge Doctor Nicolas Tessier-Doyen for providing his experimental results and for scientific helpful discussions. His experimental results have been essential to evaluate my numerical approach.

I would like to express my sincere thanks to the jury members Professor Nicolas Schmitt, Professor Ivan Iordanoff, Professor Paulo B. Lourenço and Doctor Sido Sinnema for their efforts and wisdom.

I would like to thank also all the staff of the IRCER laboratory for their help. These years of PhD wouldn’t be the same without my friends and colleagues with whom I shared memorable moments: Guy Oum, Imad Khlifi, Siham Oummadi, Andrzej Warchał, Moustapha Coulibaly, Farid Khosrowpour, Robert Kaczmarek, Fateh Tehrani, Justine Tarabeux... Thanks to all of you for those precious memories!

Last but not least, I would like to thank my parents, my brother, all members of my family and my fiancé Thanh-Hang Nguyen, for their moral support and their love.

Contents

List of Figures

List of Tables

General introduction

Thanks to their specific properties, refractories are essential for several industries such as steel, cement and glass processing. In these industries, refractories face severe working environments such as extra high temperatures, brutal thermal shocks, mechanical loadings and corrosion. The present work deals specifically with the thermal shock resistance of refractories which is not easy to characterized and managed. However, this property is crucial to increase the lifetime of refractories in many applications. Thanks to previous experimental works, it was demonstrated that the thermal shock resistance is closely related to the crack growth resistance of such materials. More specifically, in several cases, the thermal shock resistance of refractories could be increased by properly introducing micro-cracks within their microstructure during elaboration. In fact, those preexisting micro-cracks allow to increase fracture energy, thus, limit crack propagation. Depending on micro-cracking level, the mechanical behavior could be tuned from pure elastic to a so-called *nonlinear behavior* (the relation between stress and strain is no longer proportional). This empirical knowledge offers a great interest to improve thermal shock resistance of refractories by a better design of their microstructure. However, up to now, the application of such concept has not been fully understood and is not predictable.

In order to investigate the relationships between microstructure and thermomechanical properties of refractories, several experimental works were already carried out at the Institute of Research for Ceramics (IRCER, formerly SPCTS). In these researches, *model materials* with simplified microstructure, namely glass-alumina composites, were investigated. Despite their simplified microstructure, these model materials exhibit behaviors close to that of the industrial refractories. In particular, the key aspect of such simplified material is to play with the thermal expansion mismatch between its constituents in order to tune the micro-crack network within its microstructure. This micros-crack network can be modulated by the choice of different constituents and by the thermal treatment involved in processing.

In this context, the present research is a first step of a long term objective: development of a reliable modeling platform to give insights for experimental approach in order to enhance thermal shock resistance of industrial refractories. Therefore, the developed modeling platform must be able to take into account complex damage phenomena of heterogeneous material due to thermal expansion mismatch during different thermal treatments. For this purpose, the Discrete Element Method (DEM) is used in the present study as a promising way to model the damage phenomena at microscopic scale.

Thanks to the spectacular development of computer technology, this kind of numerical approach is used extensively in order to solve complex practical problems in science and engineering.

The present PhD dissertation is structured in 3 parts, each part includes 2 chapters.

Part A is dedicated to a literature review of thermal shock resistance of refractories and numerical method for damage modeling. Firstly, the classical analytical approaches of thermal shock resistance are briefly presented. The crack growth resistance and *nonlinear mechanical behavior* of refractories are then discussed. Thermomechanical behavior of 2 typical refractories dedicated to thermal shock are then presented in order to highlight the relation between initial thermal damages and thermal shock resistance. Secondly, the motivation of the so-called *model materials* and selection of two specific materials are discussed. In addition, the Hashin&Strickman analytical model is introduced as a reference for experimental and numerical results for undamaged material. Finally, the selection of numerical methods for damage modeling is presented as a promising support to experimental approach. In the present research, the DEM has been selected for its significant advantages in damage modeling, in comparison with continuous methods.

In Part B, the development of the discrete element platform, *GranOO* is presented. Firstly, a general review of GranOO is introduced: the architecture of DEM platform, the key steps of DEM simulation and the contact model. In addition, the new developments of stress computation associated with DEM simulation are also detailed. Secondly, a direct calibration method of local input parameters required by DEM is proposed in order to remove classical trial-and-error calibration, which is tedious and time-consuming. The proposed direct calibration method and virial stress concept are then applied to conduct quantitative DEM simulation of thermomechanical test. In addition, the accuracy of virial stress concept is examined through a confrontation of thermal stress between DEM and Finite Element Method (FEM) computations.

In part C, quantitative simulations of cooling stage are carried out in order to investigate the influence of thermal damage due to thermal expansion mismatch on apparent behavior of *model materials*. Firstly, the main steps and assumptions of cooling simulation are detailed. Especially, numerical process to create *Statistical Volume Element* of heterogeneous material is explained. Secondly, the DEM results are confronted with experimental data and Hashin&Strickman model.

The evolutions of Young's modulus and coefficient of thermal expansion as functions of temperature are analyzed in order to highlight the influence of thermal damages. In addition, qualitative DEM results of nonlinear tensile behavior on model materials are discussed in comparison with experimental observations reported in literature.

Finally, this dissertation will be closed by general conclusions and perspectives.

Part A

State of the art

Introduction

For a long time, refractory materials have been extensively used in many industrial areas which have severe working environments at extra high temperature. Therefore, the main requirements of refractory materials are to resist to thermal shock and to sustain significant mechanical loading and corrosion.

In this context, the knowledge concerning the improvement of thermal shock resistance of refractory materials is highly requested to enhance their lifetime. For a long time, the thermal shock resistance of refractories has been intensively studied, but it has not been fully explored. Several experimental researches have reported that thermal shock resistance could be improved by introducing appropriately thermal expansion mismatch between constituents of refractory materials. The occurrence of damages due to thermal expansion mismatch could make mechanical behavior of refractory materials deviate from linear elastic to nonlinear behavior.

The improvement of thermal shock resistance of refractories requires a better understanding of the relationships between the microstructure and the associated thermomechanical properties at macroscopic scale. However, this is not an easy task due to the complex microstructures of industrial refractory materials. Therefore, several researches have investigated this problematic by considering model materials with simplified microstructure, namely glass-alumina composites, with thermal expansion mismatch [TD03, Jol06]. In order to reinforce these experimental results, some numerical approaches have been carried out. However, up to now, numerical researches have been mainly based on continuous approaches, which are still not compatible to describe physical phenomena that involves high amount of discontinuity.

Part A is structured in 2 chapters. The first chapter is dedicated to state of the art of relationships between thermal damages and thermal shock resistance of refractory materials. The second chapter is dedicated to the selection of numerical approach to model appropriately the considered relationships.

Chapter A.I

Thermal shock resistance of refractory materials

A.I.1 Influence of thermal damages on thermal shock resistance of refractory materials

A.I.1.1 Thermal shock resistance of refractory materials

A.I.1.1.a Definition of thermal shock resistance

Thermal shock resistance is the ability of the material to withstand thermal stresses with minimal cracking [Bax04]. Among several approaches in the literature, the energetic approach, introduced by Hasselman, has been widely used to characterize thermal shock resistance of materials [Has63, Has69]. In Hasselman's approach, it was supposed that the material is initially damaged and the thermal shock causes the propagation of existing cracks in unstable or stable ways. In this approach, crack propagation was assumed to be managed by the minimization of total energy of the system. According to Hasselman, the total energy (W_{total}) is the sum of elastic energy plus the surface energy of the cracks [Has69].

$$W_{total} = W_{elastic} + W_{surface} \tag{A.I.1}$$

where: $W_{elastic} = \frac{1}{2}\frac{\sigma^2}{E}$ is elastic energy, σ is stress, E is Young's modulus; $W_{surface}$ is surface energy which corresponds to energy to create crack surfaces of the system.

Hasselman proposed two parameters to characterize the thermal shock resistance of material, i.e. R'''' and R_{st} which are given by equations A.I.2 and

A.I.3. [Has63, Has69]

$$R'''' = \frac{E.\gamma_s}{\sigma_c^2} \tag{A.I.2}$$

$$R_{st} = \sqrt{\frac{\gamma_s}{E.\alpha^2}} \tag{A.I.3}$$

where γ_s $(J.m^{-2})$ is surface energy of the material, σ_c (MPa) is material strength, E (GPa) is Young's modulus and α (K^{-1}) is Coefficient of Thermal Expansion (CTE). R'''' (m) is the thermal shock damage resistance parameter which corresponds to the case of small initial cracks. By contrast, R_{st} $(K.\sqrt{m})$ is a quasi-stable crack growth resistance parameter which characterizes thermal shock resistance of materials with large initial cracks.

According to equations A.I.2 and A.I.3, it can be noticed that both R'''' and R_{st} depend on Young's modulus and surface energy. By using a simple approximations of elastic energy, $E.\alpha^2$ is considered to be proportional to $\frac{\sigma^2}{E}$. Thus, both R'''' and R_{st} are inversely proportional to $\frac{\sigma^2}{E}$, which corresponds to the stored elastic strain energy [PB99]. This energy can be considered as a resistance for crack growth whether the thermal shock damage is either kinetic or quasi-static.

In equations A.I.2 and A.I.3, surface energy γ_s is considered at microscopic scale [Has63, Has69]. In order to apply Hasselman's energetic approach to heterogeneous materials, it was proposed to compute thermal shock resistance by the fracture energy at macroscopic scale, namely work-of-fracture γ_{WOF} [Nak65]. More specifically, the fracture energy γ_{WOF} is the energy consumed to propagate a crack through a sample. The value of γ_{WOF} is calculated from the total energy (W) to propagate the crack and the area A as follows:

$$\gamma_{WOF} = \frac{W}{2A} \tag{A.I.4}$$

Hence, several authors [LCH74, Nak65] suggested to use this fracture energy in the Hasseman's energetic approach:

$$R'''' = \frac{E.\gamma_{WOF}}{\sigma_c^2} \tag{A.I.5}$$

$$R_{st} = \sqrt{\frac{\gamma_{WOF}}{E.\alpha^2}} \tag{A.I.6}$$

An other important remark on Hasselman's approach is that thermal shock damage resistance parameter decreases as strength increases. In other words, a high strength could make refractories more sensitive to thermal shock damage. For this reason, according to specific purposes, industrials need to privilege thermal shock resistance of refractories or their strength and to make a best compromise between them.

A.I.1.1.b R-curve approach

This paragraph explains the relation between thermal damage and thermal shock resistance by introducing the R-curve concept. Indeed, it has been observed in several researches that in some cases, refractories exhibit an increasing crack propagation resistance when the crack length increases [HJ77, ALS81]. This behavior is due to energy-absorbing phenomena occurring around the cracks and demanding more energy for crack propagations [Rit88, Bra81]. Such a phenomena could be described by R-curve behavior which was first proposed by Irwin and Kies in 1954 [IK54]. As a remark, the R-curve depends on the sample volume, the depth and location of the crack initially introduced, the testing conditions and the evaluation technique [MS88].

The R-curve measurement consists in determining the crack propagation resistance (or fracture toughness) as a function of the crack extension Δa. Two typical kinds of R-curves have been identified in the literature (Fig. A.I.1).

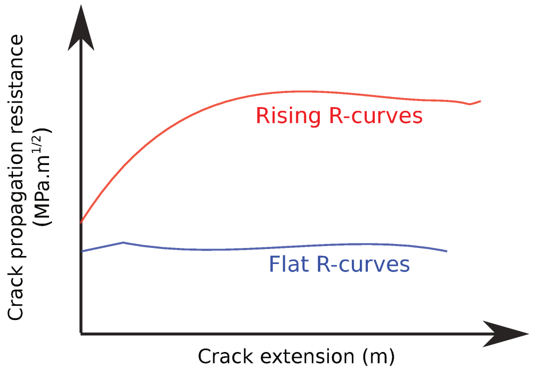

Fig. A.I.1: Two typical R-curves

The first one, named flat R-curves, corresponds to brittle linear elastic materials. In the flat R-curves, R remains constant during crack extensions. The second one, named rising R-curves, is often observed for refractories. In the rising R-curves, when crack extends, it gets more difficult for crack to grow since the total energy release rate becomes higher. This phenomenon could lead to a better thermal shock resistance of refractory before its failure and generate a nonlinear mechanical behavior. This nonlinear behavior has been associated to the improvement of thermal shock resistance in the late 1970s [GGS78, Gog93].

A.I.1.1.c Nonlinear mechanical behavior of refractories associated to thermal shock resistance

Generally, non-damaged refractories exhibit a linear elastic mechanical behavior which is resulting from the behaviors of its constituents. However, in some cases, these materials can advantageously exhibit complex nonlinear mechanical behaviors that result from the interactions between the different phases that compose their microstructure. This kind of nonlinear behavior has been investigated in many researches by using experimental approaches [Hug92, GK07, GB11, Bel15]. Nonlinear mechanical behavior of specific refractories could be characterized by a low stress-to-rupture, a high strain-to-rupture and a high irreversible strain (Fig. A.I.2). Consequently, according to the R-curves concept and Hasselman's definition of thermal shock resistances (equations A.I.2 and A.I.3), this nonlinear behavior could lead to a better thermal shock resistance which is key property of refractories.

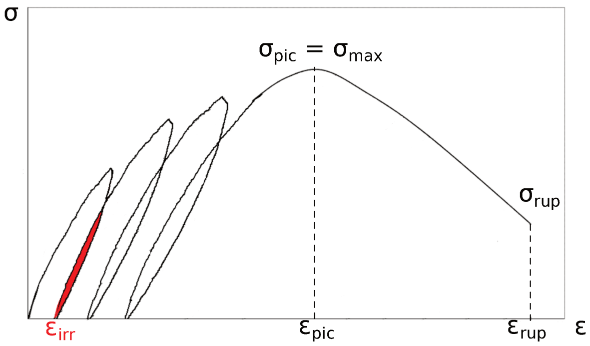

Fig. A.I.2: Nonlinear behavior of refractories obtained by tensile test

A.I.1.2 Thermal stresses and associated damages

Thermal stress phenomena has been intensively investigated since it exhibits a very important influences on the behaviors of refractories. The thermal stress could be generated by different possible origins.

The first possible origin is the mechanical restraint that prevents free expansion of a homogeneous, isotropic material. For 2D slab with uniform temperature change, the thermal stress could be computed by Eq. A.I.7 [Kin55].

$$\sigma = -\frac{E.\alpha.\Delta T}{1-\nu} \tag{A.I.7}$$

where: E is Young's modulus, α is CTE, ν is Poisson ratio of material and ΔT is temperature change.

Secondly, the thermal stress could be generated by the thermal expansion mismatch between different constituents of heterogeneous material and/or by anisotropic thermal expansion of homogeneous material [GK07]. These phenomena have been investigated in several researches by considering a simplified composite material that contains only two constituents [TD03, Jol06]. Generally, for ceramic materials, tensile strength is much lower than compressive strength. Thus, the damages are mainly generated due to tensile stresses. In the case of a two-phases material composed of a matrix (m) and spherical inclusions (p), during a uniform cooling stage, there are two configurations that cause the damages (Fig. A.I.3):

- $\alpha_m > \alpha_p$: the inclusion contracts less than the matrix and therefore prevents the free shrinkage of the matrix. Thus, the matrix is subjected to radial compressive stresses and orthoradial (circumferential) tensile stresses (Fig. A.I.3(a)). The increase of circumferential tensile stress leads to radial micro cracking;

- $\alpha_m < \alpha_p$: the inclusions contracts more than the matrix. Thus, a debonding can occur at the interface since the matrix is subjected to radial tensile stresses (Fig. A.I.3(b)). The interfacial gap can be enlarged due to the increase of thermal expansion mismatch.

Thirdly, thermal shock could be also an origin of thermal stresses. It may occur under specific conditions such as the presence of severe thermal gradient resulting from sudden temperature change at the surface of object.

In reality, thermal stress could be generated by a complex combination of the possible cases presented above. Generally, refractories could be considered, at macroscopic scale, as a homogeneous media. However, at microscopic scale, refractories involve sophisticated microstructures that mix several phases. Hence, the heterogeneity at microscopic scale has important effects on apparent properties at macroscopic scale of refractories. In the next section, thermomechanical behaviors of typical refractories will be presented in order to clarify the influence of their microstructures.

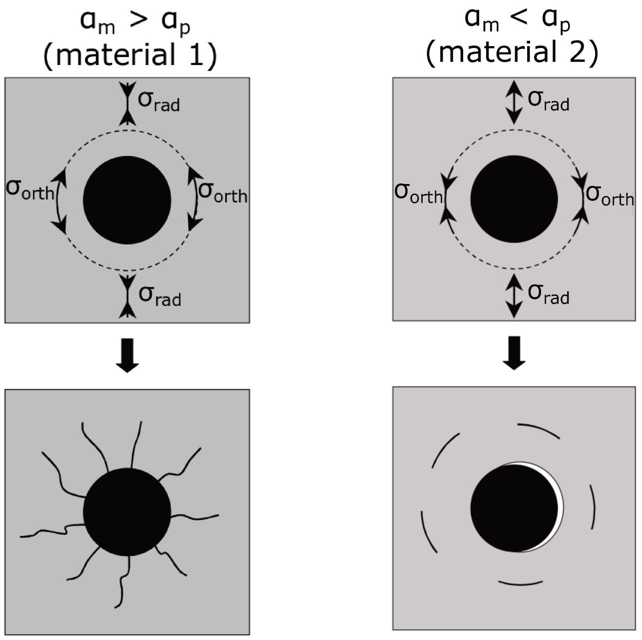

(a) Radial microcrack

(b) Debonding at interface

Fig. A.I.3: 2D illustration of damages due to thermal expansion mismatch during cooling [GK07]

A.I.2 Thermomechanical behaviors of 2 typical refractories dedicated to thermal shock

A.I.2.1 Magnesia-spinel refractories

Nowadays, magnesia-based refractories have been widely used in industries for their high thermal shock resistance and durability. In the past, thanks to empirical knowledges, it appeared that thermal shock resistance of magnesia brick is increased by the addition of 9-30% of magnesium aluminate spinel ($MgAl_2O_4$). The so-called magnesia-spinel refractories have been intensively investigated in order to understand why the thermal shock resistance increases and how to take advantage of this phenomenon. Then, it has been proved that the thermal expansion mismatch between magnesia (13-15$\cdot 10^{-6}$ K^{-1}) and spinel (8-9$\cdot 10^{-6}$ K^{-1}), causing microcracks around spinel inclusions, was one of the main reason of the raise of thermal shock resistance [ARRW02, AW03].

In order to understand better this phenomenon, Grasset-Bourdel studied materials which contained only magnesia and spinel [GB11]. In this cited research, the results of tensile and wedge splitting tests highlighted that the increase of spinel content improved the thermal shock resistance parameter R_{st} (Fig. A.I.4).

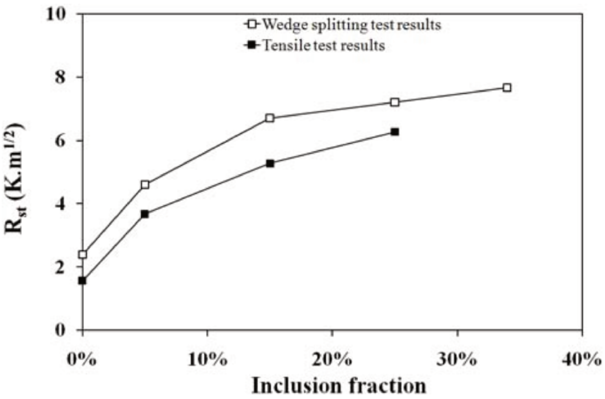

Fig. A.I.4: Influence of spinel content on thermal shock resistance parameter R_{st} of magnesia spinel refractory, taken from [GB11]

Fig. A.I.4 shows that the spinel addition allowed to increase progressively the thermal shock resistance. More quantitatively, R_{st} increased about 3 times with 35 wt.% of spinel inclusions. The increase of thermal shock resistance could be explained by considering the influence of spinel content on thermomechanical properties of magnesia-spinel refractory (Fig. A.I.5). As previously presented in Sect. A.I.1, for heterogeneous materials, thermal shock resistance R_{st} depends on work-of-fracture γ_{WOF}, Young's modulus E and thermal expansion coefficient α as follows:

$$R_{st} = \sqrt{\frac{\gamma_{WOF}}{E.\alpha^2}} \tag{A.I.8}$$

The first explanation is that the spinel addition allowed to increase work-of-fracture γ_{WOF} (Fig. A.I.5(a)). In this figure, ${}^{S}G'_f$ and ${}^{v}G'_f$ are related to the work-of-fracture γ_{WOF}, obtained by wedge spiting test and tensile test, respectively [GB11]. These results reported that with only 5 wt.% of spinel inclusions, the increase of work-of-fracture was around 65% (Fig. A.I.5(a)).

The second explanation is the decrease of Young's modulus and thermal expansion coefficient due to the increase of spinel content (Fig. A.I.5(b) and A.I.5(c)). Indeed, only 5 wt. % of spinel inclusion could divide the Young's modulus by two, in comparison with analytical HS model (Fig. A.I.5(b), the used analytical model will be explained hereafter, in paragraph A.I.3.3). Regarding the thermal expansion coefficient, the experimental values after thermal treatment was lower than the analytical HS model (Fig. A.I.5(c)). As a remark, the analytical model does not take into account thermal damages. Therefore, the discrepancy between experimental measurement and analytical model allowed to recognize the influence of thermal damages on thermomechanical properties of materials.

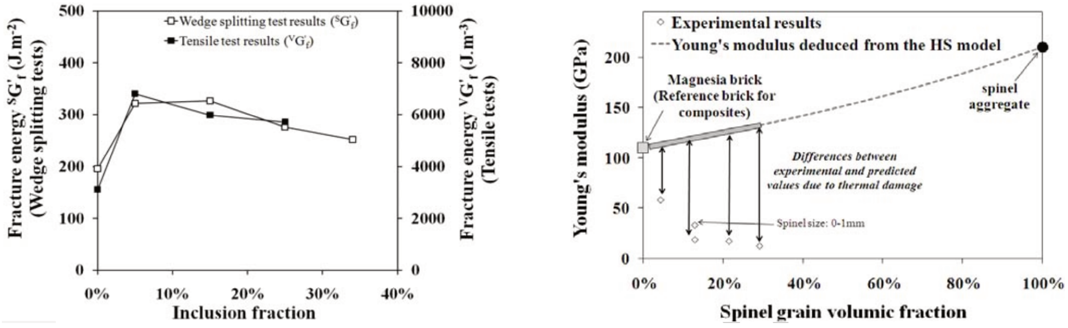

(a) Evolution of fracture energy (b) Evolution of Young's modulus

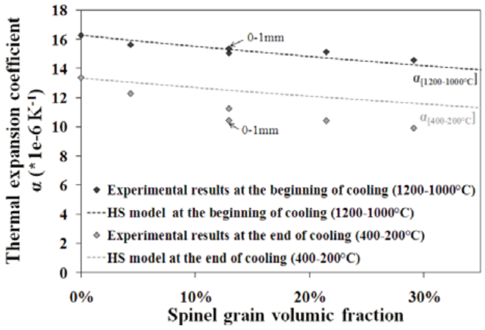

(c) Thermal expansion coefficient

Fig. A.I.5: Influence of spinel content on thermomechanical behavior of magnesia-spinel composites, taken from [GB11]

As presented before, the increase of thermal shock resistance of refractory materials has close relationship with nonlinear mechanical behavior due to thermal damages. In Fig. A.I.6, the stress-strain curves show that the increase of spinel content could promote the development of nonlinear behavior and residual strain. Moreover, tensile strength and Young's modulus decreased as spinel content increased.

The experimental results reported by Grasset-Bourdel showed a great interest to manage the microstructure of refractory materials in order to improve their thermal shock resistances.

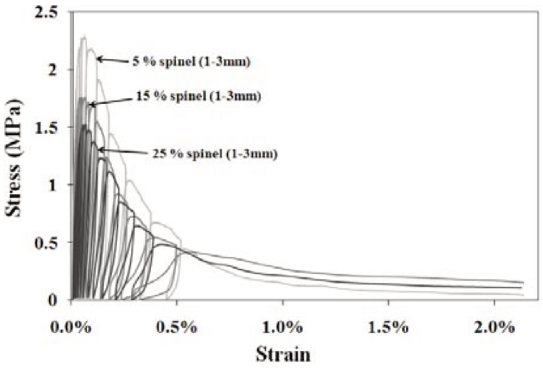

Fig. A.I.6: Nonlinear tensile behaviors obtained with different magnesia-spinel composites [GK07]

A.I.2.2 Andalusite-based refractories

For a long time, refractory concretes with andalusite aggregates has been extensively used in industries for its good thermal shocks resistance. This kind of material contains cement matrix and andalusite aggregate. Andalusite is an aluminium nesosilicate mineral with the chemical formula Al_2SiO_5. At high temperature, andalusite is transformed into mullite, which is well recognized for its good thermal shock resistance and creep resistance. Several researches have reported that such type of refractory has atypical behaviors at high temperature [Roo06, YF06].

In the research of Ghassemi Kakroudi, the relationships between microstructure and mechanical behavior of this refractory concrete has been investigated [GK07]. In order to investigate the nonlinear behavior of the considered material, uniaxial tensile tests at room temperature were carried out. More specifically, the considered refractory concrete was treated by thermal cycles at different temperatures and then, the thermally damaged samples were subjected to tensile test at room temperature. The obtained results are reported in Fig. A.I.7.

The obtained stress-strain curves reveal significant decrease of Young's modulus and development of nonlinear behavior when temperatures of thermal cycles increased. This could be explained by the fact that thermal damages are generated more as the temperature of thermal treatment increases. More quantitatively, Fig. A.I.7 shows that the Young's modulus decreases from 68 GPa to 13 GPa after thermal treatment at 1100°C. In parallel, the strain-to-rupture increased and tensile strength decreased after thermal treatment. Moreover, the fracture energy increase by 2.5 times as thermal damages occurred (Fig. A.I.8).

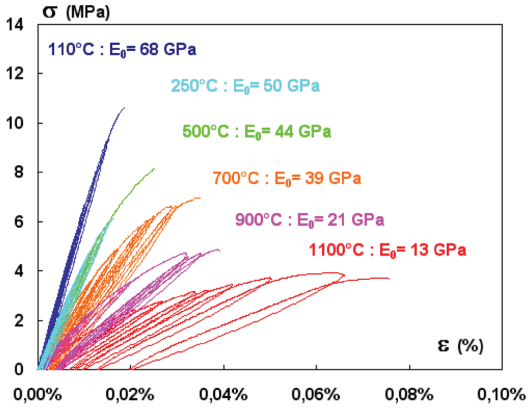

Fig. A.I.7: Tensile behavior at room temperature of Andalusite-based refractories after thermal treatments at different temperature [GK07]

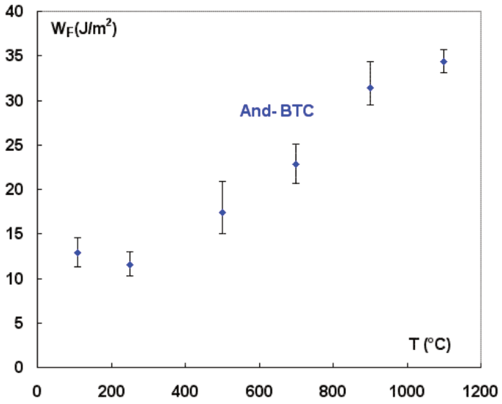

Fig. A.I.8: Evolution of fracture energy versus temperature of thermal treatment [GK07]

By using ultrasonic technique which is able to measure elastic properties, it was observed that there was a significant decrease of Young's modulus when this material had been subjected to different thermal cycles (Fig. A.I.9(a)). As explained previously, this phenomenon was caused by thermal damages due to the thermal expansion mismatch between cement matrix and andalusite aggregates (Fig. A.I.9(b)).

In this case, the andalusite monocrystal has very different thermal expansion coefficients in the 3 different directions: $\alpha_1 = 11.2{\cdot}10^{-6}$ K^{-1}, $\alpha_2 = 3.1{\cdot}10^{-6}$ K^{-1}, $\alpha_3 = 9.6{\cdot}10^{-6}$ K^{-1}. Thus, there was a strong difference of thermal expansion between andalusite inclusion and cement matrix ($\alpha_m = 7.6{\cdot}10^{-6}$ K^{-1}): $\alpha_1 > \alpha_m > \alpha_2$. Consequently, in this special case, complex thermal stresses are generated and therefore, both radial cracks and interfacial debonding could occurs during cooling stage of thermal cycles (Fig. A.I.10).

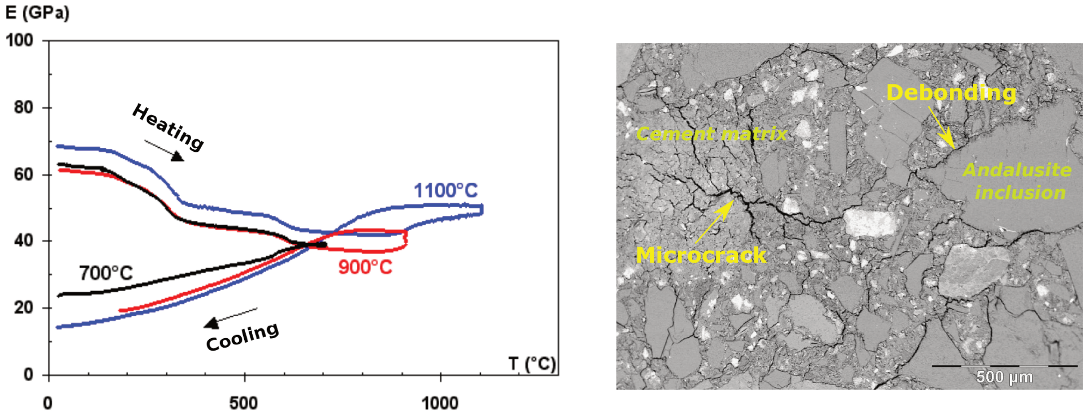

(a) Atypical behavior: Decrease of Young's modulus during cooling stage

(b) Thermal damages after cooling stage

Fig. A.I.9: Atypical behavior of andalusite-based refractory and proven reason, take from [GK07]

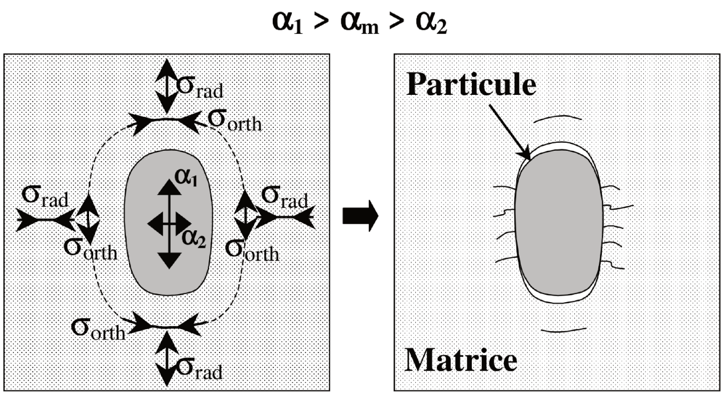

Fig. A.I.10: Thermal stresses around andalusite inclusion and associated damages during cooling, taken from [GK07]

A.I.3 Model material to investigate microstructure -properties relationships of refractories

A.I.3.1 Why model material?

As explained in the previous section, a high number of researches has pointed out that microstructures and thermal shock resistance of industrial refractories have strong relationships. However, understanding this phenomenon is not an easy task due to complex microstructures of industrial refractories. Therefore, a suitable approach is to use *model materials* that contain only 2 constituents. More specifically, only thermomechanical interactions between constituents of model materials are permitted whereas other phenomena are prohibited, e.g. physico-chemistry interaction. Despite their simplified microstructures, model materials must have behaviors close to that of the industrial refractories. Such a type of material has been developed and studied in severals researches [TD03, Jol06].

A.I.3.2 Model materials selection

In order to investigate the role of thermal expansion mismatch without influence of other phenomena, Tessier-Doyen developed several two-phases materials with simplified microstructure, namely glass-alumina composites [TD03]. Firstly, the alumina was chosen as inclusion because it corresponds to physico-chemical characteristic of aggregates generally used in industrial refractories. Secondly, it is easy to adjust the thermal expansion coefficient of glass by changing its chemical composition. Therefore, glass were chosen as matrix in order to introduce the thermal expansion mismatch. In addition, the fabrication of glass was suitable at laboratory scale. Regarding the fabrication of model materials, the alumina inclusions has spherical shape with a monomodal distribution of radii. A controlled volume ratio of inclusions was incorporated in the glass and milled to ensure the random dispersion of alumina in glass matrices. In the present study, three different volume fractions of alumina were considered in order to study the influence of alumina content on behaviors of model materials: 15%, 30%, 45%.

In the present research, two configurations of thermal damages were considered: radial microcracks and interfacial debonding. Although the studied of Tessier-Doyen was carried out in 2002, the reported results are closely related to the phenomena that are interested in the present PhD thesis. Therefore, Tessier-Doyen's results on glass-alumina composites [TD03] were used as reference to evaluate thermo mechanical modeling. After analyzing experimental results, two model material were chosen:

1. Cofer glass-alumina composite corresponds to the case $\alpha_m > \alpha_p$ in which microcracks occurs in the glass matrix;
2. BA glass-alumina composite corresponds to the case $\alpha_m < \alpha_p$ in which interfacial debonding occurs around alumina inclusion [TD03].

Thermomechanical properties of the 2 considered model materials are synthesized in Tab. A.I.1.

Tab. A.I.1: Thermo-mechanical properties of reference composite materials [TD03]

Properties	Cofer glass matrix	BA glass matrix	Inclusion
Young's modulus E (GPa)	72	68	340
Poisson's ratio ν (-)	0.23	0.20	0.24
Tensile strength σ (MPa)	60	86	300*
Coef. of thermal expansion α ($°K^{-1}$)	11.6e-6	4.6e-6	7.6e-6
Glass transition temperature (°C)	455-475	575-595	-

* Value from literature

Due to the thermal expansion mismatch between constituents of these model materials, thermal damages were generated (Fig. A.I.11), as described previously for industrial refractory materials.

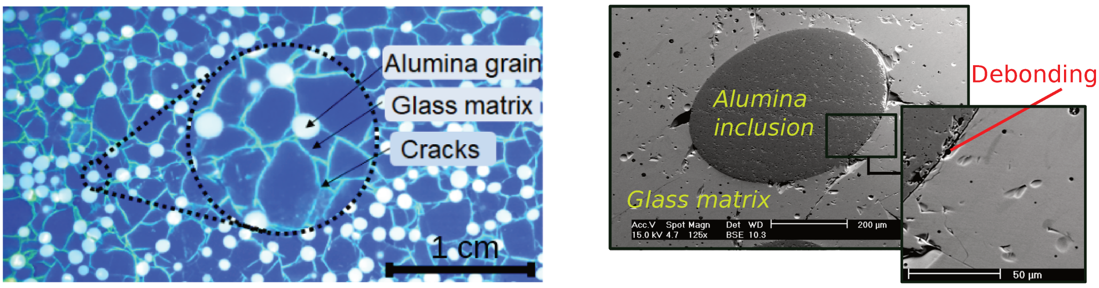

(a) Microcracks within Cofer glass-alumina, highlighted by fluorescent UV dye [TD03]

(b) Interfacial debonding within BA glass-alumina composite by SEM [Ber16]

Fig. A.I.11: Visualization of thermal damages in the considered model materials

A.I.3.3 Hashin & Strickman model: analytical prediction for undamaged material

In literature, numerous analytical models have been proposed in order to estimate the thermoelastic properties of a multiphase composite from those of its constituents. Among these approaches, the Hashin & Shtrikman (HS) model has been extensively used to predict behaviors of undamaged heterogeneous materials [HS63]. In the composite spheres assemblage constructed by Hashin, each composite sphere consists of a spherical inclusion that is surrounded by a concentric matrix shell [Has62]. The volume fraction of inclusion of each sphere is computed from radii of inclusion (r_i) and sphere (r_s) as follows:

$$f_i = \left(\frac{r_i}{r_s}\right)^3$$

In this model, the volume fraction of inclusion is the same for all composite spheres. These composite spheres of different sizes are distributed randomly in space in order to fill an arbitrary volume. Tab. A.I.2 synthesizes analytical predictions of the apparent Young's modulus and the apparent CTE of two-phases material from volume fraction of inclusion and thermomechanical properties of its constituents.

Tab. A.I.2: Analytical expressions of Hashin&Strikman to predict thermomechanical properties of two-phases materials

Lower bound HS-	Upper bound HS+
$K^{HS-} = K_m + \dfrac{f_i}{\dfrac{1}{K_i - K_m} + \dfrac{3(1-f_i)}{3K_m + 4G_m}}$	$K^{HS+} = K_i + \dfrac{1-f_i}{\dfrac{1}{K_m - K_i} + \dfrac{3f_i}{3K_i + 4G_i}}$
$G^{HS-} = G_m + \dfrac{f_i}{\dfrac{1}{G_i - G_m} + \dfrac{6(K_m + 2G_m)(1-f_i)}{5G_m(3K_m + 4G_m)}}$	$G^{HS+} = G_i + \dfrac{1-f_i}{\dfrac{1}{G_m - G_i} + \dfrac{6(K_i + 2G_i)f_i}{5G_i(3K_i + 4G_i)}}$
$\alpha^{HS-} = \alpha_i + (\alpha_m - \alpha_i)\dfrac{\dfrac{1}{K^{HS-}} - \dfrac{1}{K_i}}{\dfrac{1}{K_m} - \dfrac{1}{K_i}}$	$\alpha^{HS+} = \alpha_i + (\alpha_m - \alpha_i)\dfrac{\dfrac{1}{K^{HS+}} - \dfrac{1}{K_i}}{\dfrac{1}{K_m} - \dfrac{1}{K_i}}$
$E^{HS-} = \dfrac{9K^{HS-} \cdot G^{HS-}}{3K^{HS-} + G^{HS-}}$	$E^{HS+} = \dfrac{9K^{HS+} \cdot G^{HS+}}{3K^{HS+} + G^{HS+}}$

where: K_m, K_i are bulk modulus of matrix and inclusion; G_m, G_i are shear modulus of matrix and inclusion; f_i is volume fraction of inclusion; α_m, α_i are coefficient of thermal expansion of matrix and inclusion.

In literature, various researches have reported that the HS model could give a good estimation of thermomechanical properties of undamaged heterogeneous materials [TD03, CLTC05, Jol06]. As an example, in [TD03], the author used HS model to predict thermomechanical properties of FCu-TAB_AL composite from volume fraction of alumina and elastic properties of its contents (Fig. A.I.12). In the cited research, the Young's modulus was measured by ultrasonic technique at ambient temperature whereas the CTE was measured by thermodilatometry technique. In Fig. A.I.12, the experimental values are quite close to the lower

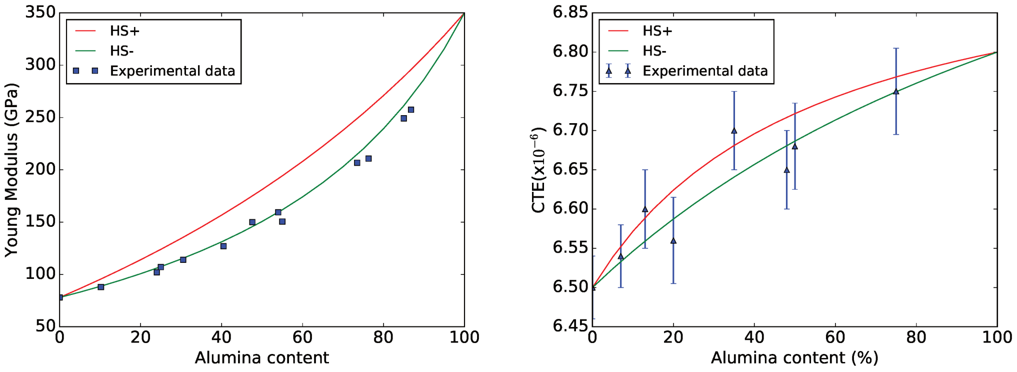

(a) Results of Young's modulus

(b) Results of CTE

Fig. A.I.12: Comparison of Young's modulus and CTE at room temperature between experimental measurements and HS model [TD03]

bound of HS model (HS- bound). Please notice that in this case, there is no damage within the considered material. Hence, these results demonstrated the accuracy of HS model to predict elastic properties of undamaged materials.

A.I.3.4 Limitations of Hashin & Strickman model

In paragraph A.I.3.3, the accuracy of HS model to predict thermomechanical properties of undamaged material was discussed. Herein, the application of HS model to damaged material will be also studied. In Tessier-Doyen's study [TD03], thermal damages occurred during cooling at about 200°C for Cofer glass-alumina composite and at about 280°C for BA glass-alumina composite. The reported results showed that thermal damages influenced significantly the behaviors of these materials.

Fig. A.I.13 shows the comparison of evolution of Young's modulus between experimental measurements and HS model. Similar tendencies could be observed for the two model materials. At the beginning of cooling, when material is still undamaged, the HS- bound follows well the experimental curves. Again, these results confirm the accuracy of HS model to describe undamaged material. However, when thermal damages occur, the experimental curves diverge from HS- bound. Indeed, the decrease of Young's modulus of Cofer glass-alumina is about 40 GPa (Fig. A.I.13(a)). Whereas the decrease of Young's modulus of BA glass-alumina is only 6 GPa (Fig. A.I.13(b)). This could be explained by different thermal damages within these materials (Fig. A.I.3 and A.I.11). In

Cofer glass-alumina composite, the radial cracks are initiated around the inclusions and interact with each other. By contrast, in BA glass-alumina, debonding occurs separately around inclusions, without interaction. Consequently, thermal damages are more developed in Cofer glass-alumina composite than in BA glass-alumina composite. These results reveal that the difference between experimental measurement and HS model allow to quantify the effect of thermal damages on properties of materials.

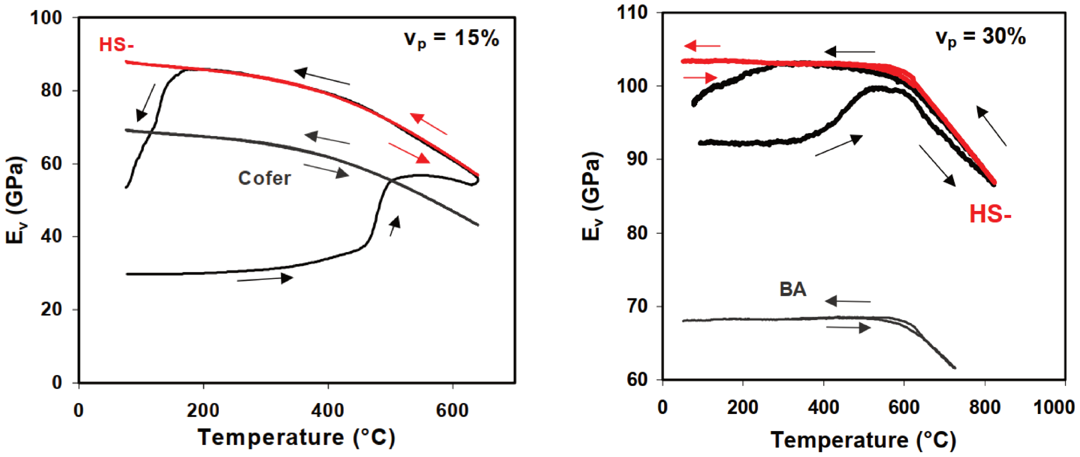

(a) Case of Cofer glass-alumina composite (b) Case of BA glass-alumina composite

Fig. A.I.13: Comparison of Young's modulus during cooling between experimental measurements and HS model [TD03]

Typically, the evolution of Young's modulus as function of temperature could be divided into 4 main zones [TD03, Jol06] (Fig. A.I.14):

- The first zone, from 20°C to the transition temperature T_g: low and quite constant values of Young's modulus;
- The second zone, from T_g to sintering temperature: increases of Young's modulus as temperature increases. At the beginning, damages that existed already within material are resorbed. After a sudden increase, viscosity of materials decreases, thus, their mechanical properties decrease. Hence, a dwell and/or a decrease of Young's modulus could appear which indicate the competition between flaws resorption process and the material softening;
- The third zone: increase of Young's modulus as temperature decrease (cooling). In this zone, materials in viscous state harden again as the temperature decreases;

- The fourth zone: brutal drop of Young's modulus. In this zone, thermal stresses within materials reach critical value and therefore, damages initiated and propagated.

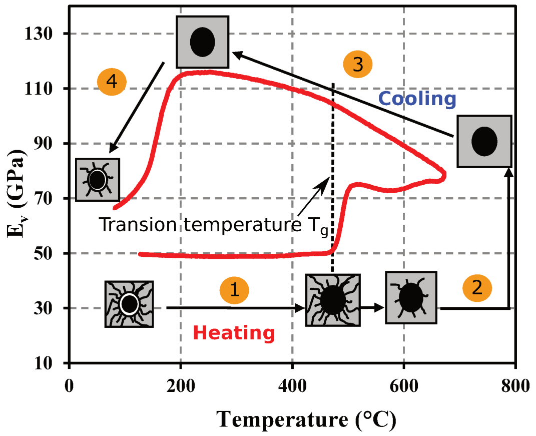

Fig. A.I.14: Typical evolution of Young's modulus versus temperature of refractory materials

As a consequence, the alumina content had a strong impact on Young's modulus and coefficient of thermal expansion of model materials. As shown in Fig. A.I.15, experimental value of E and α are lower than the HS- bound. These observations highlight significant loss of E and α values due to thermal damages.

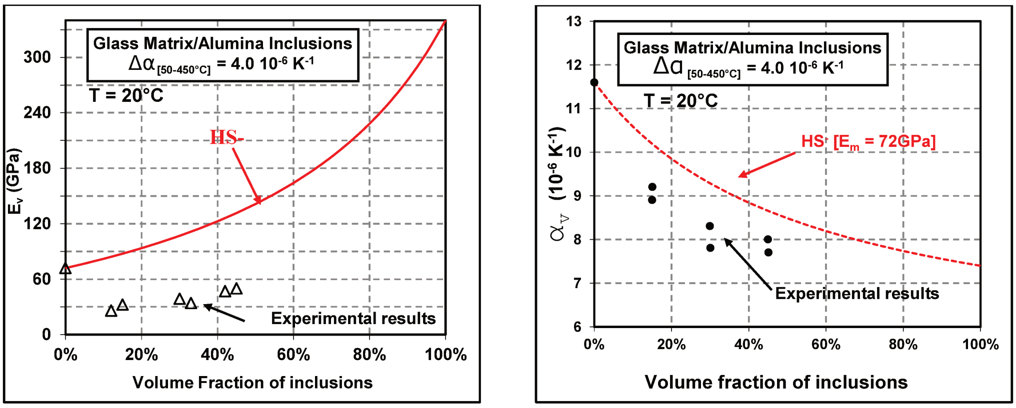

(a) Comparison of Young's moduls, case of Cofer glass-alumina composite

(b) Comparison of thermal expansion coefficient

Fig. A.I.15: Comparison between experimental thermomechanical properties at room temperature and Hashin & Strikman model, case of Cofer glass-alumina composite [TD03]

As discussed above, the HS model is able to predict thermomechanical properties of undamaged materials. In addition, the difference between HS model and experimental measurements allows to quantify the effect of thermal damages on material properties.

A.I.4 Conclusion

This chapter has allowed to present the microstructures-properties relationships of several refractory materials.

Several researches have reported that in some specific cases, thermal damages could have positive influence on thermal shock resistance of refractories, e.g. decrease of Young modulus, decrease of CTE, decrease of strength, increase of strain-to-rupture and increase of fracture energy. The experimental observations showed a great interest to investigate and to take advantages of the microstructures-properties relationships in order to improve thermal shock resistance of refractories. However, this is not an easy task due to the complex microstructures of industrial materials. Hence, a more suitable approach is to investigate model material that contains only 2 constituents. Despite its simplified microstructures, model materials have behaviors close to those of industrial material.

As discussed previously, HS model could give quite good estimation of thermomechanical properties of undamaged material. However, up to now, it is still complicated to take into account the effects of damages by using analytical prediction. Nowadays, numerical methods could predict thermomechanical properties of heterogeneous materials by considering their microstructure, including microcrack network, in addition to their intrinsic properties. The longterm purpose is to predict quantitatively the influence of thermal damages on behavior of complex industrial materials by using numerical method. This could give insights for microstructure design of refractories. Therefore, the desired numerical approach must be able to model high amount of discontinuity within heterogeneous media. The present research is a first step in order to achieve the long term purpose. It focused on the modeling of the behaviors of model materials developed by Tessier-Doyen, i.e. Cofer glass-alumina and BA glass-alumina [TD03]. The next chapter is dedicated to the selection of numerical approach.

Chapter A.II

Numerical method for damages modeling

A.II.1 Overview of numerical methods

Nowadays, thanks to the spectacular development of computer technology, numerical simulation is used extensively in order to solve complex practical problems in engineering and science. In material science, numerical simulations is an efficient tool to validate analytical models, to assists in the interpretation of physical phenomena and to offer valuable insights for experimental research. Generally, in thermomechanical area, numerical methods can be classified into continuum method and discontinuum method, each one has its advantages and drawbacks. Despite their different natures, these numerical methods have similar procedure in order to solve the targeted problem [Jeb13]:

- Governing equations: mathematical models are derived with some possible assumptions in order to describe the observed physical phenomena. These mathematical models are generally expressed in terms of governing equations with boundary conditions. The governing equations are mainly expressed by using differential equations and/or partial differential equations;
- Discretization: the problem is discretized into finite discrete components in order to solve numerically the governing equations;
- Solving of governing equations: Numerical algorithms that allow to solve governing equations of the discretized domain from boundary conditions needs to be developed;

- Programming: the developed algorithm is implemented into a computer code in some programming languages.

A.II.2 Continuous methods

A.II.2.1 Overview

The Continuum Methods (CMs) has been developed for a long time. Hence, this class of numerical method have been widely applied to various area of Computational Mechanics, e.g. solid mechanic, fluid dynamic. The main assumption of CMs is that matter is a continuum that completely fills the space. In CMs, the considered continuum domain is discretized into discrete components (element) made up of reference points (node). Then, the governing equations are changed into a system of algebraic equations. The resolution of this system gives the solutions at the reference points. For other points in the occupied space, the field variables can be approximated by interpolation or averaging of the solutions at the reference points.

The CMs are well adapted for simulating physical phenomena in which the continuity assumption is valid and remains valid during the simulation. However, this class of method faces some difficulties related to discontinuities that occurs. Indeed, additional treatments must be carried out to described the new surfaces. In literature, there are several techniques to deal with the discontinuities problem for different CMs.

A.II.2.2 Finite element method

Finite Element Method (FEM) describes the behavior of material by discretizing object (sample) into subdomains (elements) which are interconnected through common discrete nodes. Hence, the assembly of elements is called a mesh. Based on an adequate mesh, governing equations can be approximated by a set of algebraic equations for each finite element. The system of algebraic equations for the whole domain can be formed by assembling the elementary algebraic equations for all the elements. In this method, reliable constitutive laws between the stress and strain field have been developed for a long time. The primary unknown field variables are nodal values. The FEM formulation reduces the problem to the solution of a system of algebraic equations in terms of the nodal variables. FEM is capable to model complex geometries, boundary conditions and heterogeneous material. In spite of its successes in various area of computational mechanics, the major problem of FEM is that remeshing and mesh refinement are required in order to take into account discontinuities. More specifically, remeshing technique involves superposition of a new mesh on the old one in order to describe new surfaces of cracks (Fig. A.II.1). This process is very time consuming, making FEM inadequate for discontinuous problems.

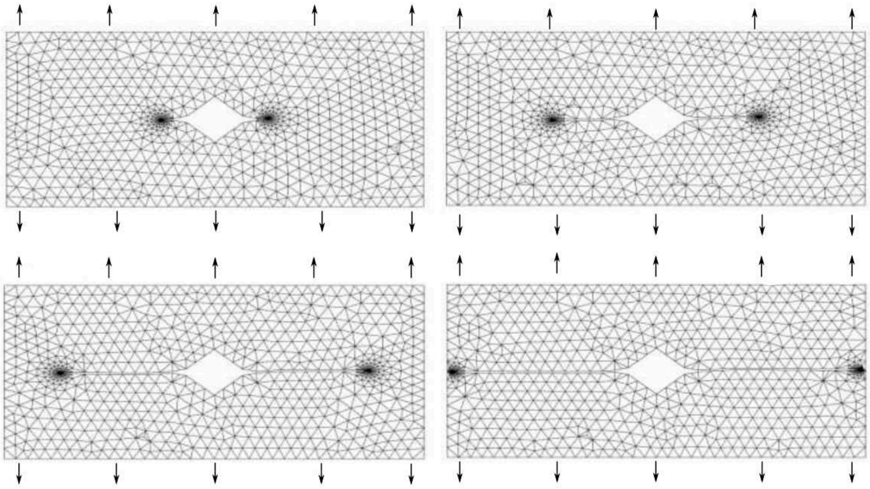

Fig. A.II.1: Illustration of crack propagation in tensile test by FEM: mesh refinement and remeshing are required around crack tips [SMAA09]

Later on, the eXtended Finite Element Method (XFEM) has been developed in order to alleviate the issue of FEM to describe arbitrary cracks in regular meshes. Initially, XFEM was proposed by Belytschko *et al.* [BB99, MDB99]. In this method, finite element discretization is enriched with additional nodal degrees of freedom, which carry local discontinuous functions, able to describe cracks within elements. More specifically, equations of displacement field of the elements that contain crack are enriched. Hence, cracks can be described accurately in a single mesh, removing the need of continuous remeshing to describe crack propagation (Fig. A.II.2)

This method has been applied to model phenomena involving discontinuities such as crack growth in rock, concrete or alloy [GJ16, LZG^{+}18, RLK19]. However, the use of XFEM to model problems with multiple cracks remains limited due to its cumbersomeness to deal with high amount of discontinuity.

As an example, Vijay and Rafael used XFEM in order to model crack propagation at microscopic scale of an aluminum alloy under tensile loading [GJ16] (Fig. A.II.3). However, in this research, crack location still needed to be prescribed and crack branching was not modeled.

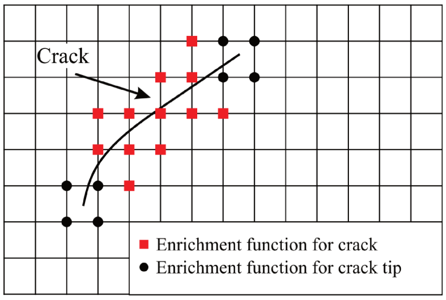

Fig. A.II.2: Illustration of XFEM discretization for describing cracks in regular mesh [Ngu15]

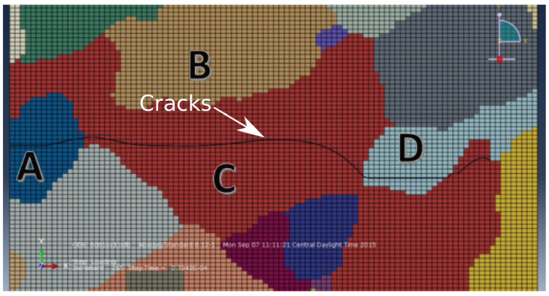

Fig. A.II.3: Crack propagations in microstructure of an aluminum alloy (grains were assigned different colors in order to display the microstructure) [GJ16]

In order to deal with the modeling of phenomena that involves high amount of discontinuity, the Phase Field Method (PFM) has been developed. The PFM, initially proposed in 1998 by Marigo and Francfort, is based on an energy minimization framework, related to Griffith's theory for brittle fracture [FM98, BFM08, PM10]. More specifically, a regularized variational approach is discretized by a finite element procedure. Thanks to this technique, both evolution of the mechanical problem and evolution of an additional field d describing the damage (called phase field) could be modeled. Hence, this technique strongly alleviates meshing problems for describing brittle cracking by using a fixed mesh and a regularized description of the discontinuities. In addition, the PFM does not require any prescription of the shape geometry and allows crack nucleation and branching. Hence, this method is able to model complex phenomena such as: initiation, coalescence and propagation of arbitrary crack morphologies. The PFM has been used for describing 2D and 3D quasi-static fracture [KM10, MWH10], dynamic crack propagation [BLR11, BVS^{+}12, BHLV14], brittle fracture under multiphysics environment [MSU15, MHSA15, NBR^{+}17]. Nevertheless, the main limitation of this method is that 3D simulations could be quite time consuming.

As an example, in the research of Nguyen *et al.* [NBR^{+}17], the authors applied the PFM to model stress corrosion crack propagation in a nickel-base alloy . In this research, complex crack network was modeled and compared with experimental observation obtained by Digital Image Correlation. The comparison show a good agreement between numerical results and experimental observations in terms of crack geometry and crack length. However, since stress corrosion cracking of homogeneous material was investigated in this research, prescriptions of locations and moments of crack initiation were still needed.

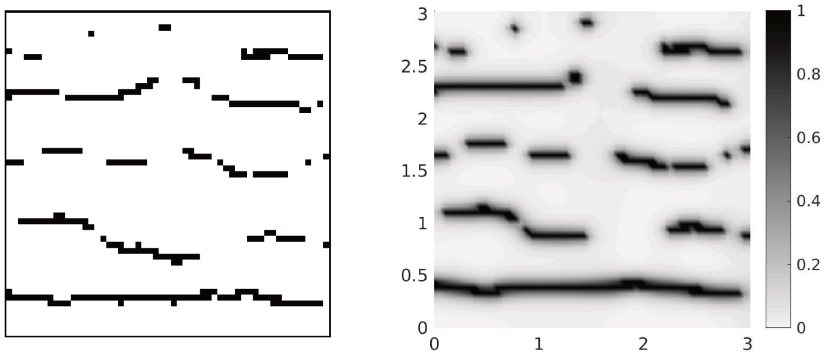

Fig. A.II.4: Comparison between experimental crack obtained from DIC procedures and from PFM of the Inconel 600 alloy sample in sub-volume size 2×3×3 mm^3 (left: experiment; right: numerical simulation) [NBR+17]

A.II.3 Discrete methods

A.II.3.1 Overview

The discrete methods (DMs) consist in simulation of an assembly of points/rigid bodies that interact with each other through interaction laws. Initially, the DMs has been developed for problems of granular materials in rock mechanics [Cun71]. Later on, DMs has been applied to continuous media in order to model complex damage phenomena that involve high amount of discontinuity. This class of numerical method has been applied successfully in several type of materials, e.g. concrete [HDD04, NT18], rocks [BFJ+09, LG14, NI15] and ceramics [TYS09, ZH15, JLZ+18]. In these researches, the continuous media is modeled by an assembly of discrete elements which interact via contact laws to ensure the cohesion of the medium. In literature, various types of contacts law to model continuous media have been proposed: parallel bond model [CMS07], cohesive bond model [AJI+13, ACI15, JATI15], flat-joint model [WX16], etc.

The application of DMs in continuous media simulations faces two significant challenges:

- Choice of the contact laws that involves limited number of input parameters in order to describe behavior of continuous media. In addition, an adequate calibration method of input parameters needs to be established in order to obtained quantitative results;
- Construction of assembly of discrete elements such that the mechanical properties of simulated domain are independent of the discrete elements number. Moreover, the so-called discrete domain must take into account the structural properties of the problem domain, e.g. homogeneity, isotropy and anisotropy [CLPG18].

Nowadays, DMs have been increasingly used in order to study physical phenomena at microscopic scale, where the continuity assumption is no longer valid, or phenomena that involve discontinuities which cannot be easily treated by CMs.

A.II.3.2 Lattice models

Lattice models was firstly proposed by Hrennikoff in 1941 [Hre41]. This models consists in discretizing a solid into an assembly of nodes interconnected by beam elements (Fig. A.II.5). In general, nodes have neither masses nor volumes.

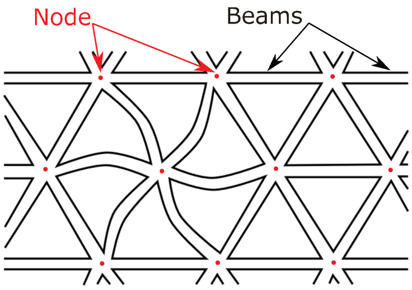

Fig. A.II.5: 2D regular triangular lattice of beams [JATI15]

In lattice models, mechanical problems are solved by constructing a global stiffness matrix from local properties of beam. Schlangen et *al.* demonstrated that the torques at local scale influence strongly the crack behavior [SG97]. Indeed, the displacement and rotation of node assembly could be obtained as follow:

$$\mathbf{X} = \mathbf{K}^{-1} \cdot \mathbf{F} \qquad \text{(A.II.1)}$$

where: **X** is the unknown vector of problem, it contains displacement and rotation vectors of node assembly; **K** is the global stiffness matrix; **F** is the loading vector, which contains force and torque vectors of beams.

Despite its "simple" formulas at local scale, lattice models are able to model elastic continuum and fracture phenomena of materials with complex microscopic structures [SG96, SG97, NKIM18]. As an example, Schlangen et *al.* used lattice models in order to study fracture phenomena of concrete [SG96, SG97]. In these researches, crack pattern observed in shear experiment on concrete plate were modeled accurately by using beam elements (Fig. A.II.6)

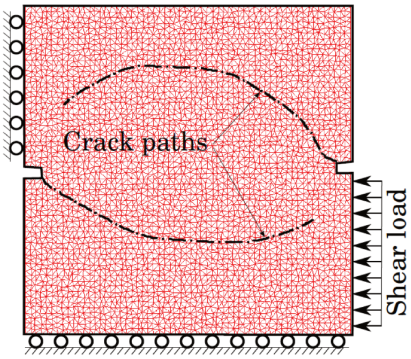

Fig. A.II.6: Crack pattern of shear experiment on concrete plate obtained by lattice model [SG96]

The main drawback of lattice models is that the nodes do not have volumes, which causes difficulty to model crack closure phenomena. To deal with this issue, Ibrahimbegovic *et al.* [ID03] proposed to assign to each node an equivalent volume, based on the spacial Voronoï decomposition. However, this solution seems to be quite time-consuming for 3D problems.

A.II.3.3 Particle models

Particle models consist in simulation of an assembly of rigid bodies (elements) that interact with each other through interaction laws. This class of methods is very similar to the discrete approach proposed by Cudall and Strack [Cun71, CS79]. In general, elements often have disk shape (2D) or spherical shape (3D). Thus, computational time decreases since only radius is needed to determine geometry of elements (geometrically, no additional memory is needed when spherical elements rotate). In addition, in particle models, mass and volume are assigned to each element in order to facilitate the modeling of crack closure. In literature, to model phenomena that involved significant shear effects, more complex shapes (ellipsoids, polygons or polyhedra) has been proposed in order to limit the rotation of elements. Nevertheless, these complex shapes could increase significantly the computational time.

Particle models could be divide in two main variants: smooth contact particle models and non-smooth contact particle models. The former is suitable to model continuous media whereas the latter is generally used to study quasi-static problem or granular media. Thus, in this paragraph, only the smooth contact is presented in detail. The resolution of smooth contact particle models involves two main steps. Firstly, interaction forces are computed when overlapping between elements occurs. The associated force-interpenetration formula is called "smooth contact" model. It involves mechanical interaction laws that describe simple relation between forces and displacements. Thanks to these interaction laws, smooth contact model could take into account easily elasticity of material. Generally, linear interaction laws (spring models) are often used when overlapping between elements occurs (Fig. A.II.7).

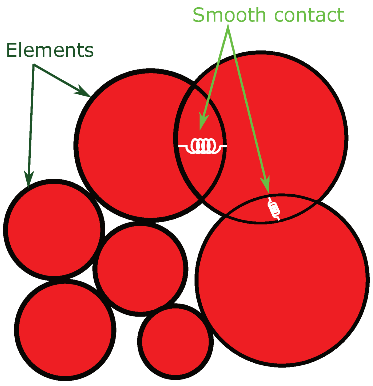

Fig. A.II.7: 2D example of smooth contact model

Secondly, Newton's second law is applied to compute acceleration of each element. Based on acceleration and previous state, new velocities and positions of element are computed by using "dynamic explicit" schemes. This process is repeated iteratively during simulation.

As an example, Fleissner *et al.* applied a particle method to simulate orthogonal cutting processes [FGE07]. In this research, a 3D model of a breakable solid was generated by bonding rigid spherical particles. The workpiece is machined using a tool represented by triangles and moved according to a function of time. A 2D illustration of this simulation is shown in Fig. A.II.8.

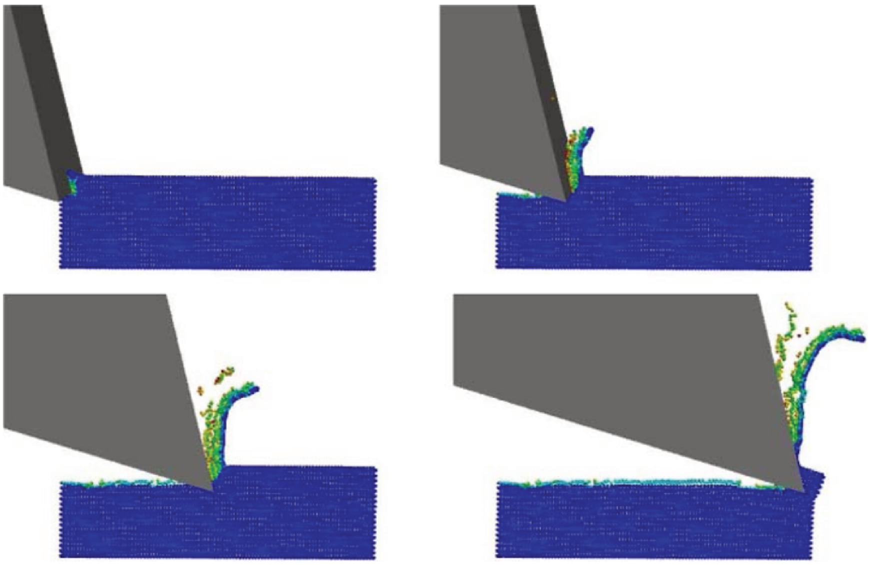

Fig. A.II.8: Simulation of cutting process of elastic-plastic solid by particle method [FGE07]

A.II.3.4 Hybrid lattice-particle model

As presented before, the lattice and particle models have their own advantages and drawbacks. However, their advantages could complete each other in order to alleviate their drawbacks. This give insight to combine the lattice and particle models in one model, namely *hybrid lattice-particle model* or bonded-particle model, as it was first proposed by Potyondy [PC04] (Fig. A.II.9).

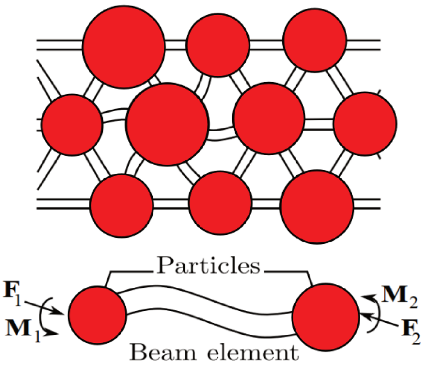

Fig. A.II.9: 2D example of hybrid lattice-particle model [JATI15]

Indeed, the smooth contact particle models is suitable to model continuous media since elasticity is naturally taken into account in their interaction laws. However, this class of model faces difficulties when significant shear effects are involved [JATI15]. This drawback can be overcome by using cohesive beams in *hybrid model* in order to connect elements, as in lattice models. Moreover, since volume is assigned to each element, it is possible to restore beam contacts that were broken before. This make the so-called *hybrid model* able to deal with the crack closure phenomena of continuous media.

As an example, a versatile modeling platform with hybrid lattice-particle model has been developed by André *et al.* since 2009 [AIICN12, ACI15, JATI15]. This discrete model platform allows to describe an elastic solid by a set of discrete elements linked by cohesive beams [JATI15]. Up to now, the developed modeling platform has been able to describe quantitatively mechanical, thermal and electrical behavior of continuous media [AJI+13, ACI15, HAD+17, TIC13]. For example, in mechanical area, André *et al.* [AJI+13] used hybrid model in order to simulate brittle fracture of glass in indentation test (Fig. A.II.10). Fig. A.II.10 shows that the developed hybrid model could reproduce crack shape in 3D which is similar to experimental. observation.

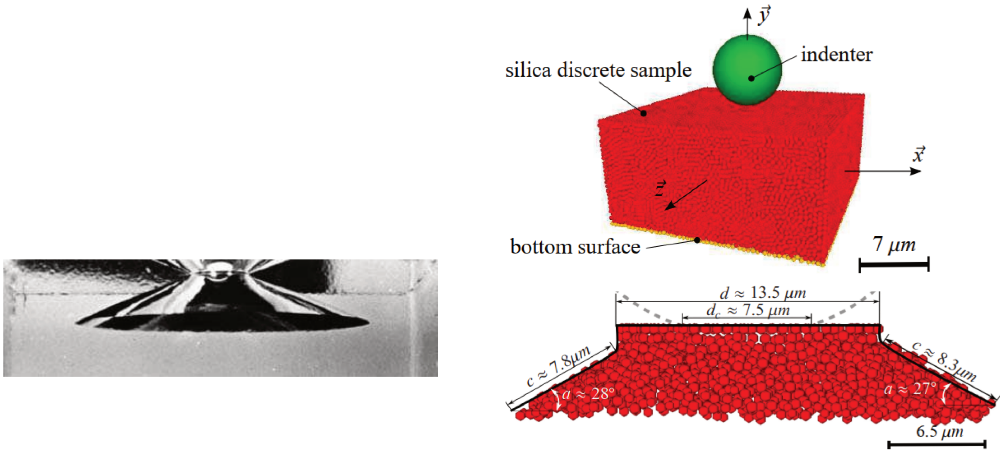

(a) The hertzian cone crack after indentation test [Roe56]

(b) Discrete model simulation and associated crack shape [AJI+13]

Fig. A.II.10: Simulation of brittle fracture in indentation test by hybrid lattice-particle model

A.II.4 What class of numerical methods to achieve the purpose of the present research?

As presented previously, there are many numerical methods applied in Computational Mechanics. These methods can mainly be classified into discrete methods and continuous methods. The former is based on Newtonian mechanics whereas the latter is based on continuum mechanics which consider matter as a continuum.

As discussed in chapter I, the present research investigates the effects of thermal damages on thermomechanical behavior of refractories in order to strengthen experimental results and to give insight for microstructure design. Therefore, this investigation involves high amount of discontinuities. As reported in Sect. A.II.2, reliable constitutive laws between stress and strain field have been developed for continuous method for a long time. However, in order to manage high amount of discontinuities or simultaneous cracking, additional treatments are required for continuous methods. Despite significant successes of several technique, e.g. XFEM, PFM, their applications for complex crack phenomena still, up to now, remain problematic. Especially, the minimization of computational time for 3D simulations of multiple cracks is still in progress.

Thanks to the ability to describe discontinuities, the discrete methods is a good candidate for the present research. Indeed, in this class of method, matter is consider as assembly of point/rigid bodies that interact with each other through interaction laws. The initiation of crack could be simply handled by breaking interaction between elements. The discrete methods were divided into two main subclasses: lattice models and particle models. Since these two subclasses are quite complementary, a "hybrid" method that combines their advantages was retained. Specifically, the variant of the Discrete Element Method (DEM) developed by André *et al.* [ACI15, JATI15] and the associated DEM modeling platform were chosen in order to achieve the purpose of the present research. The main specificities of this methods as well as the development of DEM modeling platform, namely GranOO, will be detailed in part B.

Part B

Development of discrete element modeling platform

Introduction

The main purpose of the present research is to investigate the influences of thermal damages on the behaviors of heterogeneous materials and the associated phenomena, e.g. the nonlinear behavior of refractories. According to the bibliographic study in part A, the Discrete Element Method (DEM) has shown several advantages in the modeling of fracture phenomena, e.g. the simultaneous damage propagations which is typical for refractories. For this reason, the *GranOO* DEM platform was used in the present works to study the behaviors of heterogeneous material. However, there are two main challenges for the application of DEM to model continuous media:

- establishment of relationships between input parameters and output results in order to facilitate its usage for non specialist;
- further development of stress computations in order to describe accurately fracture phenomena due to complex loading.

Part B is therefore dedicated to the development of GranOO platform during the present research. This part includes 2 chapters.

The first chapter is dedicated to a general review of *GranOO* platform. In this chapter, the architecture of DEM platform, the key elements of DEM simulation and the contact model are presented. Furthermore, the new developments of virial stress computation is also detailed.

In the second chapter, a novel calibration method of input parameters for the used DEM approach is proposed and validated through various simulation configurations. Moreover, the accuracy of virial stress computation was examined through its application to the modeling of the residual stress due to thermal expansion mismatch and the associated damages within an elementary composite materials. Indeed, the stress field obtained with DEM will be confronted with FEM and theoretical predictions. Moreover, the DEM results of damage propagations will also be compared with experimental observations [TD03, Jol06].

Chapter B.I

GranOO - A versatile discrete element modeling platform

B.I.1 DEM explicit dynamic resolution algorithm

B.I.1.1 Positions and orientations computations in DEM

In general, all DEM modelings involve the computation of acceleration of discrete elements at each time step. Indeed, the calculation of the new position of the discrete elements requires the integration of acceleration to provide position and velocity at the considered time step. In computer simulations of physical processes, explicit and implicit integration schemes can be used to obtain numerical approximate solutions of partial differential equations that describes a time-dependent problem. The explicit scheme calculates the state of a system at a later time from the current state of the system, whereas implicit scheme finds a solution by solving an equation involving both the current state of the system and the later one. Explicit scheme gives a faster solution in dynamic phenomena whereas the implicit method is privileged when the physical phenomena are much slower. The choice of implicit or explicit scheme depends on the goal of the computation. In the frameworks of the *Granular Object Oriented Workbench (GranOO)*, the numerical resolution is based on an explicit integration scheme, which is well adapted to massive DEM simulation and high velocity phenomena such as fracturing or impact [JATI15]. Many explicit schemes can be found in literature, e.g. the Verlet velocity, Runge-Kutta or gear's method, etc. Several researches have pointed out that all of these schemes give approximately the same efficiency [RMJ04]. Consequently, *André et al.*. have implemented in *GranOO*, the explicit dynamic resolution algorithm based on the Verlet velocity scheme, for its simplicity. This implementation is used for all DEM simulations presented in this study. More specifically, the discrete element positions and velocities are estimated by:

$$\mathbf{p}(t+\Delta t) = \mathbf{p}(t) + \Delta t\,\dot{\mathbf{p}}(t) + \frac{\Delta t^2}{2}\,\ddot{\mathbf{p}}(t) \tag{B.I.1}$$

$$\dot{\mathbf{p}}(t+\Delta t) = \dot{\mathbf{p}}(t) + \frac{\Delta t}{2}\,(\ddot{\mathbf{p}}(t) + \ddot{\mathbf{p}}(t+\Delta t)) \tag{B.I.2}$$

where:

- t is the current time and Δt is the integration time step.
- $\mathbf{p}(t)$, $\dot{\mathbf{p}}(t)$ and $\ddot{\mathbf{p}}(t)$ are the linear position, velocity and acceleration of the discrete elements.

In *GranOO*, the discrete element orientations are described by quaternions, which is defined as the quotient of two vectors [Har81]. More specifically, the quaternion is an operator which modifies the direction and the norm of a vector. A quaternion q can be considered as a linear combination of four quaternions units, i.e. $1, i, j$, and k (Eq. B.I.3)

$$q = a.1 + a_1.i + a_2.j + a_3.k \tag{B.I.3}$$

where a, a_1, a_2, a_3 are real numbers, and i, j, k are the fundamental quaternion units. The usage of quaternions gives an efficient way to compute the rotation of the local frames associated with the discrete elements [PS05]. The angular velocity of discrete elements is obtained by using Eq. [Ebe10]:

$$\dot{q}(t) = \frac{1}{2}\,\boldsymbol{\omega}(t)\,q(t) \tag{B.I.4}$$

where $q(t)$ is the orientations of discrete element, $\boldsymbol{\omega}(t)$ is the angular velocity of discrete element. The Verlet velocity scheme is also applied to quaternion $q(t)$, with:

$$q(t+\Delta t) = q(t) + \Delta t\,\dot{q}(t) + \frac{\Delta t^2}{2}\ddot{q}(t) \tag{B.I.5}$$

$$\dot{q}(t+\Delta t) = \dot{q}(t) + \frac{\Delta t}{2}\,(\ddot{q}(t) + \ddot{q}(t+\Delta t)) \tag{B.I.6}$$

Finally, to prevent quaternion numerical drifts, the quaternion must be normalized at each time step.

B.I.1.2 Overview of the resolution algorithm

Algorithm 1 shows the implementation of the Verlet velocity scheme in the explicit dynamic resolution of *GranOO*. This simplified algorithm hides the main difficulty of the elaboration of a numerical experiment, whose loadings, boundary conditions, micro mechanical models or involved geometries can be complex. This is one of the main advantages of *GranOO* platform: ability to provide tools and mechanisms, in a coherent environment, to perform DEM simulations in a quite easy way. This aspect will be presented briefly hereafter.

Algorithm 1: Explicit dynamic resolution [JATI15]

```
input: $\mathbf{p}(0)$ $\dot{\mathbf{p}}(0)$ $\ddot{\mathbf{p}}(0)$ $q(0)$ $\dot{q}(0)$ $\ddot{q}(0)$
$t \leftarrow 0$;
foreach iteration $n$ do
    foreach discrete element $i$ do
        $\mathbf{p}_i(t+\Delta t) \leftarrow$ Verlet velocity scheme (B.I.1);
        $\mathbf{F}_i(t+\Delta t) \leftarrow$ Sum of forces acting on $i$;
        $\ddot{\mathbf{p}}_i(t+\Delta t) \leftarrow$ Newton's second law;
        $\dot{\mathbf{p}}_i(t+\Delta t) \leftarrow$ Verlet velocity scheme (B.I.2);
        $q_i(t+\Delta t) \leftarrow$ Verlet velocity scheme (B.I.5);
        $q_i(t+\Delta t) \leftarrow$ Normalization;
        $\mathbf{M}_i(t+\Delta t) \leftarrow$ Sum of torques acting on $i$;
        $\ddot{q}_i(t+\Delta t) \leftarrow$ Angular momentum law;
        $\dot{q}_i(t+\Delta t) \leftarrow$ Verlet velocity scheme (B.I.6);
    $t \leftarrow t+\Delta t$
```

B.I.2 Architecture overview of GranOO platform

B.I.2.1 GranOO - a C++ object oriented workbench

The *Granular Object Oriented Workbench (GranOO)* has been developed since 2010 by the collaboration of 3 laboratories: Institute of Research for Ceramics (IRCER, Limoges, France), Institute of Mechanics and engineering (I2M, Bordeaux, France), Laboratory of Industrial and Human Automation control, Mechanical engineering and Computer Science (LAMIH, Valenciennes, France) [And12, JATI15]. This platform of discrete element modeling is designed based on explicit dynamic resolution algorithm to perform a wide range of numerical experiments. The conditions of computation platform, i.e. upgrade ability, robustness and performance, need to be well guaranteed. To reach this purpose, the C++ programing language, which is standardized and efficient, has been chosen to implement *GranOO*. In fact, C ++ is a compiled language, whose performances have become comparable to those of the C or the Fortran languages, which are part of the fastest programming language. In addition, the object oriented *(OO)* approach is used to design *GranOO*, whose architecture is based on an organization in libraries. This kind of architecture facilitates the upgrade process. Robustness aspect of computation is ensured by the systematic application of the concept of *programming by contract* [McK96]. Finally, an operating architecture based on the usage of *macro-command*, which was also called *plugin* in the existing documentations of *GranOO*, ensure a flexible utilization of platform. The integration and scheduling of *macro-command* are done through modifiable *input files* in eXtensible Markup Language *(XML)* format. More informations about this original and versatile computation platform are given in [And12, JATI15]

B.I.2.2 Input files and macro-command

In order to facilitate the manipulation of DEM simulations for non-specialist user, a modifiable *input file* in *XML* format is used as an interface between *GranOO* source code and user. Indeed, the input files, which can be easily configured by user, is dedicated to integration and scheduling of *macro-commands*. In addition, the *macro-commands* facilitate the usage of source code in order to develop specific configurations of DEM simulation, e.g. loading, boundary condition, etc. By using standard and user-defined *macro-commands*, the users could develop their own configuration of DEM simulation, without a high requirement of C++ programming knowledge. Typically, an input files has two fundamental parts, i.e. pre-processing and processing. The first part corresponds mainly to macro-commands that are related to the reading of discrete domain and the contact properties. The second part is dedicated to macro-commands that are related to configurations DEM simulations, e.g. boundary conditions, stress computations and saving results options, etc. An other important point is related to the saving of output discrete domains with several associated informations. This allows to develop a DEM simulation based on the results of the other ones. More specifically, the discrete domain can be saved in a *granoo discrete domain file (gdd)*, which contain complete characteristics of domain, e.g. positions, accelerations of discrete elements; mechanical properties of contact, etc. In summary, the concept of *input file* and *macro-command* makes the DEM simulations much more easier and promotes the application of DEM to the modeling of brittle elastic media.

B.I.2.3 Essential libraries and tools

The architecture of the *GranOO* discrete element modeling platform is designed based on an *OO* approach where classes are grouped into libraries. The *GranOO* platform is composed of 11 libraries written in C ++ language. The 5 fundamental libraries, and the visualization and post processing features are briefly presented hereafter.

libUtil is dedicated to manage computer issues, i.e. reading and writing *XML* files, management of macro-commands, data compression, digital sensors, etc.

libMath integrates mathematical tools, i.e. usual mathematical functions and statistical calculations.

libGeom is dedicated to Euclidean geometry calculations in a 3D space. This library models the concepts of basic entities in Euclidean geometry, e.g. coordinate system, point, vector, quaternion, etc. It proposes also various common operations for 3D calculations, e.g. change of local frame, projection, rotation, norm, etc. A DEM simulation is intensively based on the usage of the entities developed in the *libGeom*. Consequently, this library has been developed with high attention in terms of performance, robustness and accessibility.

libShape provides the concepts of geometric shapes, e.g. sphere, cone, cylinder, box, rectangle, etc.

libDEM is specifically dedicated to the implementation of DEM simulations. This library provides the concepts of discrete elements, cohesive bond, boundary condition, discrete domain, etc. These concepts are based on the three previous libraries. The *libDEM* provides also various features to manipulate efficiently DEM simulations, e.g. containers, simple expressions of boundary conditions and loadings, etc. In fact, to perform a DEM simulation, the user needs to be able to extract sets of entities (discrete elements, contacts, etc.) in order to apply specific treatments to them, e.g. loading or boundary conditions. As a result, *libDEM* provides tools to facilitate this type of action. The identification is carried out via specific containers, called *SetOf*, and the treatments are applied by *macro-command*. The *SetOf* is one of the fundamental mechanisms of *GranOO*. It allows a simple and exact identification of DEM entities of different types and guarantees also an efficient extraction of numerical data.

Visualization and post processing features provide the abilities to visualize and manipulate easily the results of DEM simulations, e.g. stress field, temperature field or damage propagation, etc. Firstly, the *granoo-viewer* feature, which is dedicated to the visualization of simulations results, has been developed in *GranOO* platform. This feature allows a visualization the contents of a *gdd* file in 3D interactive mode. Therefore, the user could check the progress of simulations and get a better description of the results. More recently, a new feature, dedicated to further post-treatments of DEM results has been implemented. Indeed, simulations results could be saved in a *pvd* file, which is compatible with *Paraview* software[1]. Thus, it makes the visualization of DEM results easier and more efficient. Moreover, the numerical data could be easily manipulated by *Paraview* and/or by *Python*, which enables the comparison of DEM against theoretical predictions and/or other numerical approaches, e.g. *FEM*, as it will be described in section B.II.4

B.I.2.4 The main steps of DEM simulations

In summary, the *GranOO* platform is based on 5 fundamental libraries, i.e. *libUtil, libMath, libGeom, libShape, libDEM*. In order to develop a DEM simulation, the user needs to communicate with these libraries via the *input file* and *macro-commands*, as presented in B.I.2.2. The main steps to develop and exploit a DEM simulation are resumed in Fig. B.I.1. Generally, there are 3 main steps:

1. **Implementation and selection of macro-commands:** The macro-commands, including user-define and standard ones, are fundamental to generate the executable file, which is used to run the simulation.

2. **Execution:** The simulation is facilitated and configured thanks to the input file as an interface between source code and user. During the simulation,

---

[1] www.paraview.org

the executable file could produce different output files, i.e. output *gdd* files, output *pvd* file and a *txt* file. The *gdd* and *pvd* files are presented in B.I.2.3. Beside, the output *txt* file records the measured results of different phenomena during DEM simulation, e.g. normal stress, displacement, etc.

3. **Analyses of results:** the *gdd* and *pvd* files could be read and visualized by using *granoo-viewer* and *Paraview*, respectively. The *txt* file could be analyzed by different tools. In this study, the analysis of *txt* file is performed by using of Python scripts.

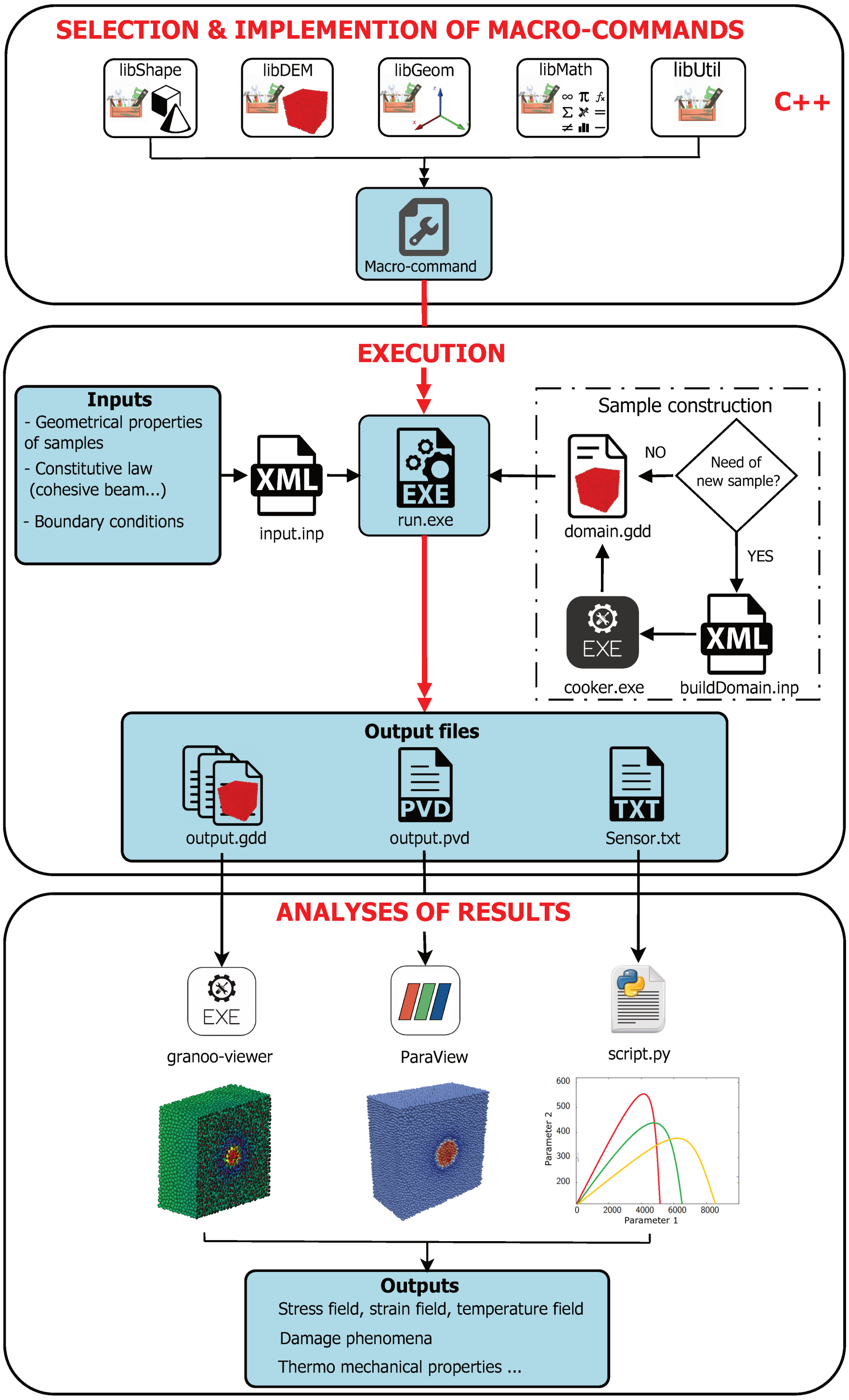

Fig. B.I.1: The main steps of DEM simulations using GranOO

B.I.3 Construction of discrete domain

B.I.3.1 Required properties of discrete domain

In DEM simulation, sample is represented by discrete domain which is an assembly of non deformable spherical discrete elements. Naturally, when a space is filled by an assembly of sphere, voids and overlapping exist. However, in order to mimic the continuous media. the discrete domain must give a good compromise between four important criteria:

- isotropic distribution of elements;
- density of assembly;
- overlapping between elements;
- average direct neighbor number which is calculated as follows:

$$\text{Average direct neighbor number} = \frac{2 \times \text{Number of contacts}}{\text{Number of discrete elements}}$$

Thus, the *cooker* algorithm, dedicated to the domain construction, has been developed in GranOO platform [JATI15]. In this algorithm, discrete element radii are randomly chosen through a uniform distribution with a range equal to 25% [AIlCN12]. This randomization process prevents ordered configuration, also known as crystallization, in the obtained discrete domain [PL01]. The *cooker* algorithm ensures also that the average direct neighbor number is close to 6.2 and the density is about 0.63, in order to produce a good representation of continuous media [GF74, Fin70]. Furthermore, the overlapping between discrete elements could be managed as it will be explained hereafter.

B.I.3.2 Construction domain algorithm

The *cooker* algorithm is able to fill a space of arbitrary shape with spherical discrete elements. Fig. B.I.2 illustrates the main steps of domain construction, which could be divided in 4 main steps:

1. **Random filling:** At the beginning, the discrete elements are randomly added until no longer free space exists. In other words, the random filling is stopped after a given number (to be fixed by the user) of unsuccessful attempts to insert a new discrete element.

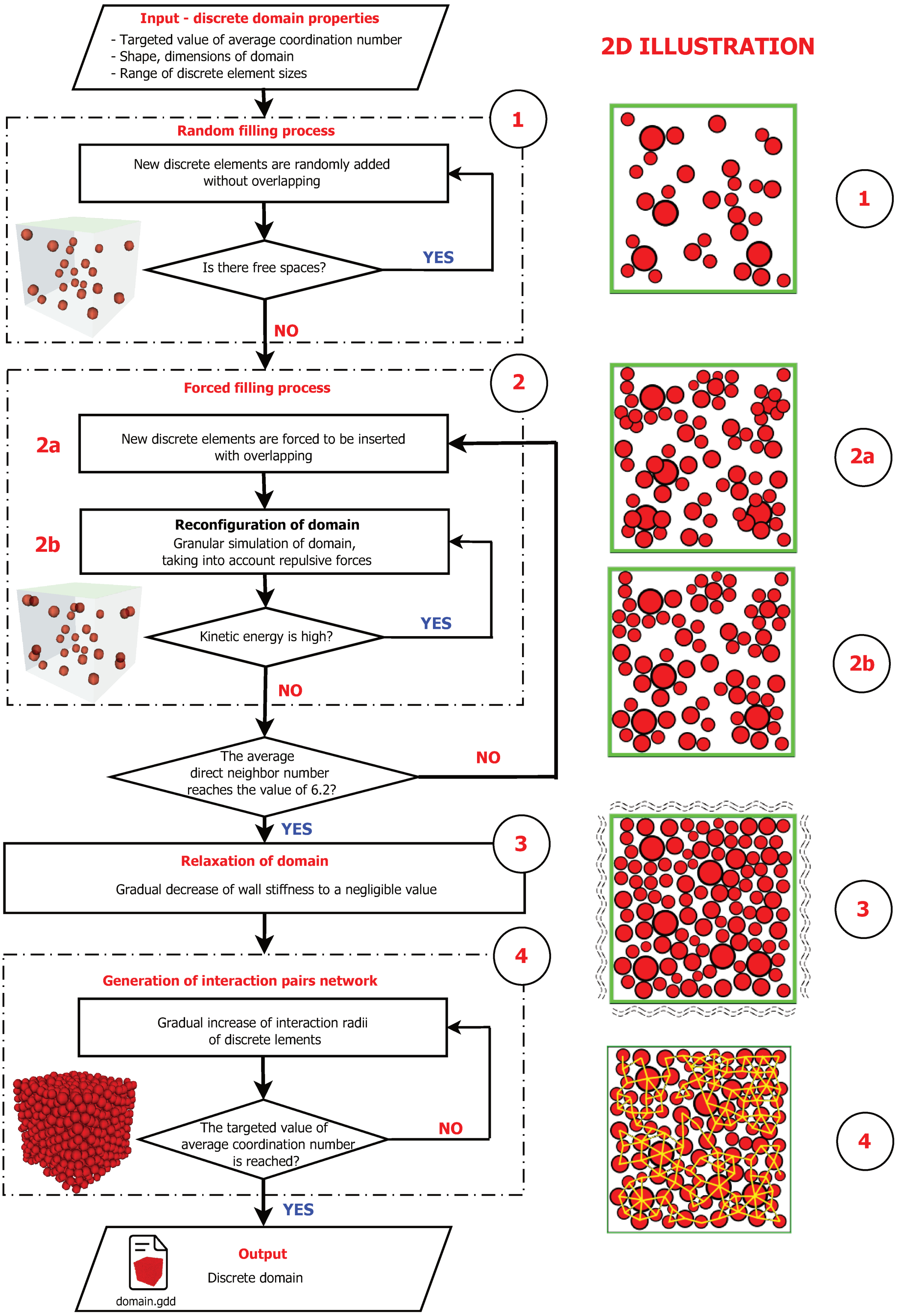

Fig. B.I.2: The main steps of domain construction by using the *cooker algorithm*

2. **Forced filling:** After the random filling, the discrete elements are forced to be inserted by packet, e.g. 1 or 10 elements, until the average direct neighbor number reach the 6.2 value that corresponds to the definition of a random close packing [GF74] (step 2a). Since the discrete elements are forced to be added, a high level of overlapping between elements is induced. Hence, the discrete domain is reconfigured after each forced insertion (step 2b). The reconfiguration of domain is done by performing a granular simulation of domain until the kinetic energy decreases to a negligible value. Once the average direct neighbor number reaches the targeted value, the forced filling step is stopped.

3. **Relaxation of domain:** Once the forced filling is stopped, the discrete domain is relaxed in order to remove the remaining overlapping. This relaxation consists of decreasing the boundary wall stiffness until this stiffness reaches a negligible value.

4. **Generation of interaction pairs network:** As it was shown in [ZYR+18], structural properties of assemblies has strong effects on apparent elastic responses. Therefore, a post-processing step, able to manage the coordination number, has been implemented to study the influence of this input parameter on the macroscopic Young's modulus and Poisson's ratio (Chapter B.II). Hence, after the filling process, a specific algorithm is involved to generate interaction pair network. In this step, the value of the global coordination number, which is the average number of interaction pair per element, can be tuned. In order to reach a targeted value of coordination number, a radius of interaction is assigned to each discrete element in order to generate interaction pairs. More specifically, the radii of interaction of discrete elements are considered to gradually increase until the expected coordination number value is reached. This algorithm allows us to choose the coordination number value and to connect elements even if they are not really in contact.

B.I.4 Thermo-mechanical behavior modeling of continuous media

B.I.4.1 Springs-like interaction laws and their limitations

The elastic behavior of isotropic materials is characterized by Young's modulus and Poisson's ratio. Since the modeling of this behavior with DEM has been intensively studied, several DEM contact models can be found in the literature. As explained in Sect. A.II.3, in the bonded-particle method, proposed by Potyondy *et al.* [PC04], the material is modeled as assembly of nonuniform-sized rigid spherical particles that may be bonded together at their contact points. Mainly, two models of bonds are frequently used in bonded-particle method: contact bond and parallel bond (Fig. B.I.3).

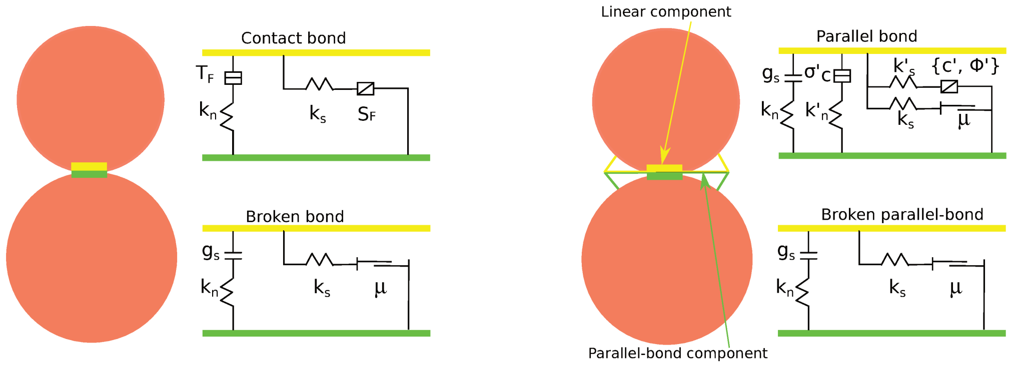

(a) Contact bond model (b) Parallel bond model

Fig. B.I.3: Rheological components of the contact models used in bonded-particle method [Inc18]

The contact bond model can be considered as a pair of elastic springs with constant normal and shear stiffnesses that act at contact points between particles (Fig. B.I.3(a)). These two springs have specific tensile and shear force limits. The bond is broken if the normal force or shear force exceeds the corresponding bond force limits. The broken contact bond has the same behavior than the linear bond, in which the dashpots are replaced by a gap and a friction (Fig. B.I.3(a)). The linear bond is active if and only if the surface gap is less than zero; the force-displacement law is skipped for inactive contacts.[CS79].

By contrast, the parallel bond model, can be considered as a set of elastic springs with constant normal and shear stiffnesses, uniformly distributed over a cross-section lying on the contact plane and centered at the contact point [CMS07]. The cross-section of contact could be rectangular in 2D or circular in 3D. More precisely, the parallel bond model has two components that act parallelly, i.e. parallel-bond component and linear component (Fig. B.I.3(b)). Hence, parallel bond can transmit both force and moment through contact. The transmitted force and moment can be related to maximum normal and shear stresses acting within the parallel-bond component. If one of these maximum stresses exceeds its corresponding bond strength, the parallel bond is broken and becomes linear model (Fig. B.I.3(b)). The properties of contact bond and parallel bond models are synthesized in Tab. B.I.1.

Tab. B.I.1: Properties of contact bond and parallel bond models

Contact bond properties	Parallel bond properties	Descriptions
T_F	-	Tensile force limit [force]
S_F	-	Shear force limit [force]
k_n	k_n	Normal stiffness [force/length]
k_s	k_s	Shear stiffness [force/length]
g_s	g_s	Surface gap [length]
μ	μ	Friction coefficient [-]
-	σ'_c	Tensile strength [stress]
-	c'	Cohesion [stress]
-	ϕ'	Friction angle [degrees]
-	k'_n	Normal stiffness [stress/disp.]
-	k'_s	Shear stiffness [stress/disp.]

The bonded-particle models have been widely used to study fracturing and fragmentation processes of brittle materials. These methods have been implemented in many common DEM softwares, such as PFC [Inc12] and YADE [KD08]. However, one of major drawbacks of the bonded-particle models is that determining the proper set of bond properties (microscopic parameters) is quite difficult. In fact, the input parameters of the model are set at the microscopic scale and they do not correspond to the material properties. A pre-processing step is necessary (calibration process) to reach quantitative results. This drawback is due to the high number of microscopic parameters, for example, 10 microscopic parameters are needed to determine the contact-bonded model [WC17], e.g. contact modulus, stiffness ratio, friction coefficient, contact-bond normal strength, contact-bond shear strength, etc.

More recently, the Cohesive Beam Model (CBM) has been developed by different authors [LHG17, HNKK17, ACI15]. In the CBM proposed by André *et al.* [AIlCN12, ACI15], discrete elements are connected by cylindrical cohesive beams which are able to work in tension, compression, bending and torsion. The Euler-Bernoulli beam theory is implemented to compute the beam forces and moments. In this framework, the behavior of modeled material could be reached by calibrating only two microscopic parameters. The calibration process of this model seems to be less complex than the previous bond models. Hence, the contact model of *Granoo* platform has been implemented by using CBM model, which is presented hereafter.

B.I.4.2 Why cohesive beam model?

The present study focuses on the Cohesive Beam Model proposed by André *et al.* [AIlCN12, ACI15], due to a rather simple calibration process. The CBM was first introduced by H. J. Herrmann in 1988 [Her88]. This model was first used for 2D ordered lattice network [SVM92b, SvM92a], and later, for disordered 2D lattice networks [SG96, KH96, DKR02, **?**, DR06]. In reference [SG96], microscopic parameters of 2D lattice model and mechanical properties of material were proposed to be equal similar. However, the *trial-and-error* calibration has mainly been recommended, using experimental and numerical approaches to determine relationships between microscopic and macroscopic outputs of CBM. In the present study, mechanical properties of the cohesive beams are different from corresponding properties of modeled material. So, microscopic local properties could be tuned to produce the targeted behaviors at the macroscopic scale.

Fig. B.I.4 draws two discrete elements bonded by a cohesive beam. The cylindrical geometry is chosen because it's dimensional description requires only two independent parameters: a length L_m and a radius R_m. Mechanical properties of cohesive beams are described by a Young's modulus E_m and a Poisson's ratio ν_m. These four microscopic geometric and mechanical parameters allow a complete description of a cohesive beam. Hereafter, in order to distinguish micro from macro properties, micro parameters and macro parameters are denoted by 'm' and 'M' indexes, respectively. In addition, in this contact model, cohesive beams are massless; mass properties are then assigned only to discrete elements.

For the sake of clarity Fig. B.I.5 shows a configuration in which the discrete elements have been moved away. The cohesive beam is symbolized by its median line. Both cohesive bond ends are fixed to the discrete element centers O_1 and O_2. The discrete element frames $\mathcal{F}_1\left(O_1, \mathbf{X_1}, \mathbf{Y_1}, \mathbf{Z_1}\right)$ and $\mathcal{F}_2\left(O_2, \mathbf{X_2}, \mathbf{Y_2}, \mathbf{Z_2}\right)$ are oriented such that $\mathbf{X_1}$ and $\mathbf{X_2}$ are normal to the beam cross section ends. At

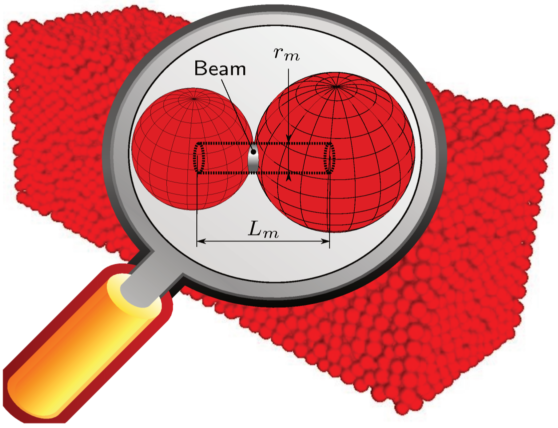

Fig. B.I.4: The cohesive beam bond [AIlCN12]

the initial time, the beams are relaxed (Fig. B.I.5(a)). Fig. B.I.5(b)) shows the cohesive beam in a arbitrary loading state.

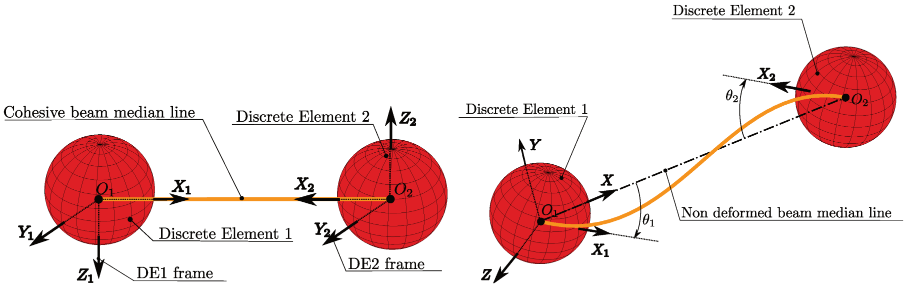

(a) Relaxing state

(b) Loading state

Fig. B.I.5: Cohesive beam bond configurations [AIlCN12]

The well-known analytic model of Euler-Bernoulli beam [Tim82] is used in this contact beam model to describe the interactions between elements. Fig. B.I.5(b) illustrates the beam local frame positioning. The center of discrete element 1 (O_1) is considered as the origin. The "aligned" configuration, in which $\mathbf{O_1O_2} = k\mathbf{X_1} = -k\mathbf{X_2}$, is considered as the non-bending state and is taken as reference. Consequently, the cohesive beam local frame $\mathcal{F}(O, \mathbf{X}, \mathbf{Y}, \mathbf{Z})$ is oriented such that (see Fig. B.I.5(b)):

$$\mathbf{X} = \frac{\mathbf{O_1O_2}}{\|\mathbf{O_1O_2}\|} \text{ and } \mathbf{Y} = \mathbf{X} \wedge \mathbf{X_1} \text{ and } \mathbf{Z} = \mathbf{X} \wedge \mathbf{Y}$$

In the local frame $\mathcal{F}$, the deflections at O_1 and O_2 are null. Cross section bending rotations at O_1 and O_2 are defined, respectively, by $\theta_1 = (\widehat{\mathbf{X}, \mathbf{X_1}})$ and $\theta_2 = (\widehat{-\mathbf{X}, \mathbf{X_2}})$. In addition, the small rotation hypothesis is used at local frame to make the following equalities applicable: $\theta_1 = \sin\theta_1$, $\theta_2 = \sin\theta_2$. In *GranOO* framework, θ_1 and θ_2 are assumed to be smaller than 10°. Consequently, the force and torque reactions acting on discrete elements 1 and 2 are:

$$\mathbf{F_{DE1}} = +E_m A_m \frac{\Delta l_m}{l_m}\mathbf{X} - \frac{6E_m I_m}{l_m^2}\left(\left(\theta_{2z} + \theta_{1z}\right)\mathbf{Y} + \left(\theta_{2y} + \theta_{1y}\right)\mathbf{Z}\right) \tag{B.I.7}$$

$$\mathbf{F_{DE2}} = -E_m A_m \frac{\Delta l_m}{l_m}\mathbf{X} + \frac{6E_m I_m}{l_m^2}\left(\left(\theta_{2z} + \theta_{1z}\right)\mathbf{Y} - \left(\theta_{2y} + \theta_{1y}\right)\mathbf{Z}\right) \tag{B.I.8}$$

$$\mathbf{T_{DE1}} = +\frac{G_m Io_m}{l_m}\left(\theta_{2x} - \theta_{1x}\right)\mathbf{X} - \frac{2E_m I_m}{l_m}\left(\left(\theta_{2y} + 2\theta_{1y}\right)\mathbf{Y} - \left(\theta_{2z} + 2\theta_{1z}\right)\mathbf{Z}\right) \tag{B.I.9}$$

$$\mathbf{T_{DE2}} = -\frac{G_m Io_m}{l_m}\left(\theta_{2x} - \theta_{1x}\right)\mathbf{X} - \frac{2E_m I_m}{l_m}\left(\left(2\theta_{2y} + \theta_{1y}\right)\mathbf{Y} - \left(2\theta_{2z} + \theta_{1z}\right)\mathbf{Z}\right) \tag{B.I.10}$$

where:

- $\mathbf{F_{DE1}}$ and $\mathbf{F_{DE2}}$ are the beam force reactions acting on discrete elements 1 and 2.
- $\mathbf{T_{DE1}}$ and $\mathbf{T_{DE2}}$ are the beam torque reactions acting on discrete elements 1 and 2.
- Beam force and torque reactions are expressed in the beam local frame $\mathcal{F}\left(O, \mathbf{X}, \mathbf{Y}, \mathbf{Z}\right)$.
- l_m and Δl_m are the initial beam length and the longitudinal extension.
- $(\theta_{1x}, \theta_{1y}, \theta_{1z})$ and $(\theta_{2x}, \theta_{2y}, \theta_{2z})$ are respectively the components of rotations vectors of cross section of the beam at the points O_1 and O_2, expressed in the beam local frame: $\boldsymbol{\theta}_{\mathbf{DE1}} = \boldsymbol{\theta}_{\mathbf{DE1}}(\theta_{1x}, \theta_{1y}, \theta_{1z})$; $\boldsymbol{\theta}_{\mathbf{DE2}} = \boldsymbol{\theta}_{\mathbf{DE2}}(\theta_{2x}, \theta_{2y}, \theta_{2z})$
- A_m, I_m and Io_m are the beam cross section area, second moment of area and polar second moment of area along $\mathbf{Y}$ and $\mathbf{Z}$
- E_m and G_m are the Young's and shear modulus of the cohesive beam.

As described previously, the cohesive beam bond is defined by four parameters: length L_m , radius R_m, Young's modulus E_m and Poisson's ratio ν_m. In fact, the cohesive beam length value L_m depends on the distance between discrete element centers and is not a free parameter because it is defined through the compact process (section B.I.3). In addition, the ν_m has no influence on the macroscopic elastic behavior [AIlCN12]. In this study, the beam radius ratio denoted by r_m is preferred to the beam radius R_m. The beam radius ratio is defined as the ratio between the cohesive beam radius and the average discrete element radius. The r_m value is the same for all the cohesive beams involved in a discrete model. Consequently, elastic behavior of materials could be macroscopically matched by calibrating only two parameters E_m and r_m. This allows us to consider the cohesive beam as a *length-free model*. In other words, the mechanical elastic property of a discrete sample, defined by its apparent Young's modulus and Poisson's ratio, do not depend on its size. This is an important feature of the cohesive beam model.

B.I.4.3 Calibration of cohesive beam elastic parameters

B.I.4.3.a Tensile test simulation and computational methods of macroscopic mechanical responses

In discrete element models, macroscopic outputs can not be introduced directly as input parameters. Indeed, they need to be measured numerically through numerical simulations. In this study, quasi-static uniaxial tensile test are simulated to deduce the apparent Young's modulus E_M, Poisson's ratio ν_M and failure strength σ_M. For such simulations, cubic samples are built by using the *cooker algorithm* (see previous section), with *length of 2 millimeters* and contains *around 10,000 discrete elements*. As it was shown in [AIlCN12, AJI$^+$13, ALTDH17], for a cubic domain, the quantity of *10,000 discrete elements* ensures a good level of convergence. In other words, if higher numbers of element are chosen, the obtained results will not be different from those ones obtained with *10,000 elements*. Consequently, in this study, a number of *10,000 discrete elements* is considered as sufficient for an acceptable level of precision.

In order to load the sample, opposite displacements at constant velocity are imposed to the discrete elements that belong to the S_{x+} and S_{x-} faces of these cubic domains (Fig. B.I.6). The normal forces F_{x+} and F_{x-} resulting from these displacements are measured by summing the measured forces $\mathbf{f_i}$ of each discrete element that belong to S_{x+} and S_{x-} faces:

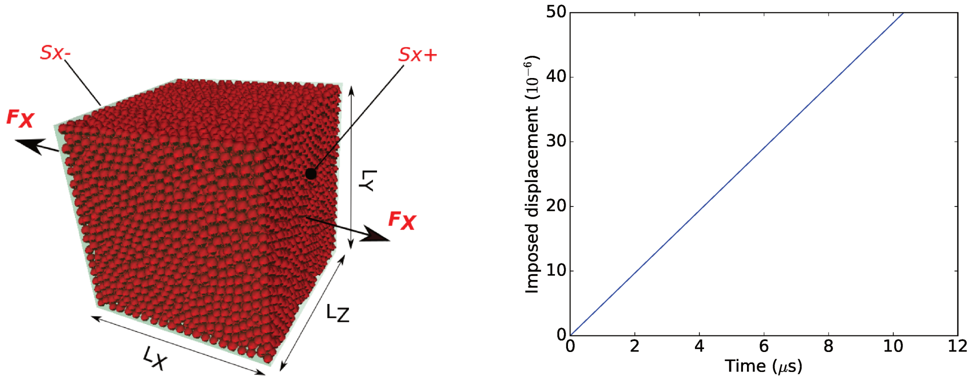

(a) The cubic discrete domain used to perform tensile tests simulation

(b) Kinetic load during a quasistatic tensile test (time step $\Delta t = 1.03 \cdot 10^{-9}s$ and number of iterations $n = 10000$)

Fig. B.I.6: Configuration of tensile test simulation

$$F_{x-} = \sum_{i \in S_{x-}} \mathbf{f_i}.\mathbf{x}$$

$$F_{x+} = \sum_{i \in S_{x+}} \mathbf{f_i}.\mathbf{x}$$

During the tensile simulations, the normal force F_x is computed by averaging these two opposite forces :

$$F_x = \frac{1}{2}(F_{x-} - F_{x+})$$

The lengths L_x, L_y and L_z of the bounding box associated to the discrete domains are updated during the computation. From the knowledge of the bounding box lengths and the applied force F_x (Fig. B.I.6(a)), the average macroscopic normal stress σ_{Mxx} along the x axis can be deduced as:

$$\sigma_{Mxx} = \frac{F_x}{L_y \times L_z} \tag{B.I.11}$$

The macroscopic engineering strain ε_{Mxx} , ε_{Myy} and ε_{Mzz} along the x, y and z axes are expressed as :

$$\varepsilon_{Mxx} = \frac{\Delta L_x}{L_x} \quad \varepsilon_{Myy} = \frac{\Delta L_y}{L_y} \quad \varepsilon_{Mzz} = \frac{\Delta L_z}{L_z} \tag{B.I.12}$$

So, the macroscopic Young's modulus E_M is :

$$E_M = \frac{\sigma_{Mxx}}{\varepsilon_{Mxx}} \tag{B.I.13}$$

The macroscopic Poisson's ratio ν_M is computed by averaging the macroscopic Poisson's ratio values along the y and z axes as :

$$\nu_M = \frac{1}{2}(\nu_{My} + \nu_{Mz}) = -\frac{1}{2}(\frac{\varepsilon_{Myy}}{\varepsilon_{Mxx}} + \frac{\varepsilon_{Mzz}}{\varepsilon_{Mxx}}) \tag{B.I.14}$$

Finally, the macroscopic failure stress σ_M is the macroscopic tensile stress σ_{Mxx} when the failure occurs. The failure at the scale of structure is detected by a brutal decrease of normal stress.

B.I.4.3.b Classical trial-and-error calibration method

This section describes briefly the classical trial-and-error calibration method, introduced by André *et al.*, in order to quantify the value of the microscopic parameters to fit the targeted macroscopic properties [AIlCN12, JATI15]. In these researches, only two microscopic parameters need to be calibrated, i.e. microscopic Young's modulus E_m and beam radius ratio r_m (Sect. B.I.4.2). Hence, to analyze the evolution of macroscopic outputs versus microscopic parameters, several simulations of quasi-static uniaxial tensile test need to be performed with different value of cohesive beam properties. According to the parametric study in [JATI15], macroscopic Poisson's ratio ν_M is independent from microscopic Young's modulus E_m. By contrast, both macroscopic Young's modulus E_M and Poisson's ratio ν_M are nonlinearly dependent upon r_m. Therefore, the calibration process can be achieved in two main steps:

1. the calibration of the microscopic beam radii by dichotomy in order to reach the required value of Poisson's ratio ν_M and then
2. the calibration of the microscopic beam Young's modulus in order to reach the required value of Young's modulus E_M. This calibration is accomplished by using a linear regression since E_M is proportional to E_m.

This calibration method involves fastidious parametric study of several simulations, which is time consuming and non-normalized. For example, the calibration process to reach the targeted elastic properties of one material involves 10 simulations which could take 4 hours to perform. In order to avoid repeating trial-and-error calibration and facilitate the usage of DEM for non-specialists, a

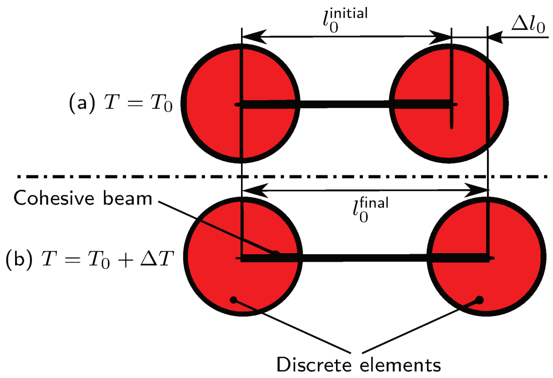

Fig. B.I.7: Thermal expansion of the cohesive beams at the initial temperature T_0 (a) and at a given temperature T (b)

direct calibration method of microscopic parameter of DEM has been established in the present work and is presented in chapter B.II.

B.I.4.4 Thermal expansion modeling

In this study, the thermal expansion is modeled by using the solution proposed by André *et al.* [ALTDH17]. This solution consists in incrementing the free length of the cohesive beams l_0 by a Δl_0 value computed from the temperature variation ΔT (see Fig. B.I.7). It could generate the thermal expansion of the whole domain without adding any internal forces, in the case of homogeneous isotropic material and homogeneous temperature in the whole volume. In this approach, the free length of cohesive beams is linearly dependent on temperature (Eq. B.I.15)

$$l_0(T) = l_0^{\text{initial}}(1 + \Delta(T) \times \alpha) \tag{B.I.15}$$

where $\Delta(T) = T - T_0$ is the temperature variation, α is the linear thermal expansion coefficient and l_0^{initial} is the initial free length for the initial temperature T_0. Please notice that the current length l is not directly affected by these computations. Changing the current length l, for the given cohesive beam, could change the reaction forces acting on the bonded discrete elements. To avoid this issue, if the related discrete elements are unconstrained, the current length l of the beam converges toward the most updated value of its free length l_0 after a given number of iterations.

Similar to the mechanical microscopic parameters, the linear thermal expansion is considered at two scales : microscopic α_m and macroscopic α_M. The α_m is the input parameter related to the thermal expansion coefficient of the cohesive beams and the α_M is the resulting thermal expansion of the bounding shape of the discrete domain. According to the analysis in [ALTDH17], the thermal expansion is identical at microscopic and macroscopic scales. Therefore, thermal expansion coefficient can be introduced directly without any calibration.

B.I.4.5 Thermal conduction modeling

The temperature filed exhibits an important role in many manufacturing processes, such as steel casting, machining, etc. Conduction is the most predominant mode of heat transfer within a solid or between solids in physical contact. Nevertheless, quite a few other DEM researches on this phenomena could by found in the literature [HGF14, Flo18]. Terreros *et al.* has developed an original method to simulate heat conduction within continuous media using DEM [**?**, JATI15]. The method proposed by Terreros *et al.* has been implemented in *GranOO* and has been validated through several thermal test simulations, e.g. cylindrical beam in contact with a hot plane, dynamically heated sheet. The DEM results shown a good agreement with analytical results and FEM results, which proved the compatibility of the proposed method to model thermal conduction phenomena in continuous media [**?**]. In the present study, since the temperature field was considered to be uniform in the whole sample, the thermal conduction was not be taken into account.

B.I.5 Virial stress and microscopic fracture model

B.I.5.1 Standard fracture model and its limitations

In discrete element approach, damage within the material is simulated by breaking the cohesive beam that connect discrete elements. Different criteria have been established in literature, e.g. maximal bond stress or maximal bond strain. In the research of André *et al.* [And12], the authors introduced a maximum bond stress criterion to study brittle material. The introduced failure model is based on the Euler-Bernoulli beam theory [Wit91] and Rankine criterion. The maximum principal stress of a cohesive beam is given by Eq. B.I.16.

$$\sigma_I = \frac{1}{2}\left(\sigma_{max} + \sqrt{\sigma_{max}^2 + 4\,\tau_{max}^2}\right) \tag{B.I.16}$$

where σ_{max} is the maximal normal stress (due to tensile and bending loadings) and τ_{max} is the maximal shear stress (due to torsion loading) (Fig. B.I.8).

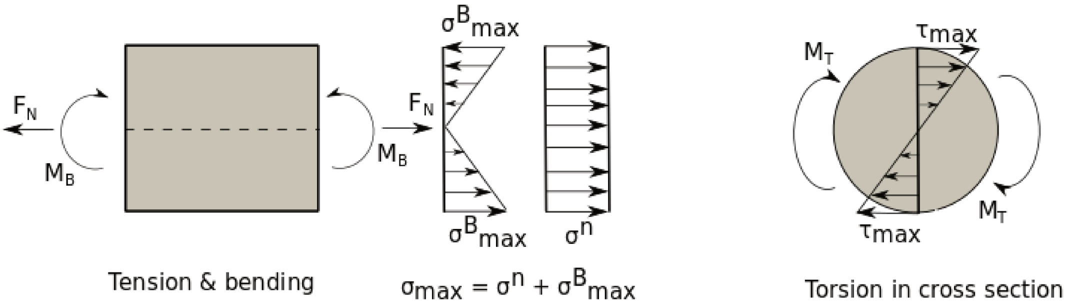

Fig. B.I.8: Stress distributions of a cylindrical beam under tension, bending and torsion, according to Euler-Bernoulli beam theory

The cohesive beam is broken if the maximal equivalent Rankine stress σ_{max} is higher than the tensile strength of the beam σ_m:

$$\sigma_I \geq \sigma_m \tag{B.I.17}$$

This fracture model has been applied to different fracture test simulations, i.e. tensile test and torsion test on cylindrical discrete domain and bending test on parallelepiped discrete domain [JATI15]. The crack path obtained by these tests were compatible with theoretical predictions and experimental observations, for example, in torsion test, the simulated crack surface is oriented 45° to the main axis of sample (Fig. B.I.9(a)). However, in the application to indentation test with a spherical indenter, this model could not produce reasonable results in term of crack geometry. Indeed, the simulations with the standard failure criterion produce a crack that occurs near the indenter and propagates throughout the thickness of the material (Fig. B.I.9(b)). Whereas, the experimental observation show a crack in form of a Hertzian cone [Roe56]. This could be explained by the fact that in beam-based fracture criterion, the state of stress at each discrete element is not describe by an stress tensor. By contrast, in this fracture model, damage is modeled by taking account only a scalar threshold of cohesive beam (Eq. B.I.17), which may not be representative for the cases of complex loadings. More recently, in order to overcome the limitations of beam-based fracture model, the virial-stress-based fracture criterion has been developed. This will be introduced in the next section.q

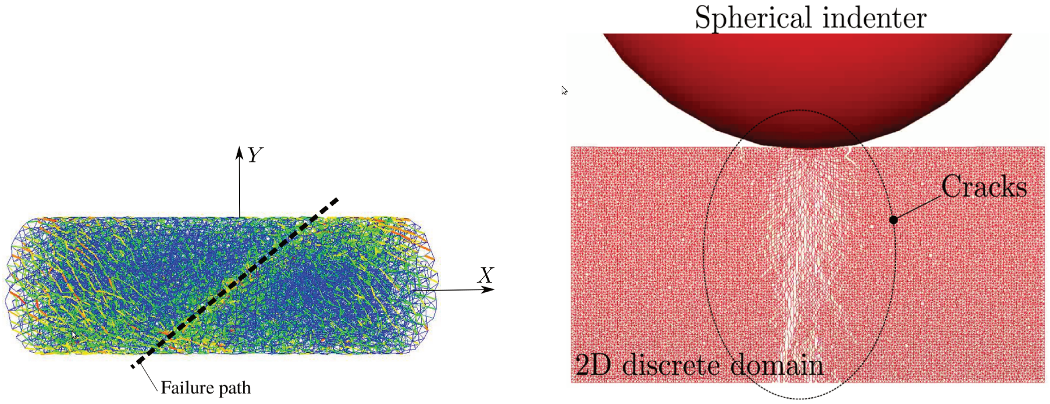

(a) Torstion simulation (b) 2D indentation simulation

Fig. B.I.9: Crack path obtained with beam-based fracture criterion, taken from [JATI15]

B.I.5.2 Virial stress formulation

The virial stress approach was initially developed to measure stress in Molecular Dynamic (MD). This formalism is a generalization of the virial theorem of Clausius (1870) for gas pressure. Since the new millennium, it has been widely implemented in different discrete methods [WKC12, TSVA15, RAHA13]. Several researches have pointed out that virial stress-based model seems to be suitable to simulate elastic brittle material [AJI+13, JDIG17, HLG+15]. This approach enables the stress computation at the scale of discrete elements and therefore, bridges the discrete and continuum mechanics. Mainly, virial stress tensors are used as post-processing tool to compute stress fields in DEM calculation. Recently, André *et al.* [AJI+13, JATI15] proposed a fracture criterion at discrete element scale, based on the computation of an equivalent Cauchy stress tensor (the so-called virial stress tensor), to model damage within brittle materials. In order to ensure the symmetry condition of the stress tensor, the same authors made a slight modification of the formulation introduced by Zhou [Zho03] to compute virial stress tensor (Eq. B.I.18).

$$\overline{\overline{\boldsymbol{\sigma}}}_i = \frac{1}{2\Omega_i}\left(\frac{1}{2}\sum_{j=1}^{N}\left(\mathbf{r}_{ij}\otimes\mathbf{f}_{ij}+\mathbf{f}_{ij}\otimes\mathbf{r}_{ij}\right)\right) \tag{B.I.18}$$

where :

- Ω_i is the volume of discrete element i,
- $\overline{\overline{\boldsymbol{\sigma}}}_i$ is the equivalent Cauchy stress tensor of the considered volume Ω,

- j takes values 1 to N neighbors of the discrete element i,
- $\otimes$ is the tensor product between two vectors,
- $\mathbf{f}_{ij}$ is the force imposed on the discrete element i by a cohesive beam that bonds the discrete element i to its "neighbor discrete element" j,
- $\mathbf{r}_{ij}$ is the relative position vector between the center of the two bonded discrete elements i and j.

Consequently, thanks to virial stress concept, the state of stress at a discrete element could be well described by an equivalent Cauchy stress tensor. In this virial formulation, only the interactions between the associated discrete element and its direct neighbor are considered (Fig. B.I.10(a)). In the case of indentation tests, the virial-based model reproduce a Hertzian cone crack, which is compatible with experimental observation (Fig. B.I.10(b)). These results reveal that the virial-based fracture model seems to be able to describe more precisely the cracking propagation issued from complex loading than the beam-based approach.

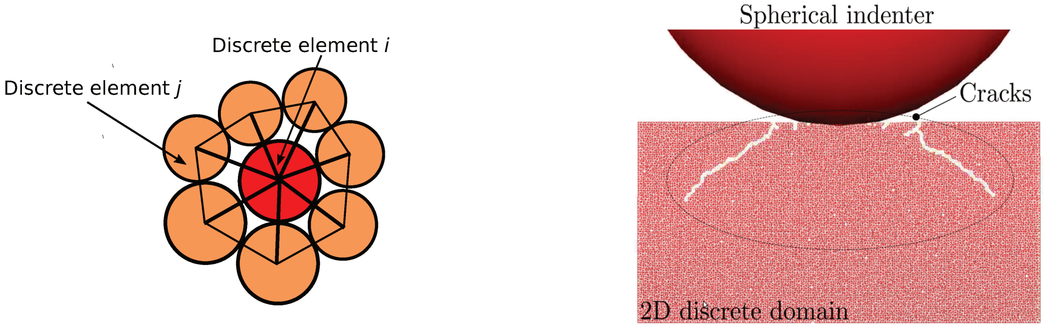

(a) 2D illustration of the concept of virial stress computation

(b) 2D simulation of indentation test with virial-stress-based [JATI15]

Fig. B.I.10: Virial stress formulation and associated results

B.I.5.3 Novel development of virial stress formulation

In the present study, a new formulation has been proposed to improve the accuracy of virial stress tensor, by considering several neighbor level as explained hereafter (Eq. B.I.19).

$$\overline{\overline{\boldsymbol{\sigma}}}_{\Omega} = \frac{1}{2\Omega} \sum_{i \in \Omega} \left(\frac{1}{2} \sum_{j=1}^{N} \left(\mathbf{r}_{ij} \otimes \mathbf{f}_{ij} + \mathbf{f}_{ij} \otimes \mathbf{r}_{ij} \right) \right) \tag{B.I.19}$$

where:

- Ω is the volume associated to the virial stress computation,
- $\overline{\overline{\boldsymbol{\sigma}}}_{\Omega}$ is the equivalent Cauchy stress tensor of the considered volume Ω,
- j takes values 1 to N neighbors of the discrete element i,
- $\otimes$ is the tensor product between two vectors,
- $\mathbf{f}_{ij}$ is the force imposed on the discrete element i by a cohesive beam that bonds the discrete element i to its "neighbour discrete element" j,
- $\mathbf{r}_{ij}$ is the relative position vector between the center of the two bonded discrete elements i and j.

As illustrated in Fig. B.I.11, the stress tensor is always computed for the *central* discrete element. Thus, different volumes Ω can be considered depending on the *neighbor level*. Neighbor elements that connect directly to the central element through cohesive beams are defined as *neighbor level 1*. Discrete elements that connect directly to the discrete elements in *neighbor level 1* are defined as *neighbor level 2* and so on. The volume Ω is simply defined as :

$$\Omega = \frac{1}{f_v} \sum_{i \in \Omega} \Omega_i \tag{B.I.20}$$

where :

- i is related to a discrete element;
- Ω_i is the volume of the discrete element i;
- f_v is the global volume fraction of the discrete domain.

With such a model, high value of neighbor level corresponds to non-local stress tensor whereas low value of neighbor level is related to local value with lower precision. The accuracy of different *neighbor levels* have been examined in order to choose the most appropriate configuration.

Several simulations of tensile tests with neighbor levels 1 and 2 were carried out. The tensile test simulations followed the same principles that was described in B.I.4.3.a. In the performed simulation, the value of microscopic Young's modulus E_m was arbitrary fixed at 500 GPa. Radius ratio was set from 0.2 to 1.0 and the coordination number varied from 6 to 13. Based on obtained results, the average

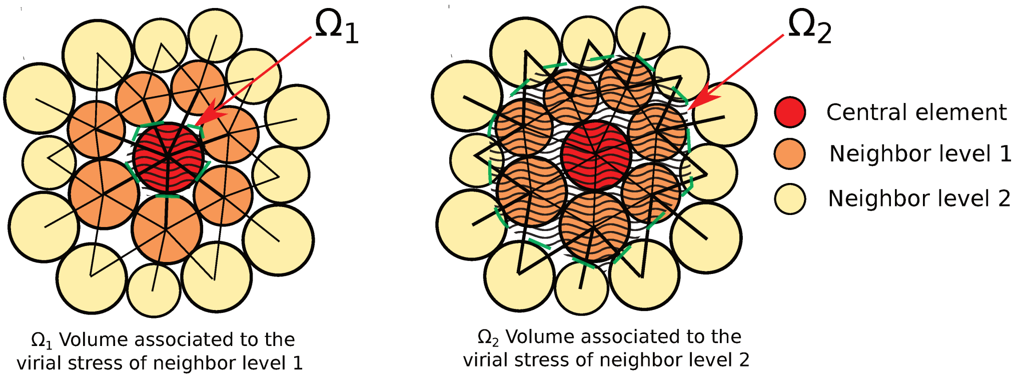

Fig. B.I.11: 2D illustration of neighbor levels used for virial stress computation

value of the xx component of local virial stress tensor $< \sigma_{m_{xx}} >$ was computed. The macroscopic normal stress $\sigma_{M_{xx}}$ was also computed thanks to Eq. B.I.11. The relative difference between $< \sigma_{m_{xx}} >$ and $\sigma_{M_{xx}}$ was then computed by the following equation.

$$\text{difference} = \frac{< \sigma_{m_{xx}} > - \sigma_{M_{xx}}}{\sigma_{M_{xx}}} \times 100 \tag{B.I.21}$$

In Eq. B.I.21, the discrete elements in the loaded boundaries were not taken into account in the computation of $< \sigma_{m_{xx}} >$. This could be explained by the fact that, in the performed simulations, the value of virial stress in the loaded boundaries was lower than in other areas of discrete domain.

The results of the case $cn = 10$ are summarized in Table B.I.2. These results show that simulations with *neighbor level 2* have lower difference between $\sigma_{M_{xx}}$ and $< \sigma_{m_{xx}} >$ (lower than 2%). The same tendency was observed for other coordination numbers. Consequently, the *neighbor level 2* seemed to ensure a good compromise between computation accuracy and time consumption. Hence, this configuration will be used to perform DEM simulations in the present study.

Tab. B.I.2: **Relative differences between local virial stress and global normal stress**

r_m	lv 1	lv 2
0.2	1.48%	0.66%
0.4	1.28%	1.25%
0.6	1.44%	1.38%
0.8	1.59%	1.42%
1.0	1.62%	1.51%
Averaged errors	1.48%	1.24%

B.I.5.4 Fracture model based on virial stress

B.I.5.4.a Fracture mechanism at microscopic scale

The present work has focused on brittle fracture which is assumed to be initiated under tensile stress in *mode I*. Therefore, two fracture criteria at the scale of discrete element were proposed to model the fracture phenomena. The first criterion, called *Rankine criterion*, is related to the maximum principal stress. Whereas the second criterion, called *Hydrostatic criterion*, is related to hydrostatic stress.

In the *Rankine criterion*, a computation of the maximal principal stress σ_I is required. Indeed, σ_I is deduced from the virial stress tensor $\overline{\overline{\sigma}}_\Omega$ thanks to the linear algebra computations that able to compute eigenvalues $(\sigma_{XX}, \sigma_{YY}, \sigma_{ZZ})$ of symmetric matrices [Str88]. The maximal principal stress is simply deduced as:

$$\sigma_I = \max(\sigma_{XX}, \sigma_{YY}, \sigma_{ZZ}) \tag{B.I.22}$$

If the maximal principal stress associated to an element exceeds the microscopic Rankine fracture threshold σ_m^{ran}, some of its connected cohesive beams will be broken:

$$\sigma_I \geq \sigma_m^{ran} \tag{B.I.23}$$

In the *Hydrostatic criterion*, the hydrostatic stress is computed by:

$$\sigma^{hyd} = \frac{1}{3}\,\mathrm{trace}(\overline{\overline{\boldsymbol{\sigma}}})$$

If the hydrostatic stress associated to an element exceeds the microscopic hydrostatic fracture threshold σ_m^{hyd}, some of its connected cohesive beams will be broken:

$$\sigma^{hyd} \geq \sigma_m^{hyd} \tag{B.I.24}$$

In order to describe more precisely the fracture propagation, the cohesive beams that have to be broken should be defined in a reasonable way. In the previous studies of Andé *et al.*, all the beams that belong to a discrete element that reaches the microscopic fracture threshold were broken [AJI+13, JATI15]. As a consequence, a debonded discrete element occurs and a debris is created. In the present study, to avoid this problem, a new microscopic fracture mechanism was proposed: only half of total cohesive beams that belong to the discrete element is broken when the microscopic fracture threshold is reached (Fig. B.I.12). Hence, this half of total beams need to be well defined. Since the brittle failure occurs in tensile mode (mode I), the broken beam set should follow a specific surface. In this research, a specific surface and its associated direction, named the failure surface S_i and the failure direction $\mathbf{d}_i$ respectively, were used to describe the fracture mechanism (Fig. B.I.12). The failure direction $\mathbf{d}_i$ of discrete element i has been assumed to be the direction of the eigenvector of virial stress tensor that corresponds to the maximal principal stress σ_I (Eq. B.I.22).

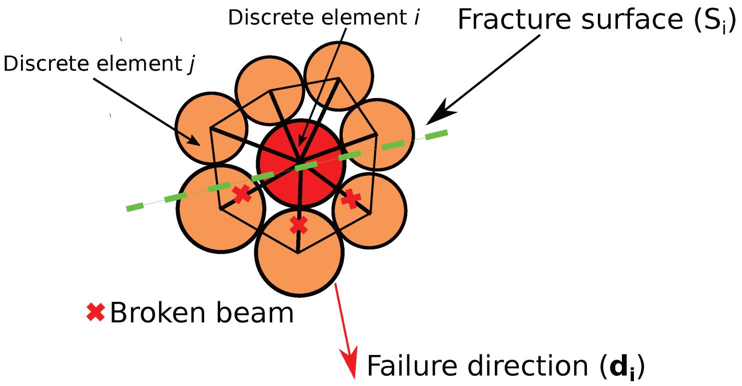

Fig. B.I.12: 2D illustration of the microscopic fracture mechanism

Finally, to mimic the creation of failure surface S_i, the cohesive beams between the discrete elements i and j, included in the neighbor level 1, are broken, assuming the following condition:

$$\mathbf{r}_{ij} \cdot \mathbf{d}_i \geq 0 \tag{B.I.25}$$

where $\mathbf{r}_{ij}$ is the relative position vector between the bonded discrete i and j. This method allows to create a crack path along the surface S_i (Fig. B.I.12).

B.I.5.4.b Comparison of microscopic fracture criteria

A series of tensile test simulations was carried to compare the proposed microscopic fracture criteria. In this task, the Cofer glass was chosen as reference material. Hence, the microscopic parameters were calibrated by using the principle described in B.I.4.3.a. The calibration were accomplished in 2 steps:

1. calibration of r_m and E_m to reach the expected value of Poisson's ratio and Young's modulus ν_M, E_M at macroscopic scale
2. calibration of microscopic fracture thresholds (Eq. B.I.23, B.I.24) to reach the expected value of tensile strength σ_M at macroscopic scale of reference material

The mechanical properties of Cofer glass and related microscopic parameters are summarized in Tab. B.I.3

Tab. B.I.3: Mechanical properties of Cofer glass for the two scales

Macroscopic parameter			Microscopic parameter			
ν_M (-)	E_M (GPa)	σ_M (MPa)	r_m (-)	E_m (GPa)	σ_m^{ran} (MPa)	σ_m^{hyd} (MPa)
0.23	72	50	0.35	677.94	60.08	22.98

The stress-strain curves issued from tensile test simulations with two fracture criteria are illustrated in Fig. B.I.13. In the performed tensile test simulations, the fracture was detected by a sudden decrease of macroscopic normal stress computed during the simulations (Eq. B.I.13). In Fig. B.I.13, as expected, the tensile behavior before the fracture was linear and the maximum value of normal stress were close to the tensile strength of reference material, i.e. 50 MPa. However, the discrepancy between two microscopic fracture criteria arose after the fracture. The *Hydrostatic fracture criterion* seemed to describe more precisely the fracture behavior at macroscopic scale than the *Rankine fracture criterion*, in comparison with theoretical and experimental observations. Indeed, with the *Hydrostatic fracture criterion*, after fracture, the normal stress decreased quickly towards zero value (Fig. B.I.13(a)). Whereas, with *Rankine fracture criterion*, the normal stress after fracture remained significant in comparison with the peak value (Fig. B.I.13(b)). Consequently, the *Hydrostatic fracture criterion* was used

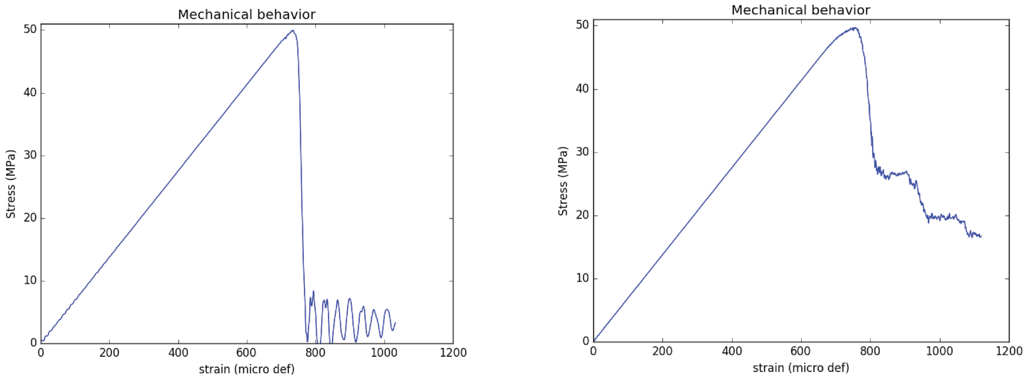

(a) Tensile behavior obtained with Hydrostatic fracture criterion

(b) Tensile behavior obtained with Rankine fracture criterion

Fig. B.I.13: Comparison of proposed microscopic fracture criteria in the following parts of this dissertation to ensure an accurate investigation of influences of damages on the apparent properties of material.

B.I.6 Conclusion

The main objective of this chapter is to explain the GranOO platform and some key elements of the proposed Discrete Element Method, i.e. sample constructions, main steps of a simulations and contact model. In addition, this chapter explained how the proposed Discrete Element Method describes the thermal mechanical behaviors and also fracture phenomena of continuous media. Furthermore, the new developments of virial stress computation are also detailed. Due to the lack of research on application of virial-stress-based modeling to continuous media, several computational configurations were examined, i.e. neighbor levels, microscopic fracture thresholds, microscopic fracture mechanisms (see B.I.5.2). The obtained results show that the proposed microscopic fracture mechanism and the microscopic *Hydrostatic fracture criterion* seem to be able to describe accurately the damage propagation due to complex mechanical loading. These configurations will be used in the next chapters in order to examine the adaptability of the proposed method to study the damage phenomena resulting from thermal expansion mismatch within heterogeneous material.

Chapter B.II

Direct calibration method of microscopic parameter

In the discrete element method, the physical phenomena could be considered in 2 scales: microscopic scale and macroscopic scale. The microscopic scale is related to the properties of the discrete elements and interactions between them. Whereas, the macroscopic scale is related to the apparent properties of the considered material. Generally, the output macroscopic properties are different from the input microscopic parameters. Therefore, the input microscopic parameters needs to be carefully calibrated in order to obtain the expected value of macroscopic properties. Up to now, calibration is usually achieved through a *trial-and-error* procedure in which microscopic parameters are adjusted until the DEM results match the expected macroscopic behavior. Such a calibration step is mandatory to achieve quantitative results but it is a complicated and time consuming process. In order to avoid this *trial-and-error* calibration, the relationships between macroscopic outputs and microscopic parameters, called *micro-to-macro* relationship, has been proposed in many DEM researches for different contact model. However, there is a lack of calibration method that is dedicated to the Cohesive Beam Model (CBM). Thus, this chapter presents a novel calibration method which allows to compute directly the microscopic parameters of CBM from desired properties of the modeled material.

B.II.1 Available calibration methods in literature - a review

Many calibration methodologies has been reported in literature in order to avoid the trial-and-error calibration. Among them, the dimensionless micro-to-macro relationship has been introduced in different researches [FV07, ROLK11, YJL06]. In this calibration method, the evolution of macroscopic outputs are described by functions of dimensionless entities, e.g. ratio between contact stiffness in the normal direction and contact stiffness in the tangential direction. Rojek *et al.* introduced a dimensionless micro-to-macro relationships for 2D and 3D discrete element models [ROLK11]. These authors considered the contact model which was determined by 7 microscopic parameters, i.e. 2 contact stiffnesses, 2 force limits, 2 damping coefficients and Coulomb friction coefficient. In the cited research, the Unconfined Compression Tests (UCT) simulations was used to obtain the Young's modulus, compressive strength and the Poisson's ratio of rock. Whereas, the Brazilian test was used to determine the tensile strength. Simulations of the UCT and Brazilian tests have been performed with different values of stiffness ratio in order to provide specific curves that describe the micro-to-macro relationships. Then, the microscopic parameters could be computed based on the obtained curves. The proposed calibration method were applied for modeling rock cutting and seemed to give satisfactory results. However, this calibration method assumed that the normal and shear force limits were equal. In addition, no analytic function was determined to describe micro-to-macro relationships. An other methodology is the fitting approach, which allows to compute microscopic parameters from macroscopic properties [HWP17]. Han *et al.* propose a fitting function to determine relationship between macroscopic tensile strength and the micro mechanical breakage parameters by using simulations of Brazilian test [HWP17]. The proposed micro-to-macro relationship was then validated through uniaxial tensile tests. In the cited research, the calibration method is applied for only one macroscopic parameter and validated through only one type of numerical experiment. The calibration methods for elastic parameters was not discussed in this research of Han *et al.* The list of the main calibration methods that were proposed in literature for continuous media is presented in Tab. B.II.1. As mentioned previously, in this list, there is a lack of calibration method that is dedicated to the Cohesive Beam Model.

Recognizing this issue, the present study proposes a novel calibration

Tab. B.II.1: List of the main calibration methods in literature

Authors	Contact model	Nb of microscopic parameters in total	Nb of considered microscopic parameters	Considered macroscopic parameters *	Calibration method	Input simulations **	Validation simulations ***
J. Rojek E. Onate (2011)	Spring -like contact	7	4	E ν σ_t	Dimension -less method	Unconfined compressive test (UCS), Brazilian test	Rock cutting
B. Yang, Y. Jiao, (2006)	Parallel -bond	12	4	E ν σ_c	Dimension -less method	Biaxial test	Biaxial test
A. Fakhimi T. Villegas (2006)	Slightly overlapped circular particle interaction	8	4	E ν σ_t	Dimension -less method	UCS, Brazilian test	Biaxial test, Brazilian test
Z. Han, R. Puscasu (2017)	Spring -like contact	6	2	σ_t	Fitting method	Brazilian test	Tensile test

* $E, \nu, \sigma_t, \sigma_c$ are Young's modulus, Poisson's ratio, tensile strength and compressive strength

*The simulations that were used to generate data to analyze the micro-to-macro relationships

***The simulations that were used to validate the proposed micro-to-macro relationships

method which allows direct computation of DEM microscopic parameters from experimental values of mechanical properties of materials. In other words, the mechanical properties of simulated materials could be used directly to perform quantitative DEM simulations. Further more, the influences of arrangement of discrete elements on macroscopic outputs, which has not been discussed in the cited researches (Tab. B.II.1), was also taken into account. The proposed direct calibration method could eliminate the need of repeating trial-and-error calibration and facilitate the usage of DEM for non-specialists. The following section describes in detail the proposed direct calibration method.

B.II.2 Direct calibration of microscopic elastic parameters

B.II.2.1 Tensile test simulations: database to analyze micro-to-macro relationships

In order to define the analytical expressions of *micro-to-macro* relationships in Cohesive Beam Model, data of macroscopic responses need to be generated from a series of simulations with reasonable ranges of microscopic parameters. In this study, the relationships between microscopic parameters and macroscopic outputs of CBM were deduced from simulations results of uniaxial tensile tests, whose the configuration is described in section B.I.4.3.a. The tensile test was used to generate data since all the important mechanical properties that describe a brittle elastic material could be measured by this type of simulation, i.e. Poisson's ratio, Young's modulus and later, the tensile strength. The simulations were carried out with different values of microscopic parameters (Table B.II.2). The total number of simulations was $4 \times 5 \times 5 \times 16 = 1,600$ for this parametric study. Each set of microscopic parameters (r_m, E_m, cn) gives an unique set of macroscopic outputs (ν_M, E_M). Based on the obtained data, nonlinear least squares method [Lev44, Mor78] was applied in order to define the analytical expressions, called *fitting functions*, that best describe the micro-to-macro relationships.

Tab. B.II.2: Value of microscopic parameters

	Values	Tot. number
Sample	1 2 3 4	4
E_m (GPa)	500 1000 1500 2000 2500	5
r_m (-)	0.2 0.4 0.6 0.8 1.0	5
cn (-)	5.5 6 6.5 7 7.5 8 8.5 9 9.5 10 10.5 11 11.5 12.5 13	16

The main steps to define and validate the elastic micro-to-macro relationship are illustrated in Fig. B.II.1. As discussed previously, in CBM, there are 3 microscopic parameters that influence macroscopic outputs: r_m, E_m and cn. Since the determination of analytical expression that contains all of these 3 parameters is not simple, the evolution of elastic macroscopic outputs in function of r_m and E_m was firstly investigated, without influence of cn (see f_1 and f_2 in step 1). Then, the evolution of coefficients that are involved in f_1 and f_2 were studied (step 2).

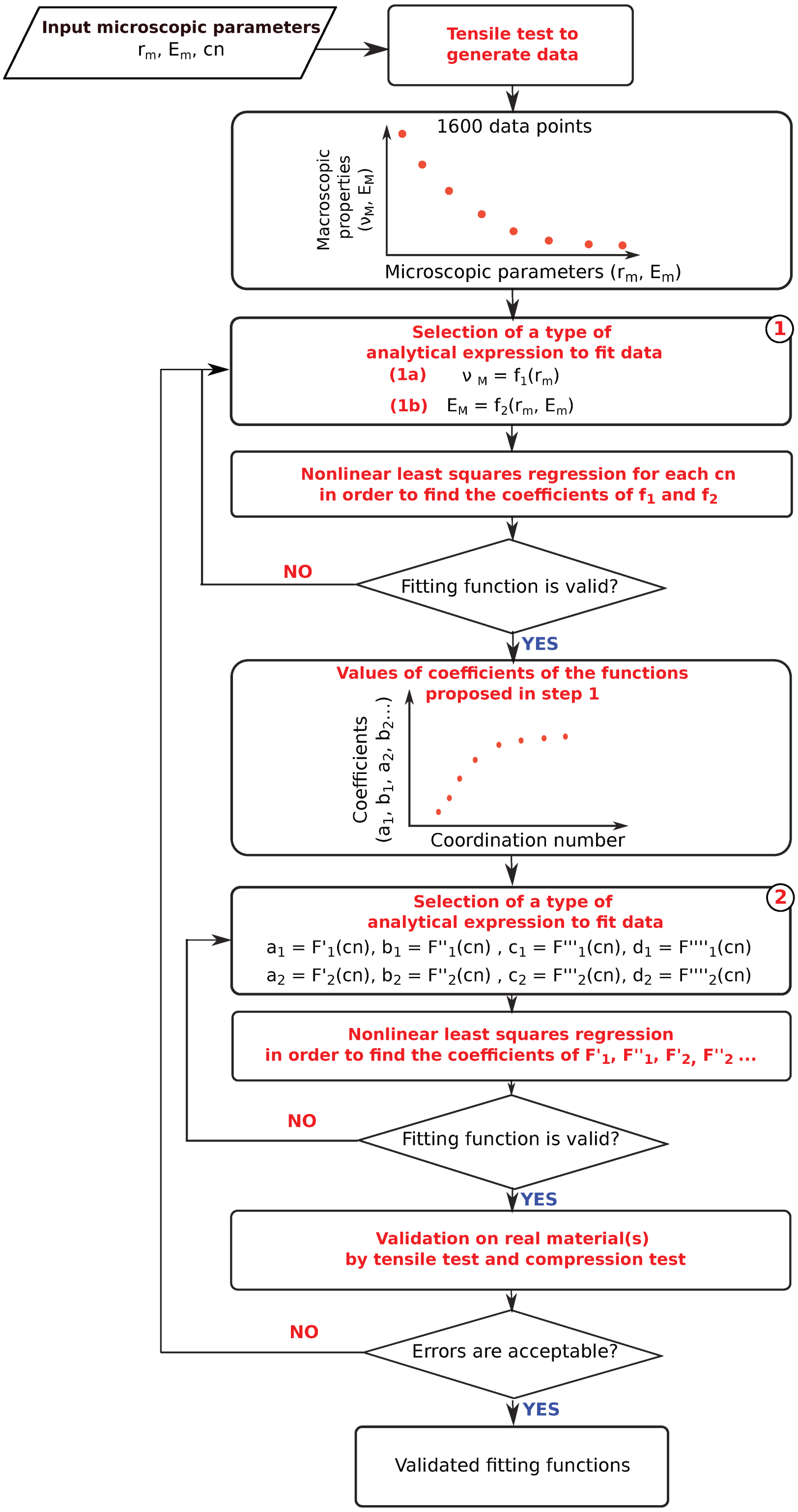

Fig. B.II.1: Main steps to define and validate the elastic micro-to-macro relationships of CBM

The determination of analytical expressions in *step 1* and *step 2* has the same principles which contains two tasks:

- Selection of a type of analytical expression in order to fit the data;
- Refinement of the involved coefficients within the analytical expressions thanks to nonlinear regressions.

After the selection of the most relevant analytical expressions and nonlinear regression, the obtained fitting functions were verified by using academic test cases, i.e. tensile tests and hydrostatic compression tests. The goal of this work is to propose a fast and robust DEM calibration method that allows direct deduction of microscopic parameter values from material properties.

B.II.2.2 Elastic micro-to-macro relationships

B.II.2.2.a Selection of fitting functions - the main principles

There are probably many functions which can describes the micro-to-macro relationships of CBM. Therefore, the following criteria were defined in order to select the *fitting function*:

1. The coefficient of determination must be close to 1: $R^2 \in [0.99; 1]$;
2. The relative difference between the fitted curves/surfaces and the data scatter must be lower than 1%;
3. The evolutions of coefficients involved in fitting functions f_1 and f_2 versus coordination number must be describable by fitting functions F_1', F_2', ...;
4. If many functions satisfy three previous criteria, the function that involves the lowest number of coefficients is chosen;
5. The fitting function must be validated by it's application to different DEM simulations, i.e. uniaxial tensile tests and hydrostatic compression tests.

As shown in Fig. B.II.1, in order to determine the elastic micro-to-macro relationships of CBM, the following steps were carried out :

1a. As it was observed in the previous study of *André et al.* [And12], in this study, macroscopic Poisson's ratio ν_M is independent from microscopic Young's modulus E_m. Therefore, ν_M was firstly considered to depend only on r_m. The following fitting function was investigated: $\nu_M = f_1(r_m)$;

1b. Then, the relationship between macroscopic Young's modulus E_M versus microscopic Young's modulus E_m and radius ratio r_m was studied: $E_M = f_2(E_m, r_m)$;

2. Finally, since the coefficients involved in f_1 and f_2 depend on the coordination number, the following fitting functions was investigated: $a_1 = F_1'(cn)$, $b_1 = F_1''(cn)$, $a_2 = F_2'(cn)$, $b_2 = F_2''(cn)$, ...

B.II.2.2.b Data analyses and nonlinear least squares regression

The nonlinear least square method was used to fit the data resulting from tensile test simulations. The main principles of this type of nonlinear regression are summarized in appendix C.II.5. After examining several fitting functions, the relations $\nu_M = f_1(r_m)$ and $E_M = f_2(E_m, r_m)$ were proposed to be described by the following functions :

$$\nu_M = f_1(r_m) = a_1 + b_1.r_m + c_1.r_m^2 + d_1.r_m^3 \tag{B.II.1}$$

$$E_M = f_2(E_m, r_m) = E_m.(a_2 + b_2.r_m + c_2.r_m^2 + d_2.r_m^3) \tag{B.II.2}$$

The fitted curves and surface, associated to Eq. B.II.1 and B.II.2, are shown in Fig. B.II.2(a) and B.II.2(b).

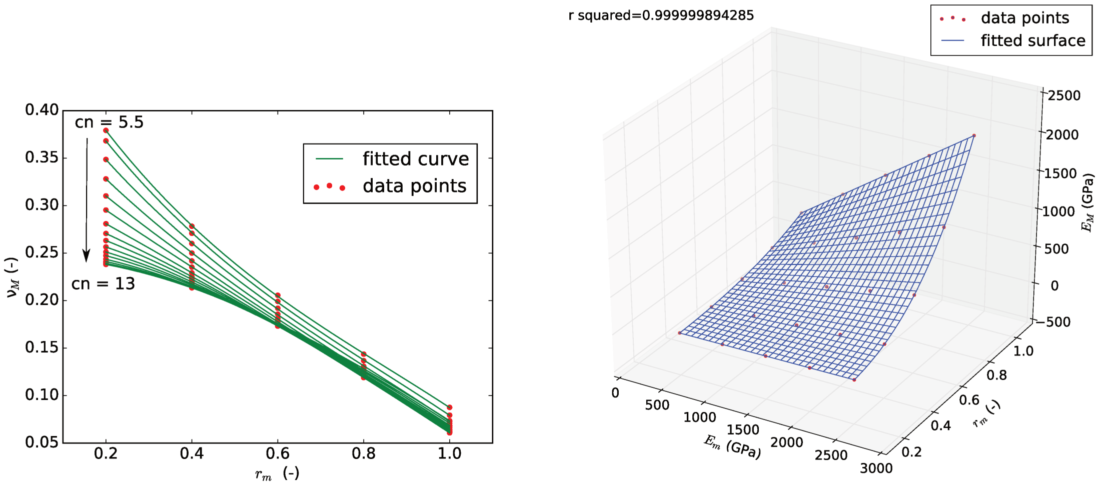

(a) Fitted curve $\nu_M = f_1(r_m)$ corresponding to all values of cn

(b) Fitted surface $E_M = f_2(E_m, r_m)$, case of cn = 6

Fig. B.II.2: Fitted curves and surface for macroscopic Young's modulus and Poisson's ratio

In the considered fitting functions (Eq. B.II.1 and B.II.2), the coefficients a_1, b_1, c_1, d_1 and a_2, b_2, c_2, d_2 depend on coordination number. Again, analytical expressions of relationships between these coefficients and coordination number cn were found by using the nonlinear least squares method. The chosen fitting functions are :

$$\text{coef}_{f1} = F_1(cn) = A_1 + B_1.\tanh[C_1.(cn-7) + D_1] \tag{B.II.3}$$

$$\text{coef}_{f2} = F_2(cn) = A_2 + B_2.cn + C_2.cn^2 + D_2.cn^3 \tag{B.II.4}$$

In these formulas, coef_{f1} is related to a_1, b_1, c_1, d_1 whereas coef_{f2} is associated to a_2, b_2, c_2, d_2. For more clarification, the following expressions describe the evolutions of a_1, b_1, c_1, d_1 and a_2, b_2, c_2, d_2 :

$$a_1 = F_1'(cn); \quad b_1 = F_1''(cn); \quad c_1 = F_1'''(cn); \quad d_1 = F_1''''(cn)$$

$$a_2 = F_2'(cn); \quad b_2 = F_2''(cn); \quad c_2 = F_2'''(cn); \quad d_2 = F_2''''(cn)$$

where: $F_1', F_1'', F_1''', F_1'''$ are different variants of F_1 and $F_2', F_2'', F_2''', F_2''''$ are different variants of F_2.

The fitted curves associated to Eq. B.II.3 are shown and detailed in Fig. B.II.3 and Tab. B.II.3. The fitted curves associated to Eq. B.II.4 are shown and detailed in Fig. B.II.4 and Tab. B.II.4.

Tab. B.II.3: Values of A_1, B_1, C_1, D_1 in Eq. B.II.3

coef_{f1}	A_1	B_1	C_1	D_1
a_1	0.430	-0.185	0.373	0.026
b_1	-0.500	0.503	0.423	-0.079
c_1	0.257	-0.495	0.518	-0.110
d_1	-0.105	0.168	0.602	-0.137

Tab. B.II.4: Values of A_2, B_2, C_2, D_2 in Eq. B.II.4

coef_{f2}	A_2	B_2	C_2	D_2
a_2	-0.0229	0.0145	-0.0021	0.0001
b_2	0.2072	-0.1454	0.0213	-0.0007
c_2	-0.3658	0.2543	-0.0306	0.0011
d_2	-0.0151	0.0270	0.0142	-0.0005

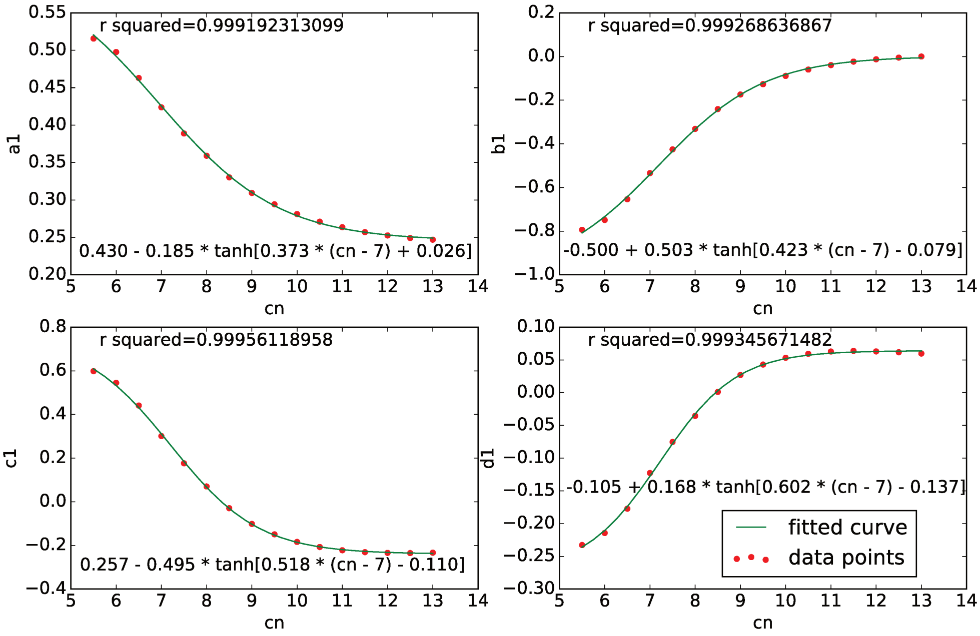

Fig. B.II.3: Fitted curves for a_1, b_1, c_1 and d_1 coefficients of f_1 versus coordination number c_n

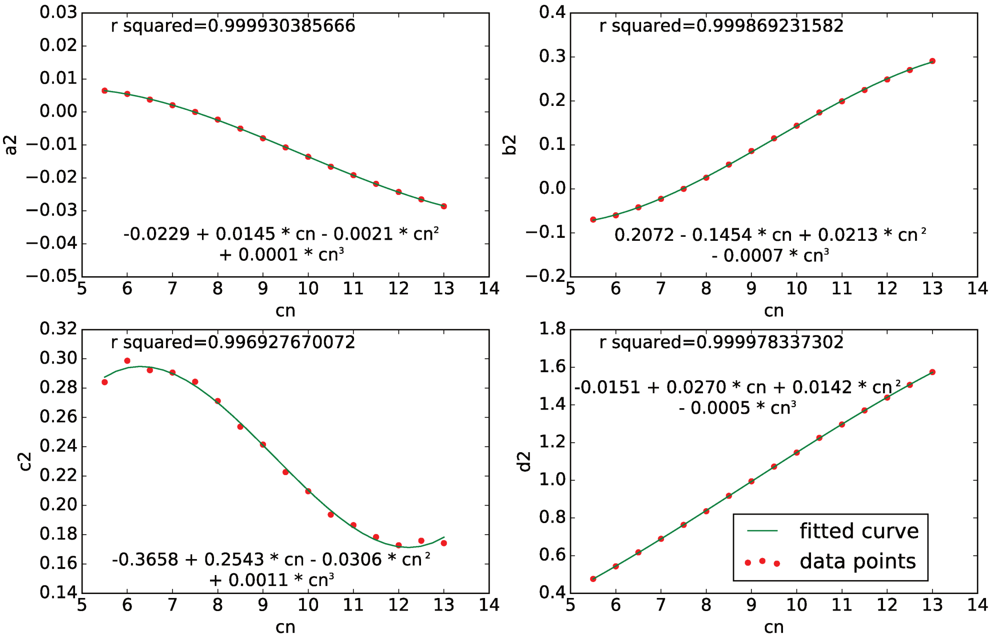

Fig. B.II.4: Fitted curves for a_2, b_2, c_2 and d_2 coefficients of f_2 versus coordination number c_n

As expected, Fig. B.II.2, B.II.3 and B.II.4 reveal that the fitted curves and the fitted surface are in good accordance with data points. More specifically, these curves respect the criterion of coefficient of determination ($R^2 \approx 1$). Hence, the proposed *fitting functions* satisfy the defined fitting criterion. Consequently, the Equations B.II.1, B.II.2, B.II.3 and B.II.4 were chosen to describe the *elastic* micro-to-macro relationships of CBM.

B.II.2.2.c Deduction of microscopic parameters from elastic properties of material - Reverse analysis

As it was shown previously, the proposed *fitting functions* allow us to compute the macroscopic properties from the microscopic parameters of CBM. However, in practice, the purpose is to compute microscopic parameters from macroscopic properties of material in order to performed quantitative DEM simulations. Therefore, in this study, the microscopic parameters are deduced from elastic properties of material by using a reverse analysis, which could be divided in 3 steps (Fig. B.II.5):

1. Firstly, from a given value of coordination number, the coefficients of fitting functions $\nu_M = f_1(r_m)$ and $E_M = f_2(E_m, r_m)$ are deduced by using Eq. B.II.3 and B.II.4. In this study, the coordination number is in range from 6 to 13.

2. Secondly, the value of r_m is computed from the Poisson's ratio of material (ν_M) by solving Eq. B.II.5. Theoretically, this third order equation could have three solutions. However, in this study, only solution in range from 0 to 1 of this equation is taken into account: $r_m \in \ ]0; 1]$. This condition ensures mainly the uniqueness of solution.

$$a_1 + b_1.r_m + c_1.r_m^2 + d_1.r_m^3 - \nu_M = 0 \qquad \text{(B.II.5)}$$

3. Finally, the value of E_m is computed from the Young's modulus of material (E_M) and the obtained value of r_m from previous step, by solving the following equation:

$$E_m = \frac{E_M}{(a_2 + b_2.r_m + c_2.r_m^2 + d_2.r_m^3)} \qquad \text{(B.II.6)}$$

As explained, the proposed *fitting functions* allow to compute directly elastic microscopic parameters from elastic properties of material. This calibration method will be validated hereafter.

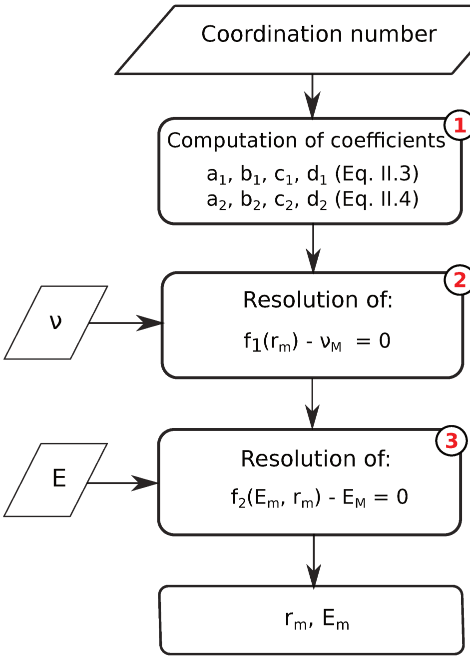

Fig. B.II.5: Main steps of reverse analysis to compute microscopic parameters

B.II.2.3 Validation of calibration formulations

To validate the proposed fitting functions, the behaviors of two typical brittle materials, i.e. soda-lime glass and alumina, were used as reference. These materials, which were used in the research of N. Tessier-Doyen [TD03], will be later investigated to study the thermal damages. The main mechanical properties of reference materials are given in Table B.II.5.

Tab. B.II.5: Mechanical parameters of reference materials

Properties	**Glass**	**Alumina**
Young's modulus E (GPa) *	72	340
Poisson's ratio ν *	0.23	0.24
Tensile strength σ (MPa) **	50	380

* Experimental value taken from [TD03]

** Estimated value taken from [Ber16]

B.II.2.3.a Validation through tensile test simulation

To validate the proposed calibration method, series of tensile test simulations were carried out for the two reference materials. Values of microscopic parameters (r_m, E_m), corresponding to coordination numbers varied from 6 to 13, were computed for the two reference materials by using the proposed fitting functions (Eq. B.II.1, B.II.2, B.II.3, B.II.4). These values were used as microscopic parameters to perform tensile test simulations. The macroscopic Young's modulus and Poisson's ratio *computed* by these numerical tests were then compared to the corresponding values of reference materials (Table B.II.5).

Validation results are summarized in Tables B.II.6 and B.II.7. As expected, the maximal difference between *computed value* and *targeted values* is lower than 2%, which is an acceptable result.

Tab. B.II.6: Validation results through uniaxial tensile test for glass

cn	r_m (-)	E_m (GPa)	Targeted ν (-)	Computed ν_M (-) *	Difference (%)	"Targeted" E (GPa)	Computed E_M (GPa) *	Difference (%)
6	0.506	613.94	0.230	0.231	0.533	72.0	72.26	0.365
7	0.461	613.52	0.230	0.230	0.000	72.0	72.06	0.085
8	0.417	636.18	0.230	0.230	0.000	72.0	71.61	0.538
9	0.380	655.58	0.230	0.230	0.000	72.0	72.44	0.616
10	0.348	677.94	0.230	0.230	0.000	72.0	71.74	0.364
11	0.320	705.07	0.230	0.230	0.000	72.0	71.36	0.884
12	0.298	723.72	0.230	0.230	0.000	72.0	71.00	1.378
13	0.283	725.14	0.230	0.230	0.000	72.0	71.22	1.077

* Average result of the simulations with 4 different samples

Tab. B.II.7: Validation results through uniaxial tensile test for alumina

cn	r_m (-)	E_m (GPa)	Targeted ν (-)	Computed ν_M (-) *	Difference (%)	"Targeted" E (GPa)	Computed E_M (GPa) *	Difference (%)
6	0.478	3378.29	0.240	0.241	0.490	340.0	341.37	0.404
7	0.431	3439.53	0.240	0.240	0.000	340.0	340.29	0.085
8	0.384	3695.23	0.240	0.240	0.000	340.0	337.98	0.593
9	0.338	4058.51	0.240	0.240	0.000	340.0	341.88	0.554
10	0.294	4646.18	0.240	0.241	0.324	340.0	337.70	0.677
11	0.251	5576.21	0.240	0.241	0.353	340.0	335.66	1.276
12	0.215	6820.35	0.240	0.240	0.000	340.0	336.62	0.995
13	0.189	8187.01	0.240	0.239	0.404	340.0	345.80	1.705

* Average result of the simulations with 4 different samples

B.II.2.3.b Validation through hydrostatic compression test simulation

In order to reinforce the validity of the proposed calibration method, it's sensitivity is examined by changing sample shape, sample size, discrete element number and boundary conditions. For this purpose, hydrostatic compression test was used to determine bulk modulus of reference materials. In the proposed configuration of hydrostatic compression test, spherical samples have diameter of *10 mm* and contain around *15,000 discrete elements* (Fig. B.II.6)

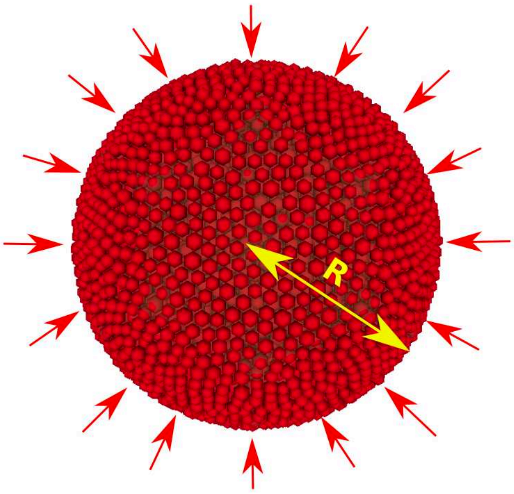

Fig. B.II.6: Configuration of hydrostatic compression test simulation

According to mechanical theory, the bulk elastic properties of a material determines how much it will compress under a given pressure. However, in discrete element framework, the pressure could not be computed in the same way as in the theoretical definition. Thus, in order to simulate an *"equivalent pressure"*, external forces are uniformly imposed to all discrete elements that belong to the surface of the spherical sample. More specifically, the applied forces have the same value, but different directions, which depend on relative position vectors between the center of sample and discrete elements (Fig. B.II.6). Hence, the imposed pressure can be computed as:

$$P = \frac{1}{S}\sum_{j=1}^{N} f_j = \frac{1}{4\Pi R^2}\sum_{j=1}^{N} f_j \tag{B.II.7}$$

where j is an element that belongs to the sample surface, f_j is the value of imposed force on element j, S is the total surface and R is sample radius.

In the DEM simulation, the bulk modulus K of material was computed by dividing the imposed pressure by the fractional volume compression of sample (Eq. B.II.8).

$$K = -\frac{P}{\frac{\Delta V}{V}} \tag{B.II.8}$$

where V is the sample volume, ΔV is the volume change and P is the imposed pressure.

However, according to the elasticity theory, the bulk modulus can be computed through Young's modulus and Poisson's ratio as:

$$K = \frac{E}{3(1-2\nu)} \tag{B.II.9}$$

Hereafter, the results of DEM simulations is confronted with elasticity theory. On the one hand, theoretical bulk modulus values of glass and alumina were computed by using Eq. B.II.9 and Table B.II.5. Thus, the theoretical bulk properties of glass and alumina are 44.4 GPa and 218.0 GPa, respectively. On the other hand, values of macroscopic bulk modulus K_M were measured through DEM simulations, using Eq. B.II.7 and B.II.8. These numerical results are then compared to the theoretical values.

Series of hydrostatic compression tests were performed in order to validate the proposed micro-to-macro relationships. More specifically, value of microscopic parameters, computed by using the proposed fitting function, were used as input parameters of DEM simulations (Tab. B.II.6, B.II.7). As expected, validation results (Table B.II.8 and B.II.9) show that difference between numerical and theoretical values of bulk modulus are lower than 2% for the two reference materials. Consequently, the proposed micro-to-macro relationship, related to elastic behavior, can be validated through hydrostatic compression test.

Tab. B.II.8: Validation results through hydrostatic compression test for glass

cn	r_m (-)	E_m (GPa)	Targeted K (GPa)	Computed K_M (GPa) *	Difference (%)
6	0.506	613.94	44.4	44.319	-0.282
7	0.461	613.52	44.4	44.555	0.249
8	0.417	636.18	44.4	44.428	-0.036
9	0.380	655.58	44.4	44.564	0.269
10	0.348	677.94	44.4	44.566	0.274
11	0.320	705.07	44.4	44.320	-0.280
12	0.298	723.72	44.4	44.201	-0.548
13	0.283	725.14	44.4	44.307	-0.310

* Average result of the simulations with 4 different samples

B.II.2.4 Partial conclusions

Up to now, the calibration of microscopic parameter is still a major challenge for DEM research. In the literature, there is a lack of research that is dedicated to this problematic, especially in continuous media modeling. In this section, the *elastic*

Tab. B.II.9: **Validation results through hydrostatic compression test for alumina**

cn	r_m (-)	E_m (GPa)	Targeted K (GPa)	Computed K_M (GPa) *	Difference (%)
6	0.478	3378.29	218.0	215.312	-1.210
7	0.431	3439.53	218.0	216.325	-0.745
8	0.384	3695.23	218.0	215.526	-1.112
9	0.338	4058.51	218.0	216.146	-0.827
10	0.294	4646.18	218.0	216.054	-0.869
11	0.251	5576.21	218.0	214.793	-1.448
12	0.215	6820.35	218.0	215.718	-1.024
13	0.189	8187.01	218.0	221.124	1.457

micro-to-macro relationships were proposed to be described by *fitting functions*. These mathematical functions were deduced from the data resulting from *1,600* simulations by using the *nonlinear regression* technique. One tensile test simulation lasts around 2 hour, therefore, the data generation process took around 15 days (360 hours) by using the computation server that could run simultaneously 8 simulations. The proposed fitting functions were then examined through uniaxial tensile tests and hydrostatic compression tests. Indeed, the proposed calibration method remained accurate with different configurations of simulation, i.e. loading, sample shape/size, discrete element numbers. Consequently, the proposed calibration method allows to compute precisely the elastic microscopic parameters, regardless of type of numerical experiment, discrete elements number and geometrical properties of sample. The direct calibration method of microscopic fracture threshold will be proposed in the next section.

B.II.3 Direct calibration of microscopic fracture threshold

B.II.3.1 Tensile test simulation: database to determine fitting function

In this section, relationships between macroscopic tensile strength σ_M and microscopic parameters are studied. In addition to the microscopic elastic parameters, the microscopic fracture threshold σ_m was considered in this analysis. Following the same method used in Sect. B.II.2, series of tensile test simulations with different values of (E_m, r_m, σ_m and cn) were carried out in order to determine micro-to-macro relationships which involve the *microscopic fracture parameter*. The total number of simulations is $4 \times 4 \times 5 \times 10 \times 8 = 6,400$ for this parametric study (Table B.II.10). Due to a high number of simulations, the data generation was carried out on a new computational server of IRCER laboratory, which could run simultaneously 32 simulations. The data generation time was then reduced from 60 days to 15 days for this parametric study.

Tab. B.II.10: Value of microscopic parameters

	Values	**Tot. number**
Sample	1 2 3 4	4
E_m (GPa)	500 1000 1500 2000	4
r_m (-)	0.2 0.4 0.6 0.8 1.0	5
σ_m (MPa)	2 4 6 8 50 100 300 500 700 1000	10
cn (-)	6 7 8 9 10 11 12 13	8

The main steps to determine the *fitting functions* that describe the *fracture* micro-to-macro relationships are synthesized in Fig. B.II.7.

Theoretically, the macroscopic fracture tensile strength σ_M depends on 4 microscopic parameters: r_m, E_m σ_m and cn. However, after a first analysis, it was observed that σ_M is proportional to σ_m. Moreover, the ratio between σ_M and σ_m does not depend on microscopic Young's modulus E_m. Therefore, a fitting function of this ratio versus r_m and cn is expected: $\frac{\sigma_M}{\sigma_m} = f_3(r_m, cn)$. The number of variables was reduced from 4 to 2. Consequently, this approach made the regression more simple. The determination of analytical expressions contains two tasks:

- Selection of a type of analytical expression in order to fit the data;
- Refinement of the involved coefficients within the analytical expressions thanks to nonlinear regression.

After the selection of the most relevant analytical expression and nonlinear regression, the obtained fitting function was verified by simulations of common destructive tests, i.e. Brazilian tests and torsion tests.

B.II.3.2 Fracture micro-to-macro relationships

B.II.3.2.a Selection of fitting function

The selection of fitting function that describe the fracture micro-to-macro relationship must satisfy the following criteria:

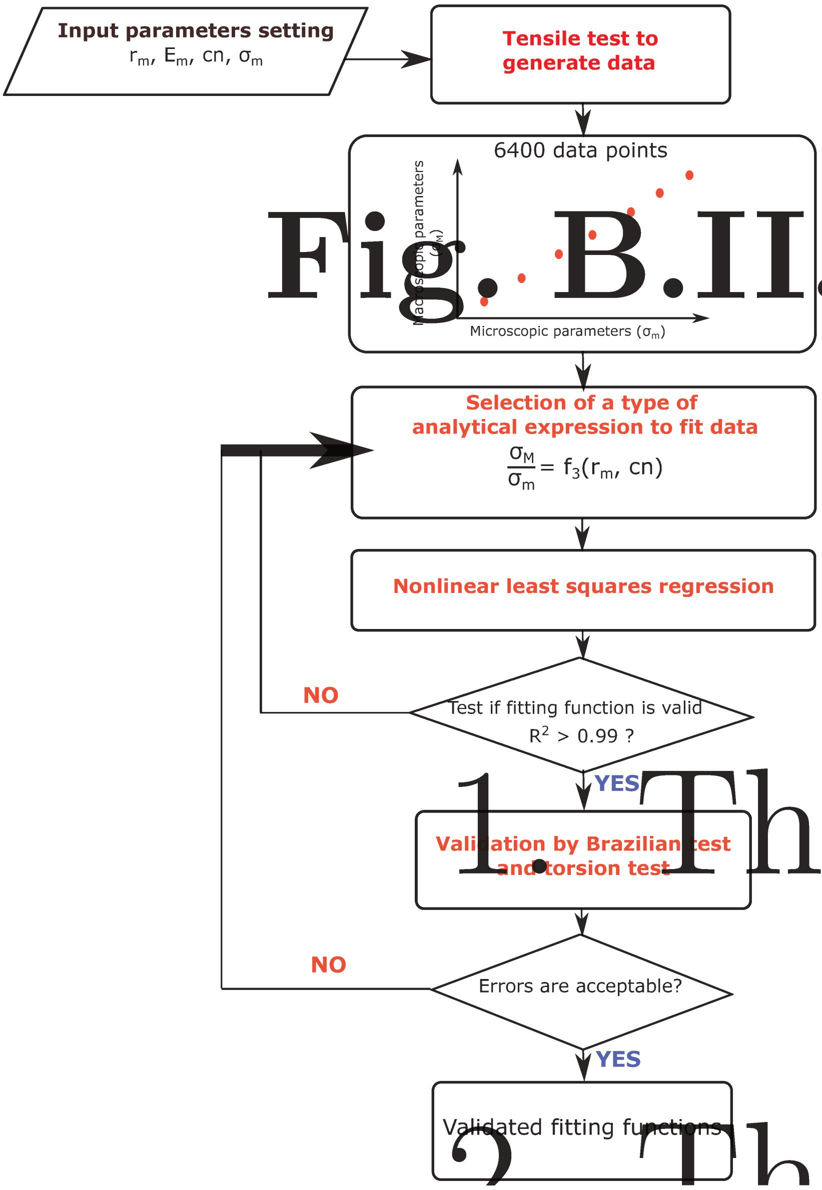

Fig. B.II.7: Ma

1. The coef

2. The diff

B.II.3.2.b Data analyses and nonlinear least squares regression

As with elastic parameters (Sect. B.II.2), the nonlinear least square method was used to determine the *fracture* micro-to-macro relationship of the proposed discrete element model. After initial analyses, as illustrated on Fig. B.II.8(a), it is noticed that if values of E_m, r_m, σ_m and cn are fixed, σ_M is proportional to σ_m:

$$\sigma_M = k \times \sigma_m \tag{B.II.10}$$

In addition, Fig. B.II.8(b) reveals that the coefficient of proportionality k (Eq. B.II.10) does not depend on value of microscopic Young's modulus E_m.

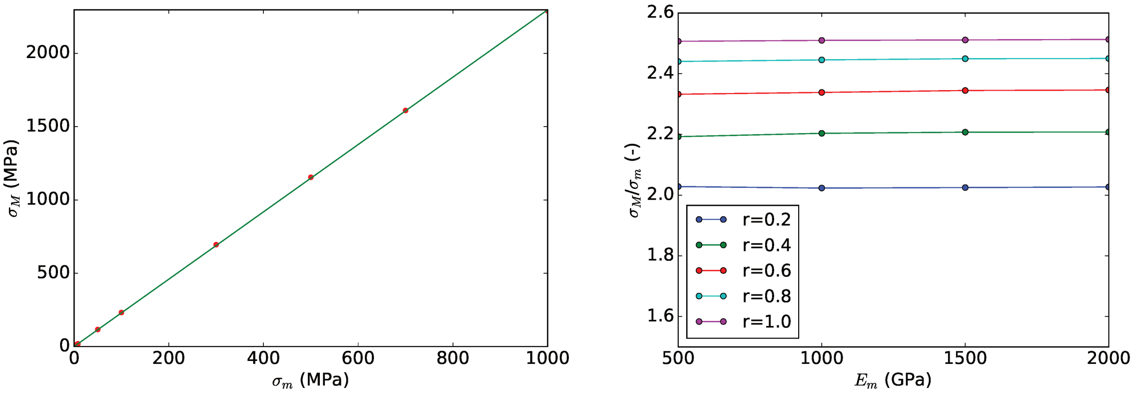

(a) Evolution of σ_M versus σ_m when E_m, r_m and cn are fixed

(b) Evoluation of k versus E_m(case c_n=10)

Fig. B.II.8: Evolution of σ_M versus microscopic parameters

Based on theses results, a fitting function $k = f_3(r_m, cn)$ is expected. After examining many functions, it was found that the relation $k = f_3(r_m, cn)$ could be well described by the following relation:

$$\begin{aligned} k = f_3(r_m, cn) =& [(m_0 + n_0 \cdot cn + p_0 \cdot cn^2) + r_m \cdot (m_1 + n_1 \cdot cn + p_1 \cdot cn^2 + q_1 \cdot cn^3) \\ & + r_m^2 \cdot (m_2 + n_2 \cdot cn + p_2 \cdot cn^2)] \end{aligned} \tag{B.II.11}$$

The coefficients of Eq. B.II.11 were refined by using the nonlinear least square regression (Tab B.II.11).

Fig. B.II.9 reveals that the obtained fitted surface is in good accordance with data points. Indeed, the nonlinear regression has a good coefficient of determination ($R^2 \approx 1$). Consequently, Eq. B.II.11 was chosen to describe the

Tab. B.II.11: Refinement of fitting function related to microscopic fracture threshold

m_0	n_0	p_0	
-0.66972	0.30934	-0.00618	
m_1	n_1	p_1	q_1
-2.83372	1.25549	-0.11087	0.00254
m_2	n_2	p_2	
1.54739	-0.46791	0.02653	

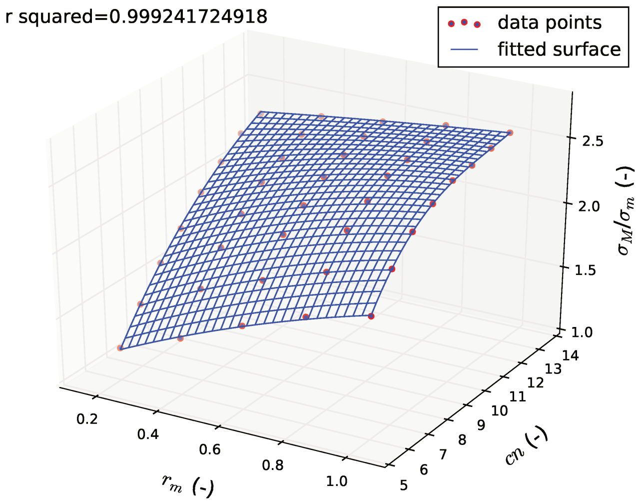

Fig. B.II.9: Fitting results of function $k = f_3(r_m, cn)$

fracture micro-to-macro relationship of CBM.

B.II.3.2.c Deduction of microscopic fracture threshold from tensile strength of material - Reverse analysis

In this study, the fitting functions were determined to describe the *micro-to-macro* relationships of CBM. As explained in paragraph B.II.2.2.c, this approach enables the computation of microscopic parameters from mechanical properties of material by using reverse analysis, which could be divided in 2 main steps (Fig. B.II.10):

1. Firstly, the value of k is computed from value of r_m and cn (Eq. B.II.11). In this step, the value of r_m and cn are taken from previous analysis in paragraph B.II.2.2.c.

2. Then, the value of microscopic fracture threshold σ_m could be computed by:

$$\sigma_m = \frac{\sigma_M}{k} \qquad \text{(B.II.12)}$$

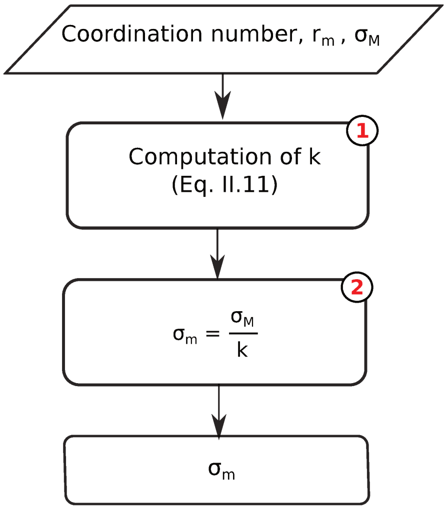

Fig. B.II.10: Main steps of reverse analysis to compute microscopic fracture threshold

As explained, the proposed calibration method allows to compute directly the microscopic fracture threshold of CBM from tensile strength of material. The fitting function related to microscopic fracture threshold σ_m will be validated hereafter, through Brazilian tests and torsion tests.

B.II.3.3 Validation of calibration formulation

B.II.3.3.a Validation through Brazilian test simulation

To validate the proposed relationships between macroscopic tensile strength σ_M and microscopic parameters, series of Brazilian test simulations were carried out. Brazilian tests are commonly used for characterization of brittle materials such as ceramic, concrete, refractory. In experimental techniques, Brazilian tests are performed by applying a vertical compressive load across the diameter of a disk sample. In the rupture phase, a crack appears along the vertical diameter of the disk, due to tensile stresses induced horizontally by the geometry of sample [BDP+17].

Again, validation process is given for glass and alumina materials. For each value of coordination number, the corresponding value of r_m obtained in the previous section (Table B.II.6 and B.II.7) was used to compute microscopic fracture threshold σ_m value by using the Equation B.II.11. This value of σ_m was used to perform Brazilian test simulations. In the proposed configuration, the virtual disk samples have *diameter of 50 mm, thickness of 10 mm* and contain around *20,000* *discrete elements.* According to experimental and numerical studies in literature, crack initiation at the center of the disk sample is considered to be crucial for the test validity [WJK+04, Fai64, EW12]. C. Fairhurst, in [Fai64], stated that " *failure may occur away from the center of the disk for small angles of loading contact area with material of low compression tension ratios. In such cases, the tensile strength as usually calculated from test results, is lower than the true value*". Conforming to this observation, opposite vertical displacements are imposed on two circular arcs of 2α=24° of virtual sample (Fig. B.II.11).

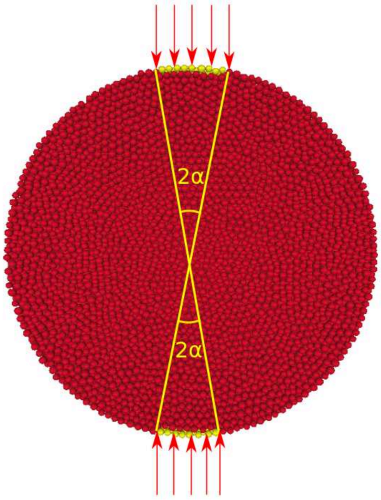

Fig. B.II.11: Configuration of the virtual Brazilian test

Vertical forces at upper and lower loading area, P_{up} and P_{down} respectively, resulting from the imposed displacement are measured during simulations. Hence, the average applied force P is computed as:

$$P = \frac{|P_{\text{up}}|+|P_{\text{down}}|}{2} \tag{B.II.13}$$

According to literature [WJK+04], the tensile strength can be computed as:

$$\sigma_M = \frac{2 \cdot P_c}{\pi \cdot t \cdot D} \tag{B.II.14}$$

where P_c is the critical load (it is also the maximum applied load during the test), t and D are the disk thickness and diameter, respectively.

The typical behaviours resulting from the Brazilian test simulation are reported in Fig. B.II.12, B.II.13, and B.II.14. In Fig. B.II.12, a sudden decreasing of the average force P indicates the failure of the virtual sample. The corresponding value of P is considered as the critical load in order to compute the macroscopic tensile strength σ_M of the sample by using Equation B.II.14. Fig. B.II.13 shows that the crack is initiated near the center of the disk and propagate along vertical diameter, as expected. Consequently, the crack initiation and propagation are relevant with theoretical predictions and experimental observations [EW12].

In order to highlight the interest of the virial stress computation, as described in section B.I.5, the evolution of stress along the diameter is monitored. Fig. B.II.14 shows both the theoretical horizontal stress evolution and the numerical one. This comparison was performed before the failure of sample, when the applied force $P \approx 36.48$ kN (Fig. B.II.12). The theoretical stress distribution on the loading diameter is given by the following relationship [Hon59] [SAKK07]:

$$\sigma = \frac{2p}{\pi} \left\{ \frac{\sin 2\alpha}{1 - 2\rho^2 \cos 2\alpha + \rho^4} \left[1 - \rho^2 \right] - \arctan \left[\frac{\rho^2 \sin 2\alpha}{1 - \rho^2 \cos 2\alpha} \right] - \alpha \right\} \tag{B.II.15}$$

where :

- σ is the horizontal normal stress,
- p is the load per unit area,
- t is the disk thickness,
- R is the disk radius of the disk,
- r is distance from a point in disk to the center,
- ρ is equal to r/R and
- α is the half central angle of the applied distributed load.

Please notice that, in Fig. B.II.14, the numerical blue curve is given thanks to the Gaussian Kernel interpolation method available in the *Paraview* software. This figure reveals a good quantitative accordance between theoretical curve (continuous dotted curve) and numerical curve, although there are discrepancies towards the loading areas. The possible reason for these discrepancies may come from the edge effect that influence the virial stress computation at the boundaries. In fact, at the boundaries of domain, discrete elements are cut by domain boundaries, then their coordination numbers are one half of the coordination numbers of the internal elements. This could raise errors in the computation.

Based on the typical behaviors resulting from the Brazilian test simulation, it is noticed that the proposed fracture criterion (section B.I.5) and the virial stress computation seem to be able to simulate fracture phenomena of brittle materials under complex loadings, i.e. (indirect) tensile test.

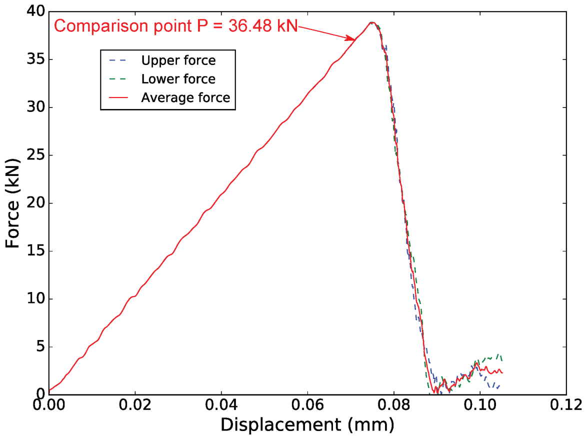

Fig. B.II.12: Force - displacement curve during Brazilian test, case cn =10, glass

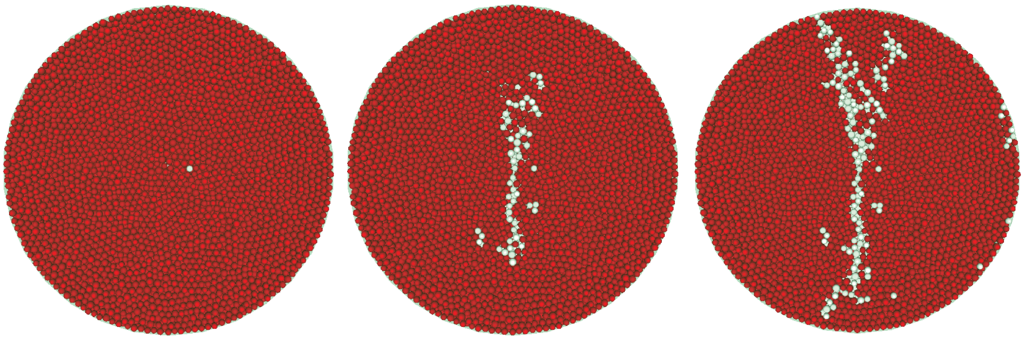

Fig. B.II.13: Crack propagation of Brazilian test

The macroscopic tensile strength σ_M obtained by Brazilian tests were compared to the theoretical values of the tensile strength of glass and alumina (50 MPa and 380 MPa, respectively, Table B.II.5). Synthesis of the validation through Brazil test simulation is shown in the Table B.II.12 and B.II.13. Quantitatively, differences are quite acceptable for two reference materials. Consequently, the proposed relationships between σ_M and microscopic parameters of DEM could be validated through Brazilian test simulation.

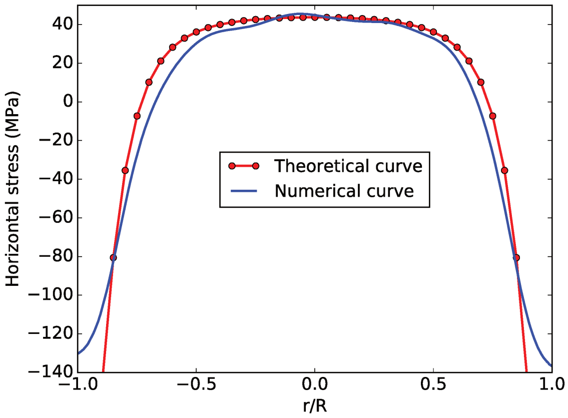

Fig. B.II.14: Horizontal stress distribution along vertical diameter of sample, case *cn* = 10, glass, when applied force P = 36.48 kN (see Fig. B.II.12)

Tab. B.II.12: Validation of brittle behavior calibration for glass

cn	r_m	σ_m (MPa)	Targeted σ (MPa)	Computed σ_M (MPa) *	Difference (%)
6	0.506	78.08	50.0	50.94	1.88
7	0.461	70.58	50.0	49.59	1.80
8	0.417	65.79	50.0	49.13	1.74
9	0.380	62.43	50.0	49.74	2.20
10	0.348	60.08	50.0	50.27	2.05
11	0.320	58.44	50.0	52.08	4.16
12	0.298	57.37	50.0	53.08	6.15
13	0.283	56.80	50.0	53.49	6.99

* Average result of the simulations with 4 different samples

Tab. B.II.13: Validation of brittle behavior calibration for alumina

cn	r_m	σ_m (MPa)	Targeted σ (MPa)	Computed σ_M (MPa) *	Difference (%)
6	0.478	601.22	380.0	377.30	0.97
7	0.431	543.05	380.0	363.01	4.47
8	0.384	505.90	380.0	359.54	5.38
9	0.338	480.10	380.0	369.24	2.83
10	0.294	461.84	380.0	368.16	3.12
11	0.251	448.82	380.0	385.09	2.00
12	0.215	439.89	380.0	396.17	4.26
13	0.189	435.00	380.0	406.88	7.08

* Average result of the simulations with 4 different samples

B.II.3.3.b Validation through torsion test simulation

In this section, the proposed calibration method is applied for brittle torsion test simulation. Fig. B.II.15 presents the geometric model used to simulate the quasi-static torsion test. The virtual cylindrical samples have diameter of *4 mm*, length of *100 mm* and contain around *10,000 discrete elements*. The samples are subjected to progressive rotations ϕ_x and $-\phi_x$ about the $\mathbf{X}$ axis on the *xMin* and *xMax* opposite faces. The coordination number is arbitrary set at 10 and the corresponding values of microscopic parameters (i.e. r_m, E_m and σ_m, Tab. B.II.12, B.II.13) are used to perform simulations of both reference materials.

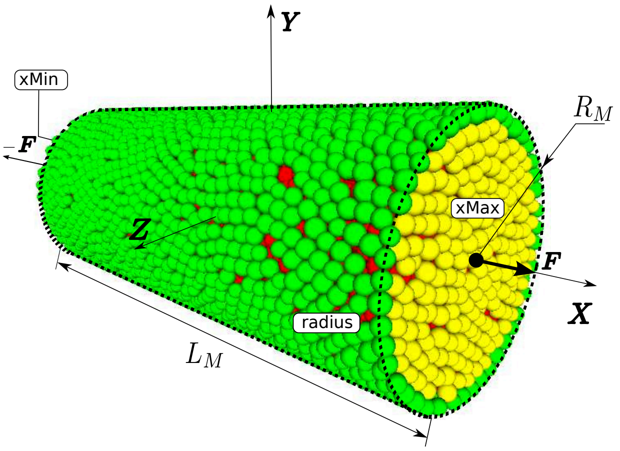

Fig. B.II.15: Discrete domain for torsion tests

To compute the macroscopic fracture stress, the forces $\mathbf{F_p}$ and torques $\mathbf{M_p}$ applied on opposite faces are monitored. The macroscopic torsion torque M_{Mx} can be obtained from these quantities as follows:

$$M_{Mx}^{xMin} = \sum_{p=1}^{N_{xMin}} \left(\mathbf{M_p} + \mathbf{O_1G_p} \wedge \mathbf{F_p}\right).\mathbf{X} \qquad \text{(B.II.16)}$$

$$M_{Mx}^{xMax} = \sum_{p=1}^{N_{xMax}} \left(\mathbf{M_p} + \mathbf{O_2G_p} \wedge \mathbf{F_p}\right).\mathbf{X} \qquad \text{(B.II.17)}$$

where the points O_1 and O_2 are the centers of *xMin* and *xMax* faces and G_P is the center of a discrete element p. Then, the macroscopic torsion torque M_{Mx} is taken as the mean of M_{Mx}^{xMin} and M_{Mx}^{xMax}. Based on the material strength theory, the maximal macroscopic shear stress can be obtained as:

$$\tau_{M_{max}} = \frac{M_{Mx}}{Io} R_M \qquad \text{(B.II.18)}$$

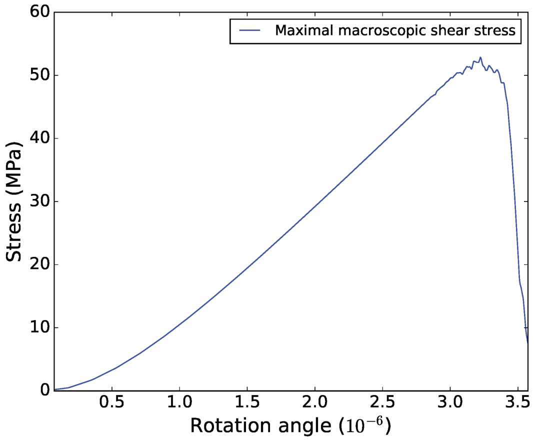

Fig. B.II.16: Shear stress curve during torsion test for glass

where R_M is the radius of the discrete domain and Io is the polar moment of inertia which is defined as:

$$Io = \frac{\pi\, R_M^4}{2} \tag{B.II.19}$$

Using the Rankine criterion, the macroscopic tensile strength which is the maximal macroscopic principal stress can be expressed as:

$$\sigma_M = (\tau_{M_{max}})_{fracture} \tag{B.II.20}$$

where $(\tau_{M_{max}})_{fracture}$ is the maximal macroscopic shear stress measured at the fracture of the numerical sample. The values of macroscopic tensile strength measured through torsion test simulations are compared with targeted values of tensile strength for 2 reference materials.

A typical behavior resulting from torsion test is reported in Fig. B.II.16 and B.II.17. As illustrated in B.II.16, a sudden decreasing of maximal macroscopic shear stress indicates the failure of samples. In addition, at the structure scale, the crack geometry seems in agreement with the brittle fracture theory that predicts an helical crack surface oriented at 45° to the main axis of the numerical sample (Fig. B.II.17). Moreover, the quantitative simulation results, summarized in Tab. B.II.14, show that difference between computed values of σ_M and targeted values are quite acceptable for two materials. Consequently, the proposed micro-to-macro relationships seemed to be compatible to describe brittle failure in shear experiments.

Tab. B.II.14: Torsion simulation results

	r_m	σ_m (MPa)	Targeted σ (MPa)	Computed σ_M (MPa) *	Difference (%)
Glass	0.348	60.08	50	53.04	6
Alumina	0.294	461.84	380	394.23	3.69

* Average result of the simulations with 4 different samples

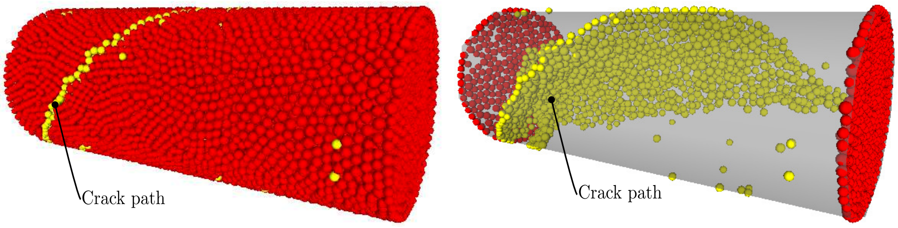

(a) View showing all discrete elements (b) View showing only critical elements

Fig. B.II.17: View of crack path in a torsional test; the discrete elements in which the fracture criterion is fulfilled are highlighted

B.II.3.4 Partial conclusions

In this study, the *fracture* macro-to-micro analysis were validated through Brazilian tests and torsion tests. As expected, the proposed fitting function allows to compute accurately the microscopic fracture threshold to reach the tensile strength of reference materials. Combining with the elastic macro-to-micro analysis (Sect. B.II.2), this methodology enables a direct deduction of microscopic parameters of CBM from mechanical properties of elastic brittle material, which is described by Poisson's ratio, Young's modulus and tensile strength. This calibration method ensures also an unique solution of microscopic parameters to match the expected macroscopic behaviors. Moreover, the virial stress concept seemed to be able to describe the crack phenomena, in terms of crack position and crack path, in comparison with experimental observations. These results were published in the *Computational Particle Mechanics* international journal [NAH19]. Hereafter, the virial stress concept will be further examined through its application to the modeling of residual stresses induced by thermal expansion mismatch.

B.II.4 Application to the modeling of thermal stresses in elementary composite material

B.II.4.1 Introduction

This section deals with the modeling of thermal stress due to thermal expansion mismatch within composite materials. Indeed, simulations of cooling stage of different composite-like materials were performed by using DEM and FEM approaches. In these preliminary simulations, the single-particle configuration was used for its simplicity. The stress field obtained with DEM was then confronted with FEM results and theoretical predictions to verify accuracy of the virial stress computation. In this study, two cases of thermal expansion mismatch are studied:

- thermal expansion coefficient of matrix is higher than inclusion: $\Delta\alpha > 0$
- thermal expansion coefficient of matrix is lower than inclusion: $\Delta\alpha < 0$.

The purpose is to confront the developed stress computation of DEM with FEM and theoretical approaches, which has been well developed in the literature. In the present study, the model materials used by Tessier-Doyen [TD03], which exhibit the considered cases of thermal expansion mismatch, were used as reference materials, i.e. Cofer glass-alumina and BA glass-alumina composites (Section A.I.3). Hereafter, Cofer glass - alumina and BA glass - alumina composites are called material 1 and material 2, respectively. The experimental values of thermo mechanical properties of the components of reference materials are synthesized in Tab. B.II.15

Tab. B.II.15: Thermo-mechanical properties of reference composite materials [TD03]

Properties	Cofer glass matrix	BA glass matrix	Inclusion
Young's modulus E (GPa)	72	68	340
Poisson's ratio ν (-)	0.23	0.20	0.24
Tensile strength σ (MPa)	60	86	300*
Coef. of thermal expansion α ($°K^{-1}$)	11.6e-6	4.6e-6	7.6e-6
Glass transition temperature (°C)	455-475	575-595	-

* Value from literature

In first step, the elastic behavior was investigated and damages were not modeled. Hence, in these first simulations, the decrease of temperature was set at 120°C in order to generate thermal residual stresses without any damage.

In second step, the damages due to thermal expansion mismatch during cooling were modeled by using DEM approach. In these simulations, in order to generate the thermal damages, the reference materials were subjected to a critical decrease of temperature, from the vitreous transition temperature of glass matrices (T_g) to ambient temperature (20°C). Indeed, reference materials exhibit a visco-elasto-plastic behavior when the temperature is greater than T_g. However, since this study focused only on solid behaviors, temperatures higher than T_g were not considered.

In the research of Tessier-Doyen [TD03], the transition temperature of glasses, determined by *dilatometry experiments*, corresponded to an interval of temperature (Tab. B.II.15). In the present study, the starting point of cooling simulation was tested with both maximal and minimum value of transition temperature. However, the minimum value seemed to give more relevant results in comparison with experimental ones. Consequently, only the results associated to the minimum value of T_g will be discussed in this section. The starting points of cooling simulations were 455 and 555°C for material 1 and material 2, respectively. The resulting damages were then compared to the experimental observations in order to examine the adaptability of the proposed DEM model to study the thermal damage phenomena.

B.II.4.2 Modeling configuration: single-inclusion composite

B.II.4.2.a Discrete element modeling

In this study, the numerical results will be compared with theoretical predictions of thermal stresses. In the compared theoretical prediction, the configuration of a spherical inclusion embedded in an isotropic infinite matrix was used [LSB00]. However, the boundary condition that is usually used in FEM approach to describe the assumption of infinite media, e.g. periodic boundary condition, has not yet been available in the developed DEM. Therefore, in the performed numerical simulations, the concept of Representative Elementary Volume (REV) was used. More specifically, a cubic sample with a spherical inclusion embedded inside was modeled. The length of edges of the cubic sample and the radius of the inclusion were set to be equal to 2.2 mm and 0.275 mm, respectively (Fig. B.II.18) These specific dimensions ensured the accuracy of simulations with a reasonable time cost. Indeed, it was a compromise between number of discrete elements

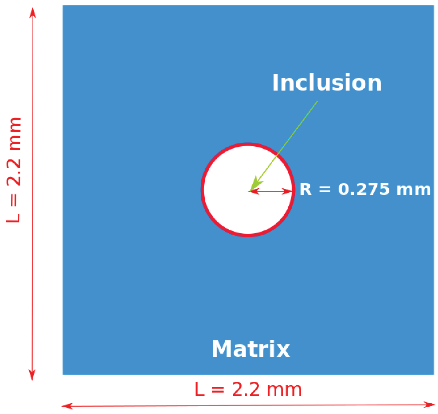

Fig. B.II.18: Median cross section of 3D sample

of sample and number of discrete elements associated to the inclusion, in order to model precisely the thermal stresses. Regarding the boundary conditions, in DEM simulations, 6 surfaces of cubic samples are free to have displacement under loading. In the performed DEM simulations, cubic discrete domains composed of 80,000 discrete elements were generated to study the considered phenomena. The coordination number was arbitrary set to 10. An user-defined *macro-command* was implemented in order to generate the spherical inclusion inside the cubic discrete domain. More precisely, if the distance between a discrete element and the center of sample does not exceed the radius of inclusion, i.e. 0.275 mm, it will be assigned to the inclusion. By contrast, the remaining discrete elements are assigned to the matrix (Fig. B.II.19). Thus, the number of discrete elements that belong to the inclusion was about 750. The microscopic parameters was then computed for each components of reference materials by using the direct calibration method proposed in Sect. B.II.2 and Sect. B.II.3. The values of microscopic parameters used to perform DEM simulation are synthesized in Tab. B.II.16.

Tab. B.II.16: Input parameters used to model reference materials

Input parameters	Cofer glass matrix	BA glass matrix	Inclusion
Young's modulus E_m (GPa)	677.94	290.31	4646.14
Radius ratio ν_m (-)	0.35	0.49	0.29
Fracture threshold σ_m (MPa)	22.98	37.80	∞
Coef. of thermal expansion α (K^{-1})	11.6e-6	4.6e-6	7.6e-6

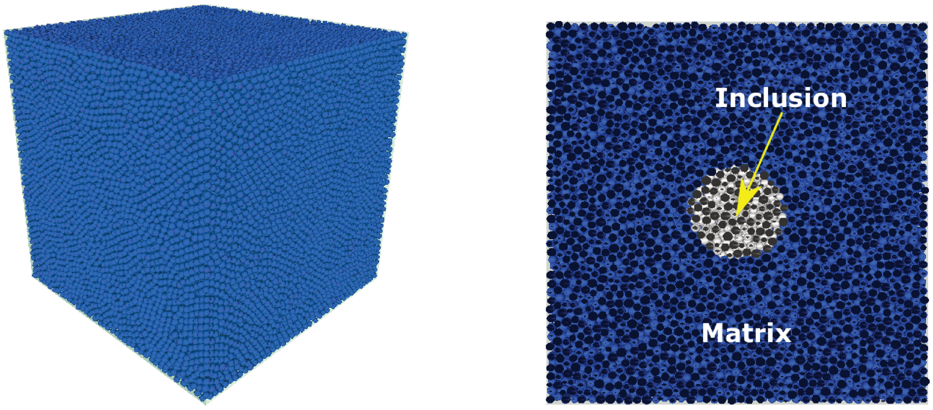

(a) 3D view of the cubic discrete sample

(b) Cross-section of the cubic discrete sample

Fig. B.II.19: Discrete element sample (visualization in *granoo-viewer*)

B.II.4.2.b Finite element modeling

In this study, the FEM simulations were performed by using *Code Aster* software[1], developed by EDF (Électricité de France). The mesh was generated by using *Netgen* algorithm [Sch97]. The maximum and minimum linear dimensions of mesh cells were 0.1 mm and 0.02 mm, respectively. Hence, the mesh is composed of 50, 792 nodes and 288, 055 elements (Fig. B.II.20).

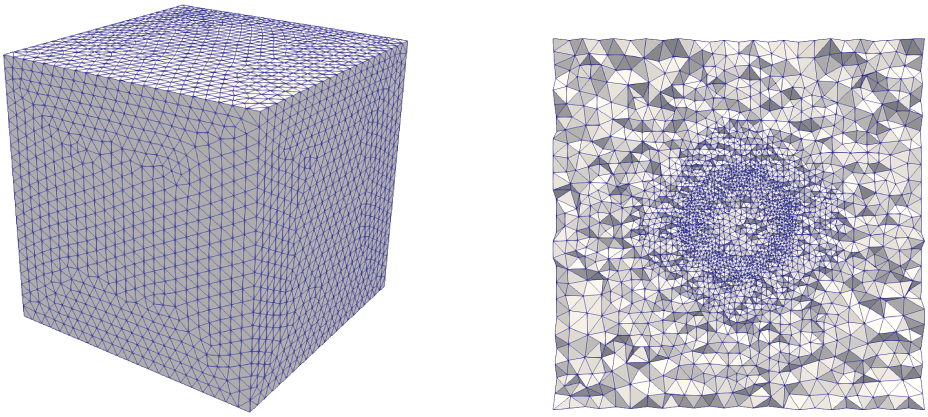

(a) 3D view of the mesh

(b) Median cross-section of mesh

Fig. B.II.20: Mesh discretization of sample generated by using Netgen algorithm in Code Aster

The same boundary conditions used in DEM simulations were applied here: the

---

[1] www.code-aster.org

surfaces of FEM samples were free to shrink during cooling stage. As illustrated in Fig. B.II.21, the displacements at the centers of 3 surfaces of sample are clamped along the direction of sample edges. These boundary conditions prevent the movements of rigid bodies, which are forbidden in static FEM simulations.

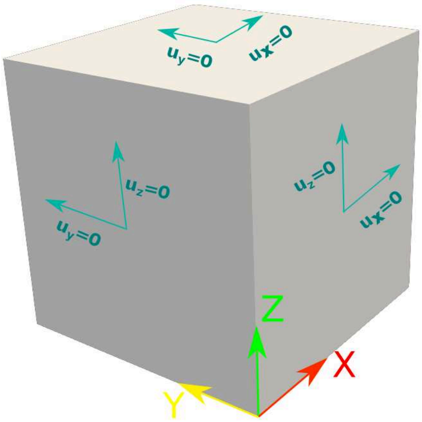

Fig. B.II.21: Boundary conditions of FEM simulation

The thermo mechanical properties of references materials were then used to performed simulations (Tab. B.II.15).

B.II.4.3 DEM-FEM confrontation: validation of virial-stress-based modeling

B.II.4.3.a Principles of DEM-FEM comparison

In this study, the modeling of thermal stress was performed for the two reference materials. Firstly, the comparison of stress fields on the vertical median cross section of the sample were carried out (Fig. B.II.22(a)). Secondly, the comparison was further investigated by evaluating the thermal stress profile within the horizontal median line of the considered cross section (Fig. B.II.22(b)).

As it was shown previously, the discretization methods used in DEM and FEM are different (figures B.II.19(b) and B.II.20(b)). Therefore, the stress values obtained by DEM and FEM needed to be extracted in a common grid/line in order to perform quantitative comparisons. More specifically, the stress values on the median cross section were extracted by using the *Gaussian kernel interpolation* tool in *Paraview* software. The first analyses showed that the shear stress components were negligible in comparison with normal stress components. Hence, the present comparison focused only on the normal stress components, i.e. σ_{xx}, σ_{yy} and σ_{zz}.

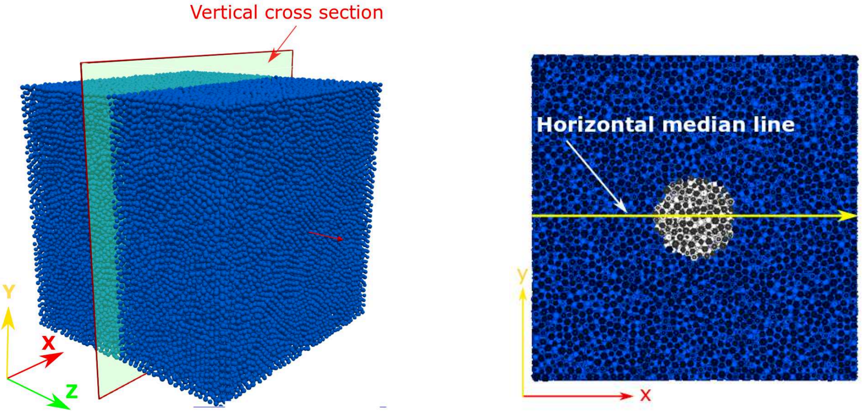

(a) Vertical median cross section (b) Horizontal median line

Fig. B.II.22: Investigated zone of stress field comparison

Moreover, in order to decrease the effect of the random filling process of sample construction (Sect. B.I.3), the DEM results was obtained by averaging the results of 5 different discrete samples. In summary, the DEM-FEM comparison were accomplished in 3 steps (Fig. B.II.23):

1. Gaussian kernel interpolation of DEM results of 5 discrete samples on a common grid for the vertical median cross section. This enables the computation of average results of 5 samples which have different spatial distributions of discrete elements. In this study, the grid has configuration of 500 × 500 points. Thus, the average DEM results could be easily computed on this common grid;

2. Gaussian kernel interpolation of FEM results on the same grid that was used for averaging DEM results;

3. Computation of difference between DEM and FEM results in the common grid

In a further step, the numerical results were confronted with theoretical predictions to examine the accuracy of performed simulations. In this section, the theoretical prediction of thermal stress proposed by Lauke et al. [LSB00] is used (equations B.II.21 and B.II.22).

$$\sigma^p_{rad} = \frac{12 G_m K_p \left(\alpha_m - \alpha_p\right) \Delta T}{4G_m + 3K_p}, \qquad \sigma^p_{orth} = \sigma^p_{rad} \tag{B.II.21}$$

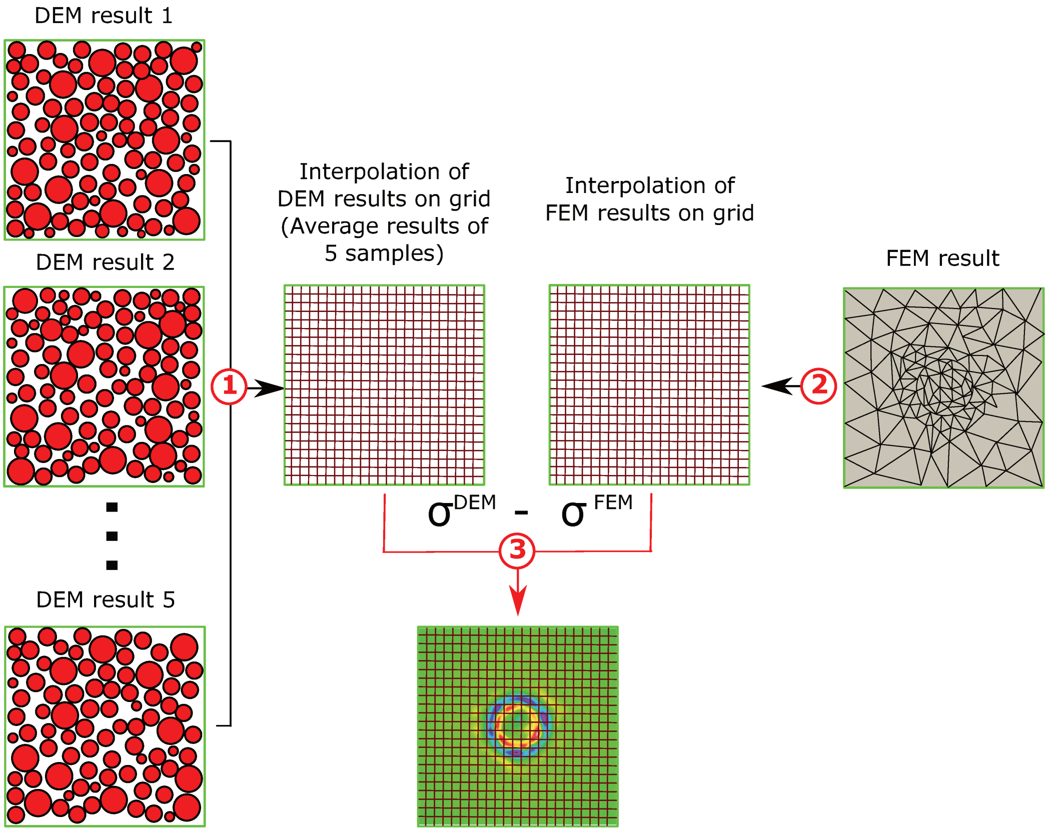

Fig. B.II.23: Main steps of quantitative DEM-FEM comparison

$$\sigma_{rad}^{m} = \frac{r_p}{r}\frac{12G_m K_p\left(\alpha_m - \alpha_p\right)\Delta T}{4G_m + 3K_p}, \qquad \sigma_{orth}^{m} = -\frac{1}{2}\sigma_{rad}^{m} \tag{B.II.22}$$

where: *(p, m)* superscripts denote particle and matrix respectively; $(rad, orth)$ subscripts denote radial stress component and orthoradial (circumferential) stress component, respectively (Fig. B.II.30); G, K, α denote shear modulus, bulk modulus and coefficient of thermal expansion, respectively; ΔT denotes the temperature difference; r_p is the radius of inclusion, r is the distance between considered point and inclusion center.

According to equations B.II.21 and B.II.22, in the case of $\alpha_m > \alpha_p$ (material 1), the radial stress component and orthoradial stress component in the matrix are respectively compressive and tensile. Whereas, the inclusion of material 1 is under compressive stress. By contrast, in the case of $\alpha_m < \alpha_p$ (material 2), the radial stress component and orthoradial stress component in the matrix are respectively tensile and compressive. Whereas, the inclusion of material 2 is under tensile stress. The thermal stresses of the two reference material are resumed in

Tab. B.II.17.

Tab. B.II.17: Thermal stresses within the matrix due to thermal expansion mismatch

Materials	$\Delta\alpha$	Radial stress	Orthoradial stress
Material 1 (Cofer-alumina)	$\alpha_m > \alpha_p$	Compressive	Tensile
Material 2 (BA-alumina)	$\alpha_m < \alpha_p$	Tensile	Compressive

Logically, the accuracy of stress computation is crucial for the modeling of damage phenomena. However, up to now, the accuracy of virial stress computation in DEM has not usually been investigated. Whereas, the stress computation of FEM and theoretical approaches has been developed for a long time. Therefore, in this study, the DEM was confronted with these approaches in order to verify its adaptability to study the thermal damage phenomena.

B.II.4.3.b Case of cofer-alumina composite

The DEM-FEM comparison of stress field for material 1 are synthesized in Fig. B.II.24, which correspond to the case $\alpha_m > \alpha_p$. In this figure, the first column, i.e. figures B.II.24(a), B.II.24(d) and B.II.24(g), corresponds to DEM results. The second column, i.e. figures B.II.24(b), B.II.24(e) and B.II.24(h), corresponds to FEM results. These first two columns illustrate that, the normal stress components (σ_{xx}, σ_{yy}, σ_{zz}) on the median cross section obtained by DEM and FEM are quite identical. Indeed, the inclusion is under compressive stresses, whereas, the matrix is under both tensile stress and compressive stresses. These observations are compatible with theoretical predictions of thermal stress proposed in [LSB00].

In the third column, i.e. figures B.II.24(c), B.II.24(f) and B.II.24(i), the absolute differences between DEM and FEM results are shown:

$$\text{Absolute difference} = \sigma_{ii}^{DEM} - \sigma_{ii}^{FEM} \quad \text{where ii = xx, yy, zz} \tag{B.II.23}$$

As illustrated, the differences are quite acceptable. Indeed, the DEM-FEM difference in the matrix varied mainly from 2 to 5 MPa. Whereas, the difference in the inclusion varied from 2 to 8 MPa. The highest value of difference, about 8 MPa, were detected in the interfacial zone between matrix and inclusion.

Finally, the confrontation between DEM, FEM and theoretical approaches is shown in Fig. B.II.25. As illustrated, the normal stress profiles (σ_{xx}, σ_{yy}, σ_{zz}) within the median line obtained by FEM, DEM and theoretical approaches (Eq. B.II.21 and B.II.22) show a good accordance. It can also be observed

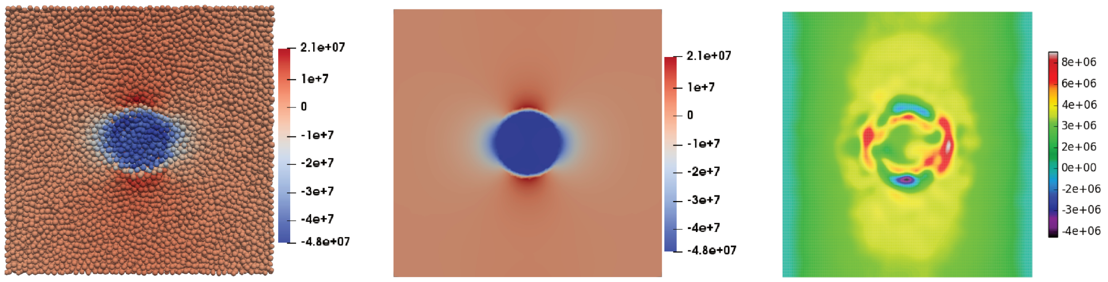

(a) σ_{xx} (DEM) (b) σ_{xx} (FEM) (c) Absolute difference σ_{xx}

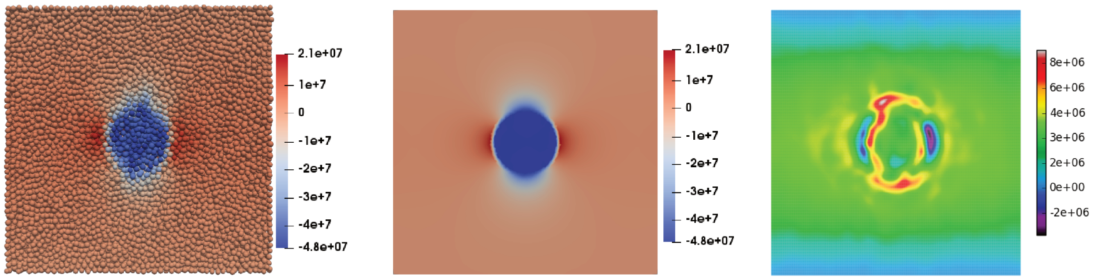

(d) σ_{yy} (DEM) (e) σ_{yy} (FEM) (f) Absolute difference σ_{yy}

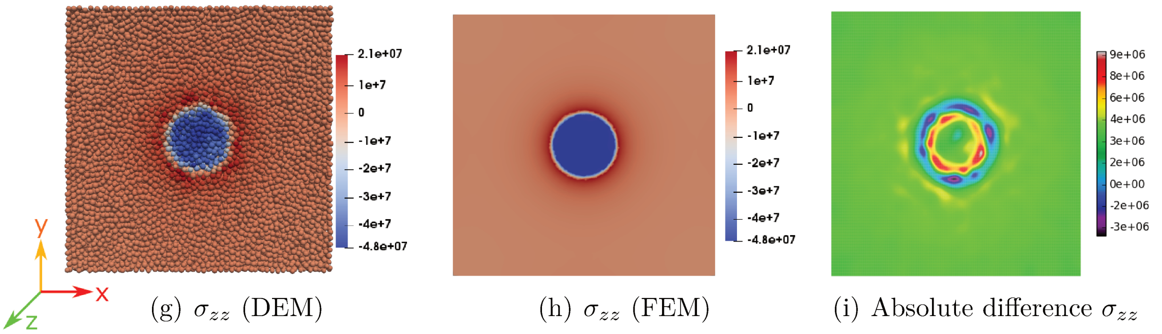

(g) σ_{zz} (DEM) (h) σ_{zz} (FEM) (i) Absolute difference σ_{zz}

Fig. B.II.24: DEM-FEM comparison of thermal stresses on median cross section, case of cofer glass-alumina ($\alpha_m > \alpha_p$), $\Delta T = 120°\text{C}$

that the maximum differences between numerical and theoretical predictions were positioned in the interfacial zone between matrix and inclusion. Despite the observed discrepancies, the comparison results were globally acceptable with regard to the whole cross section.

B.II.4.3.c Case of BA - alumina composite

The DEM-FEM comparison of stress field for material 2 are synthesized in Fig. B.II.26, which correspond to the case $\alpha_m < \alpha_p$. In this figure, the first column, i.e. figures B.II.26(a), B.II.26(d) and B.II.26(g), corresponds to DEM results. The second column, i.e. figures B.II.26(b), B.II.26(e) and B.II.26(h), corresponds to FEM results. These first two columns show that the normal stress components

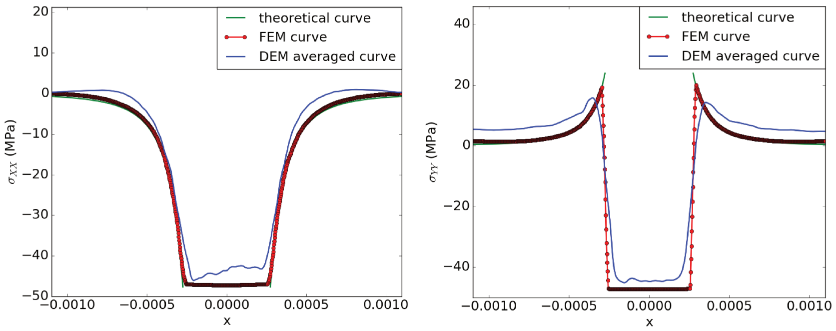

(a) σ_{xx} (b) σ_{yy}

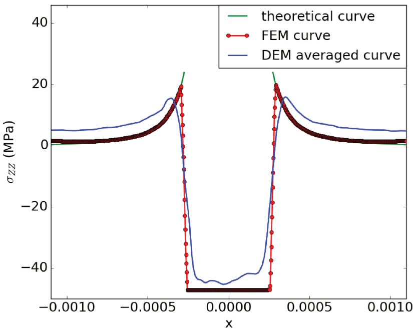

(c) σ_{zz}

Fig. B.II.25: Profile of normal stresses along the median line, case of cofer glass-alumina ($\alpha_m > \alpha_p$), $\Delta T = 120$°C

on the median cross section (σ_{xx}, σ_{yy}, σ_{zz}) obtained by DEM and FEM are quite identical. Indeed, the inclusion is under tensile stress, whereas, the matrix is under both tensile stress and compressive stresses. These observations show a good agreement with theoretical predictions [LSB00].

The third column, i.e. figures B.II.26(c), B.II.26(f) and B.II.26(i), shows absolute difference between DEM and FEM results. The same tendency as in the case of material 1 were observed here. In this case, the absolute difference in the matrix was about -1 MPa. Whereas, the absolute difference in the inclusion varied from 0 to 5 MPa. The highest value of difference were mainly detected in the interfacical zone between inclusion and matrix.

Finally, the confrontation between DEM, FEM and theoretical approaches is shown in Fig. B.II.27. As in the case of material 1, the normal stress profiles within the median line (σ_{xx}, σ_{yy}, σ_{zz}), obtained by three confronted approaches, had similar shape. It can also be observed that the maximum differences between numerical and theoretical predictions were positioned in the interfacial zone

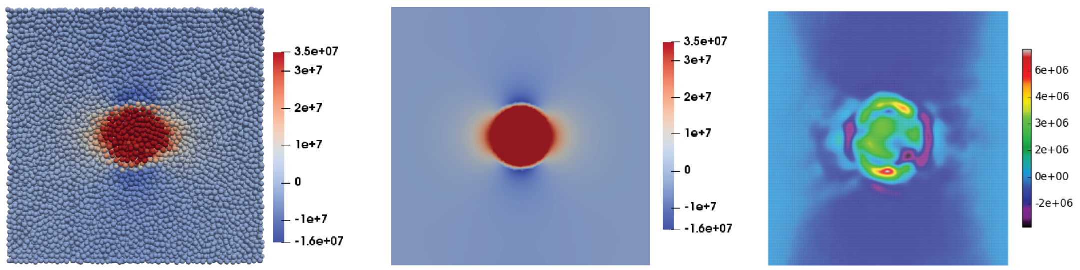

(a) σ_{xx} (b) σ_{xx} (c) Absolute difference σ_{xx}

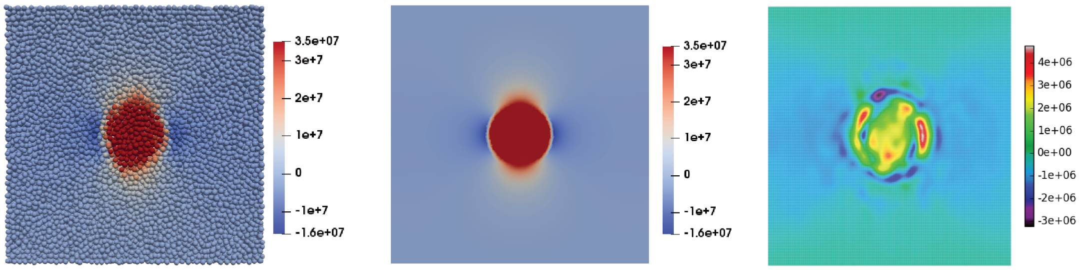

(d) σ_{yy} (e) σ_{yy} (f) Absolute difference σ_{yy}

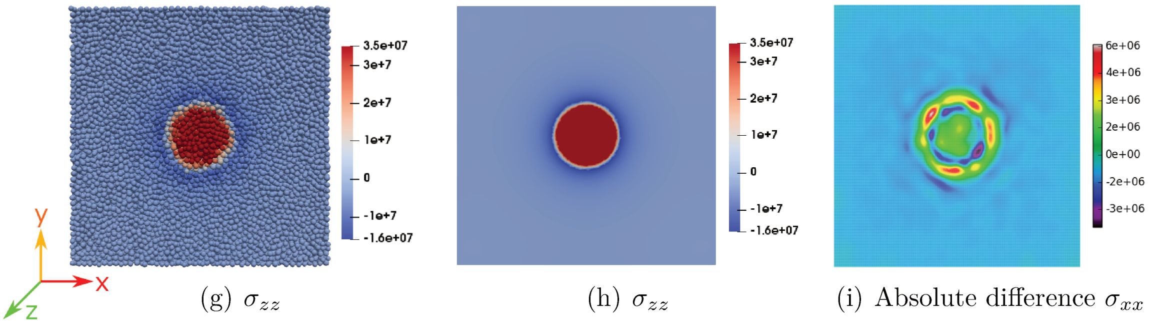

(g) σ_{zz} (h) σ_{zz} (i) Absolute difference σ_{xx}

Fig. B.II.26: DEM-FEM comparison of thermal stresses on median cross section, case of BA glass-alumina ($\alpha_m < \alpha_p$), ΔT = 120°C

between matrix and inclusion. Despite these discrepancies, the comparison results were globally acceptable for the whole cross section.

B.II.4.3.d Possible reasons of discrepancy between DEM, FEM and theoretical approaches

As it was shown previously, there was discrepancies between DEM, FEM and theoretical approaches. Especially, the discrepancies became more significant in the interfacial zone between matrix and inclusion in both 2 cases of reference materials. After examination, these discrepancies could mainly be explained by two reasons.

Firstly, the discrepancy might be issued from different discretization methods of DEM, FEM and theoretical approaches. Indeed, in DEM, the samples were

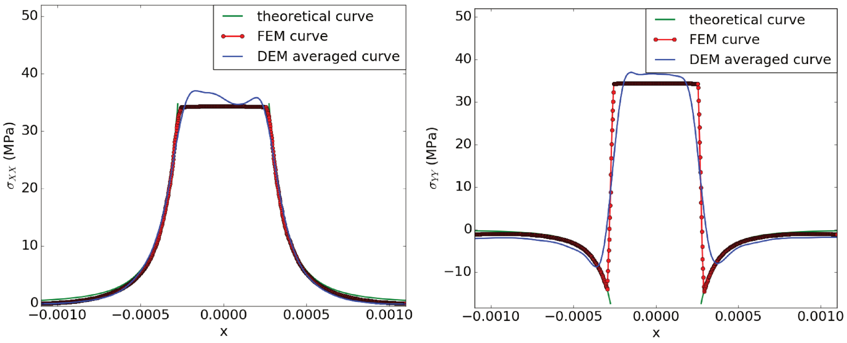

(a) σ_{xx} (b) σ_{yy}

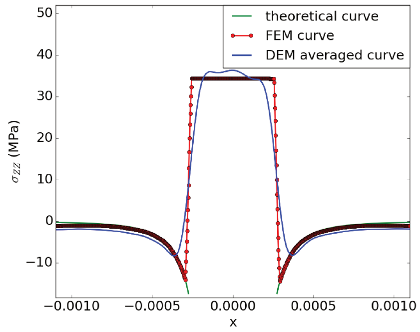

(c) σ_{zz}

Fig. B.II.27: Profile of normal stresses along the median line, case of BA glass-alumina ($\alpha_m < \alpha_p$), $\Delta T = 120$°C

discretized with lower number of elements than in FEM, whereas, the theoretical approach does not involve any discretization. In addition, the discrepancy of element number was more significant at the interfacial zone (Fig. B.II.28(a) and B.II.28(b)). The DEM-FEM discrepancy could be reduced by increasing the discrete element number of domain.

Secondly, the discrepancy might be caused by difference of stress computation methods between DEM and FEM approaches. Fig. B.II.29 illustrates a specific case where the discrete elements are close to the interface. Indeed, in the performed DEM simulations, the virial stress was computed in a specific range which contain the considered discrete element and it's neighbor elements (Sect. B.I.5.2). In the case shown in Fig. B.II.29, the discrete elements in the computation range of virial stress could belong to the matrix or the inclusion. Therefore, near the interface, in some cases, the stress computation of discrete elements were deducted from properties of two different materials. Whereas, in the performed FEM simulations, the stress was computed by using properties of only one material, either matrix

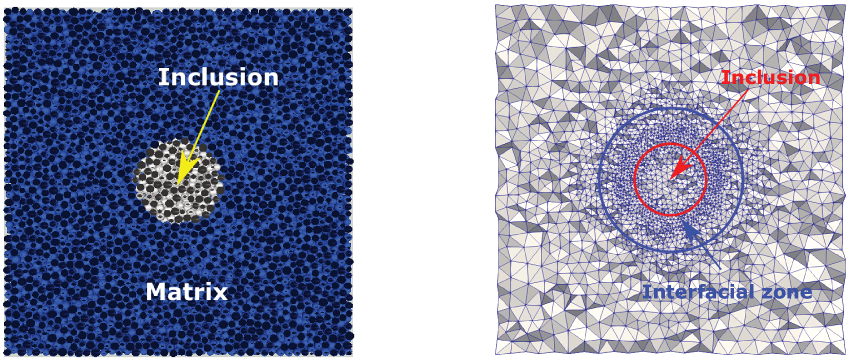

(a) DEM discretization (b) FEM discretization

Fig. B.II.28: Discretization of inclusion and interfacial zone

or inclusion. Consequently, different stress computation methods of DEM and FEM simulations might lead to the discrepancy of the obtained results. This issue might be solved by increasing the discrete elements number in the interfacial zone between inclusion and matrix. Indeed, the element sizes decrease as the discrete elements number increases and this reduces dimensions of the computation range of virial stress. Since the refinement of a specific zone has not been established yet, the proposed solution is a perspective of GranOO development team in the future.

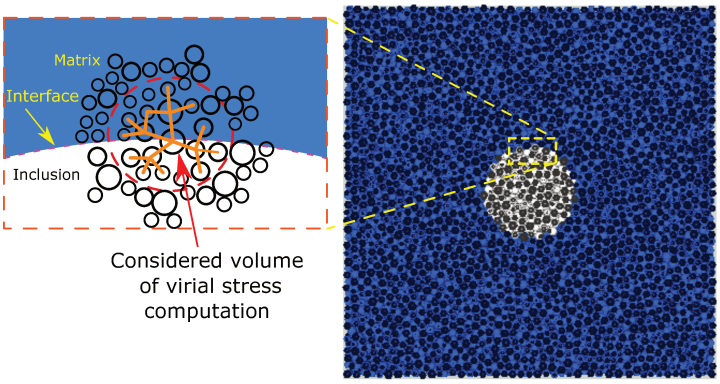

Fig. B.II.29: 2D illustration of virial stress computation of discrete elements near the interface

B.II.4.4 Thermal damages modeling

This section deals with the modeling of thermal damages in single-inclusion composites. Two configurations of damages due to thermal expansion mismatch during cooling process are illustrated in Fig. B.II.30. This figure involves a typical behavior of ceramic materials: tensile strength is much lower than compressive strength. Moreover, with regard to material 1 and material 2, the tensile strength of matrix is much lower than the tensile strength of inclusion. Consequently, the thermal damages are only generated within the matrix by tensile stresses. Based on Eq. B.II.21 and B.II.22, in the case of material 1 ($\alpha_m > \alpha_p$), the tensile stress in the matrix is in circumferential direction. Hence, in material 1, when the thermal tensile stress exceeds the critical value, radial micro-cracks could be generated within the matrix (Fig. B.II.30(a)). By contrast, in the case of material 2 ($\alpha_m < \alpha_p$), the tensile stress is in radial direction. Hence, in material 2, debondings could occur at the interface between matrix and inclusion (Fig. B.II.30(b)).

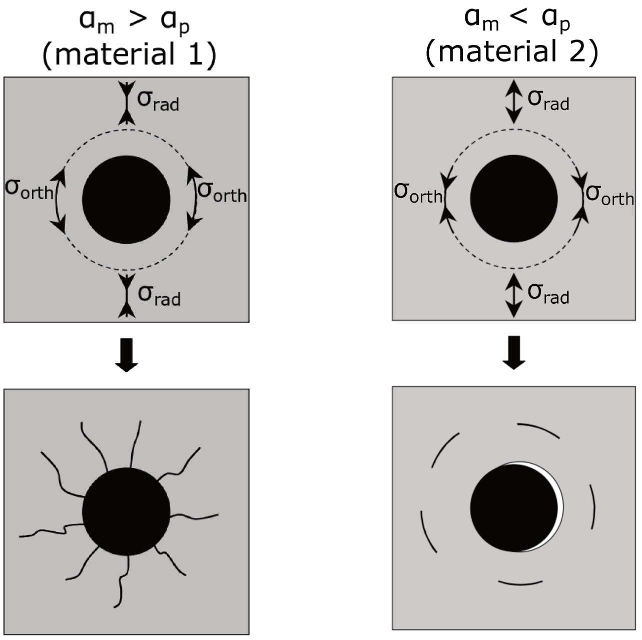

(a) Radial microcrack

(b) Debonding at interface

Fig. B.II.30: 2D illustration of damages due to thermal expansion mismatch during cooling [GK07]

In this section, in order to generate the thermal damages, the reference materials were subjected to cooling process, from the vitreous transition temperature (T_g) of matrices to ambient temperature (20°C). As explained previously, the starting points of cooling simulations were 455 and 555°C for material 1 and material 2, respectively. Then, the damage propagations issued from cooling simulations were compared to experimental observations [TD03, Jol06]. The damage visualization are shown in Fig. B.II.31 and B.II.32. As illustrated in Fig. B.II.31, for material 1, the micro-cracks are propagated along the radial direction of inclusion. Whereas, for material 2, debondings occur around the inclusion (Fig. B.II.32). These observations are compatible with experimental observations [TD03, Jol06] (Fig. B.II.32(c) and B.II.31(c)). Consequently, the proposed DEM model seems to be compatible to model damages due to thermal expansion mismatch. These phenomena will be further investigated for the multi-inclusion configuration in part C.

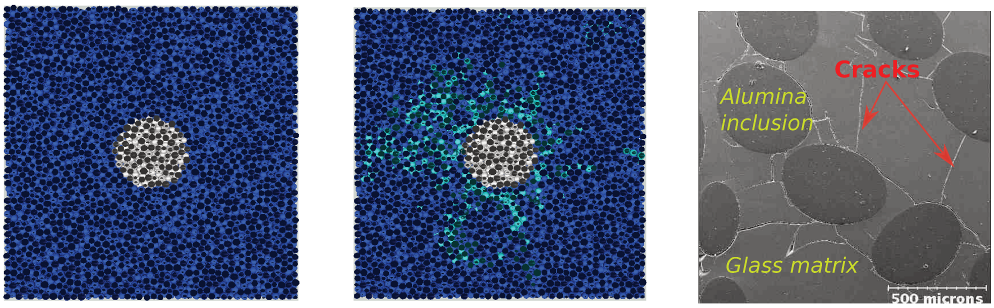

(a) Initial state (b) Radial cracks (c) Experimental result

Fig. B.II.31: Micro-crack propagation, view of median cross-section (Material 1)

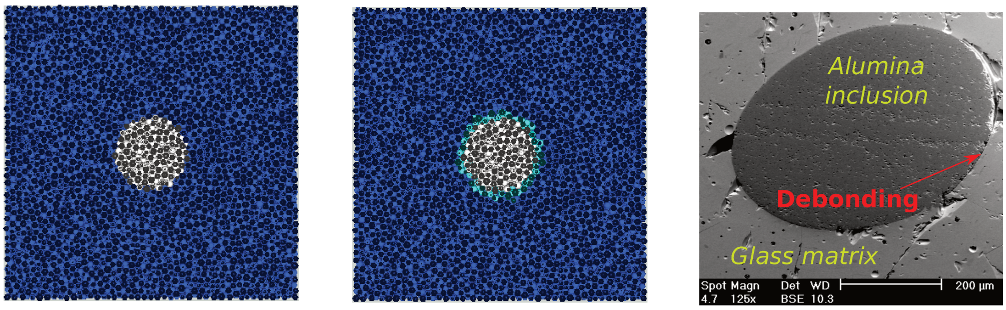

(a) Initial state (b) Interfacial debonding (c) Experimental result

Fig. B.II.32: Debonding propagation, view of median cross-section (Material 2)

B.II.4.5 Partial conclusions

The confrontation with FEM and theoretical approaches reveals the adaptability of the proposed discrete elements method to simulate the thermal stress due to thermal expansion mismatch and the associated damage phenomena. Indeed, in these preliminary configurations, i.e. single-inclusion composite, the virial-stress-based modeling given acceptable stress fields for 2 reference materials, in comparison with the FEM and theoretical approaches. Moreover, in the thermal damages modeling, the DEM produced quite adequate damage propagations, i.e. radial crack and debonding, in comparison with experimental observations available in the literature [TD03, Jol06]. The influence of thermal damages on the reference material will be further investigated in the case of multi-inclusion in part C.

B.II.5 Conclusion

The main objective of this chapter was to explain the direct calibration method and the virial stress concept. Indeed, the proposed calibration method allows us to compute directly the microscopic parameters from mechanical properties of material, regardless of type of numerical experiment, discrete elements number and geometrical properties of sample. This could eliminate the classical trial-and-error calibration method which is complicated and time consuming. The validation results highlight the accuracy of the proposed calibration method through different simulations, i.e. uniaxial tensile tests, hydrostatic compression tests, Brazilian tests and torsion tests. Up to now, this kind of macro-to-micro analysis has not been well established in the literature. Therefore, the direct calibration method was an important part of the present research. Moreover, the adaptability of virial-stress-based modeling to study thermal residual stresses and associated damages were also investigated on single-inclusion composites in this chapter (see B.II.4). In fact, the virial stress has been widely used in DEM only as a post-treatment analysis. However, this kind of computation has not been applied to the modeling of fracture phenomena, especially for continuous media. Thus, in the present research, the accuracy of the virial stress computation was evaluated with high attention. In the first simulations with single-inclusion configuration, the DEM results showed qualitatively and quantitatively a good agreement with FEM and theoretical results. These results validated the stress computation at scale of discrete element by using the proposed virial stress concept. Thus, this concept was used in order to investigate the thermal damages by using the microscopic fracture threshold developed in Sect. B.I.5. As expected, the damage propagations in the 2 reference materials obtained by DEM were compatible with experimental observations [TD03, Jol06]. The influence of the damage phenomena due to thermal expansion mismatch will be further investigated in Part C by using multi-inclusion composites.

Part C

Numerical modeling of microstructure-properties relationship of model materials

Introduction

Part C focuses on the modeling of thermal damage phenomena and their influence on apparent behaviors of model materials. Again, the model material developed by Tessier-Doyen [TD03] were used in this part to evaluate numerical results obtained by DEM. Part C includes two chapters.

The first chapter is dedicated to the main steps of cooling simulation. Virtual samples that contain multiple spherical inclusions are used in order to reproduce *Statistical Volume Element* of model materials. In order to study the influence of alumina content on the damage phenomena, three volume fractions were considered: 15%, 30% and 45%. The main assumptions that were used in part C are also detailed.

The second chapter presents the confrontation of DEM results against experimental data of Tessier-Doyen as well as the Hashin & Strickman model. The evolution of Young's modulus and coefficient of thermal expansion (CTE) as functions of temperature is investigated, regarding the effect of thermal damages. In addition, qualitative DEM results of nonlinear tensile behavior of model materials are discussed, regarding the experimental observations that were reported in literature. These comparisons allows to evaluate the ability of the developed DEM modeling platform to model complex damage phenomena and their effects on thermomechanical properties of heterogeneous materials.

Chapter C.I

Development of numerical laboratory

C.I.1 Simulation of cooling stage

C.I.1.1 Construction of heterogeneous sample

In order to mimic the microstructure of model materials, sample that contains multiple spherical inclusions were built to create *Statistical Volume Element* (Fig. C.I.1).

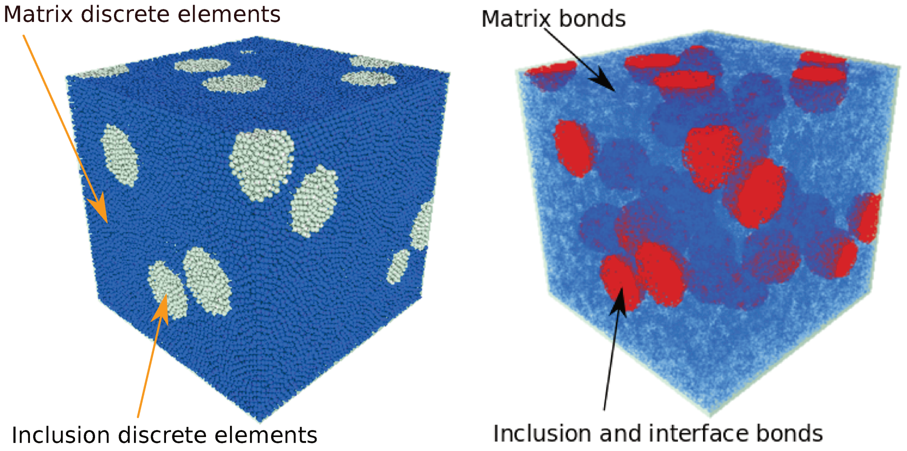

(a) View with discrete elements (b) View with bonds only

Fig. C.I.1: Statistical Volume Element of the two-phase model materials

In the present study, the *Statistical Volume Element* of heterogeneous material were generated by using the methodology proposed by André *et al.* [ALTDH17].

More specifically, the generation of multi inclusion sample was carried out through 3 steps (Fig. C.I.2).

Step 1 - Generation of homogeneous discrete domain: in this step, the *Cooker algorithm* is used to create homogeneous domain (Sect. B.I.3.2);

Step 2 - Creation of each inclusion: From the initial domain and the targeted properties (volume fraction of inclusion, average radius of inclusion and radius dispersion), inclusions are created one by one thanks to a finite loop. In this step, the center of spherical inclusion is distributed randomly within the homogeneous domain. The radius of inclusion varies randomly around an averaged value with a predefined dispersion. More specifically, a controlled number of discrete elements around the center of new inclusion are assigned to a *temporary set of elements*. The distance between the affected elements and the center of new inclusion must be lower than the radius of inclusion. During this process, the overlapping between inclusions is forbidden. If overlapping between the *temporary set of elements* with the other inclusions is detected, the affected discrete elements are withdrawn from this *temporary set*. Then, the insertion of newest inclusion restarts by choosing an other position of inclusion center. Step 2 is repeated until the insertion of new inclusion succeeds and the process switches to the next step;

Step 3 - Computation of volume fraction of inclusion: in this step, the current volume fraction of inclusion is computed in order to control the creation of inclusions. In this study, the computation of volume fraction involves only number of interaction pair that link discrete elements together (Sect. B.I.3.2). Here, the heterogeneous sample could have three types of interaction pairs (called *bond*): matrix, inclusion and interface bonds (Fig. C.I.1(b)). In the present research, for simplicity, the *interface bonds* that link *matrix* discrete elements and *inclusion* discrete elements were considered to have properties of *inclusion* bonds. The proposed computational method of volume fraction will be detailed in the next section.

Steps 2 and step 3 are repeated until the current volume fraction of inclusion reaches the targeted value. Finally, the *Statistical Volume Element* of model material is obtained.

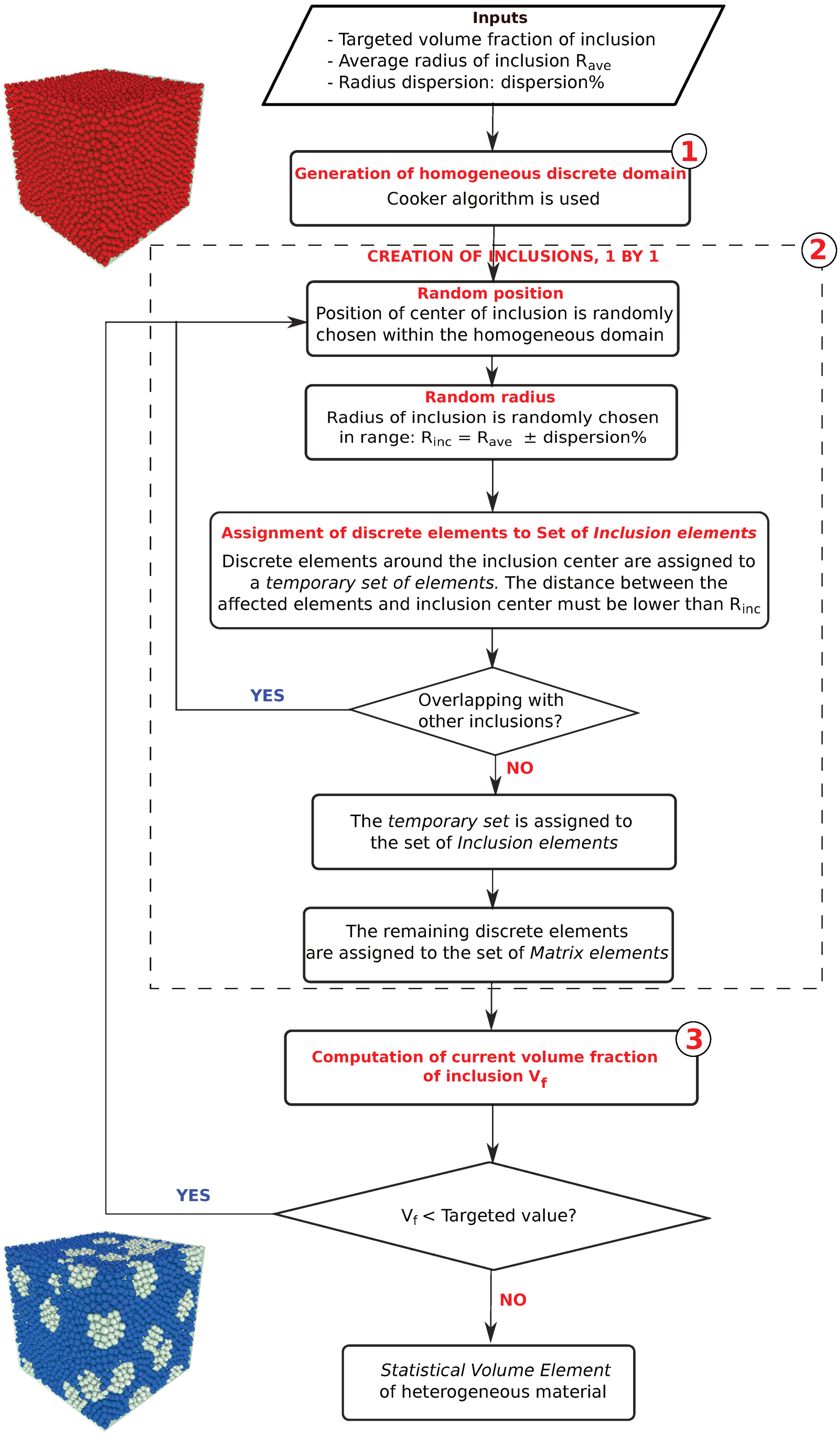

Fig. C.I.2: Illustration of geometrical algorithm to build heterogeneous sample

C.I.1.2 Synthesis of numerical investigation

In order to investigate the influence of thermal damages on behavior of Tessier-Doyen's model materials [TD03], numerical processes were carried out through 4 main steps:

Step 1 - Creation of Statistical Volume Element: Samples that contains multiple spherical inclusions were built. As presented in paragraph C.I.1.1, spherical inclusions were created and distributed randomly in a cubic sample with a controlled volume fraction, i.e. 15%, 30% and 45%. The radius of inclusion was the same as in the real material, i.e. 250 μm± 10%. The dimensions of the virtual cubic sample were set as *2.2 mm* in order to reproduce an adequate *Statistical Volume Element* with a reasonable number of inclusion within the matrix (Fig. C.I.1(a)). In the present study, number of discrete elements was around 120,000 in order to ensure a good compromise between the precision of the results and the computational time. Thus, the number of discrete elements of each inclusion was about 900. Moreover, three *Statistical Volume Elements* were created from three different homogeneous domains for each volume fraction of inclusion. The purpose of this duplication is to ensure the reproducibility of numerical results and to alleviate the influence of random distribution of discrete elements in the *cooker* algorithm (Sect. B.I.3.2). Consequently, hereafter, numerical results associated to each volume fraction of inclusion are average results of three different heterogeneous samples;

Step 2 - Cooling simulation of two-phases material: Input parameters were set at scale of discrete elements in order to obtain thermomechanical properties of the two reference materials, e.g. Cofer glass-alumina and BA glass-alumina. The same values of input parameters in Tab. B.II.16 (Young's modulus, radius ratio, fracture threshold and CTE) were used here. Since the present study focused only on solid behavior, the cooling stage were modeled from vitreous transition temperature of glasses to 20°C (See paragraph B.II.4.1). The transition temperatures T_g of glasses are taken from [TD03]: T_g are 455 and 555°C for Cofer glass and BA glass, respectively. During cooling simulation, thermal stress increases as the temperature decrease from Tg, due to thermal expansion mismatch. Consequently, when thermal stresses exceed critical value, damages occurs within material;

Step 3 - Measurements of apparent Young's modulus: Thermally damaged samples obtained in step 2 were submitted to tensile tests in order to measure their apparent Young's modulus. Following the same principles presented in paragraph B.I.4.3.a, opposite displacement of 50 μm are imposed to two opposite surfaces of damaged samples. In addition, the tensile strength of materials was set to an infinite value in order to forbid the crack extension. This technique is comparable with measurement of Young's modulus by the Ultrasonic technique, which is non destructive;

Step 4 - Measurements of apparent CTE: The CTE α of damaged samples could be simply deduced from the results of cooling simulations:

$$\alpha = \frac{\varepsilon}{\Delta T} \tag{C.I.1}$$

where, ε is the thermal deformation of numerical sample during cooling simulation and ΔT is the temperature variation.

Globally, in order to focus on damage phenomena due thermal expansion mismatch during cooling stage, the following assumptions were used:

- The temperature field was considered as uniform in the whole virtual sample (heat transfer was considered as infinite);
- Intrinsic evolution of Young's modulus of each constituents as a function of temperature was considered in the simulation (Fig. A.I.13);
- In order to model brittle materials, damage occurred only in tensile mode. More specifically, crack initiation is managed by *virial stress* concept (Sect. B.I.5): if the computed virial stress of a discrete elements exceeds predefined thresholds for each glass matrix, its connected beams are destroyed. By contrast, the failure in compression was not considered;
- In the present research, only crack opening was considered. The crack closure could be modeled, however, the crack healing phenomenon was not investigated.

C.I.2 Simulation of evolution of Young's modulus versus temperature

C.I.2.1 Main principles

This chapter focuses on the effect of thermal damages on thermomechanical properties of the two reference materials, regarding the evolution of elastic properties versus temperature of their constituents. Therefore, the direct calibration method (Sect. B.II.2) was used to vary input parameters as function of temperature, in order to reproduce the evolution of elastic properties of each constituent. In the present study, only evolution of Young's modulus of the constituents (Cofer glass, BA glass, alumina) was taken into account. In fact, from transition temperature of glass to ambient temperature, the Poisson's ratio and CTE of these constituents are quite stable and independent from temperature. Therefore, in DEM simulations, the Poisson's ratio and CTE of the constituents were considered as constant.

Firstly, the input parameter r_m (radius ratio) is computed from Poisson's ratio ν_M of material by using the direct calibration method:

$$a_1 + b_1.r_m + c_1.r_m^2 + d_1.r_m^3 - \nu_M = 0 \tag{C.I.2}$$

As discussed in paragraph B.II.2.2.c, Eq. C.I.2 has generally unique solution of r_m in range from 0 to 1. Since ν_M is considered as constant, r_m is also constant during cooling simulation.

Secondly, the ratio between Young's modulus of material E_M and input parameter E_m is given by:

$$K_E = \frac{E_M}{E_m} = a_2 + b_2.r_m + c_2.r_m^2 + d_2.r_m^3 \tag{C.I.3}$$

Since r_m is constant, K_E is also constant during cooling simulation. Hence, in order to reproduce the evolution of Young's modulus of material $E_M(T)$, the input parameter $E_m(T)$ could be set by using the following equation:

$$E_m(T) = \frac{E_M(T)}{K_E} \tag{C.I.4}$$

In this study, the Young's modulus obtained by Ultrasonic technique of the 3 considered constituents [TD03] were described by algebraic equations $E_M(T)$

resulting from nonlinear regression. Fig. C.I.3 shows that these simple equations could describe well the evolution of Young's modulus.

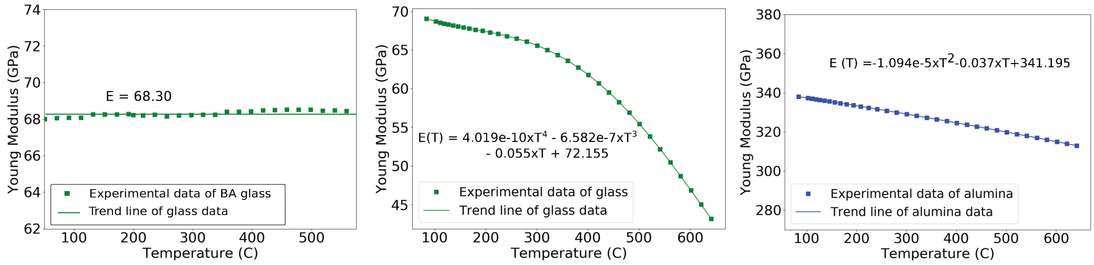

(a) BA glass (b) Cofer glass (c) Alumina

Fig. C.I.3: Nonlinear regression of ultrasonic measurement: Young's modulus versus temperature

As illustrated in Fig. C.I.3(a), the Young's modulus of BA glass is quite independent from temperature. Therefore, in this study, the input parameters were considered as constant to model BA Glass. By contrast, the Young's modulus of cofer glass and alumina could be described by a polynomial of degree four and a polynomial of degree two, respectively (Fig. C.I.3(b) and C.I.3(c)). Therefore, for cofer glass and alumina, the evolution of E_m was deduced from $E_M(T)$ by using Eq. C.I.4.

As presented in chapter B.II, the direct calibration method were validated for case of constant temperature. In part C, the variation of temperature is taken into account for the first time. Hence, a validation is necessary to ensure the accuracy of the direct calibration in case of varied temperature. For this purpose, cooling simulation of cofer glass and alumina were carried out with variation of E_m. Then, the Young's modulus of homogeneous sample at certain moments of cooling simulation is measure by tensile test (paragraph B.I.4.3.a). The comparison between Young's modulus obtained by DEM and Ultrasonic measurement is shown in Fig. C.I.4.

As illustrated, DEM results show a good agreement with experimental measurement of Young's modulus (Fig. C.I.4(a) and C.I.4(b)). These results confirmed the accuracy of the direct calibration method to reproduce the evolution of Young modulus as function of temperature of homogeneous materials.

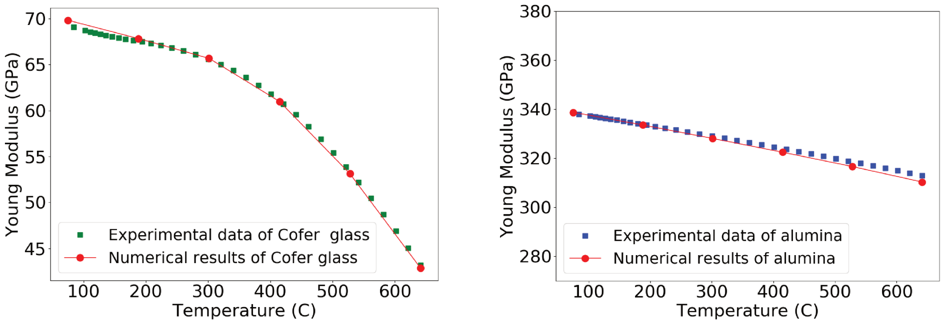

(a) Cofer glass (b) Alumina

Fig. C.I.4: Validation of direct calibration to reproduce evolution of Young's modulus: Comparison between DEM results and experimental data

C.I.2.2 Computation of volume fraction

Naturally, the volume fraction of inclusion in the *Statistical Volume Element* f_V^I could be computed by considering the *occupied volume* of each set of elements, i.e. *Inclusion elements* and *Matrix elements*:

$$f_V^I = \frac{V^o_{\text{Iset}}}{V^o_{\text{Total}}} \tag{C.I.5}$$

where, V^o_{Iset} is the *occupied volume* of *Inclusion elements set* and V^o_{Total} is the *occupied volume* of the whole discrete domain.

However, as presented in Sect. B.I.3, voids exist between discrete elements. In other words, assembly of discrete elements does not fill completely the occupied volume. Thanks to the *cooker algorithm*, the ratio between the sum of discrete element volumes and the *"real"* volume that they occupied could be controlled. This ratio is homogeneous for the whole discrete domain and its value f_v is around 0.63 (Sect. B.I.3). Thus, the occupied volume V^o_{Iset} and V^o_{Total} could be deduced from the sum of discrete element volumes as follows:

$$V^o_{\text{Iset}} = \frac{V^e_{\text{Iset}}}{f_v} \tag{C.I.6}$$

$$V^o_{\text{Total}} = \frac{V^e_{\text{Total}}}{f_v} \tag{C.I.7}$$

where, V^e_{Iset} is the sum of discrete element volumes of *Inclusion elements set* and V^e_{Total} is the sum of discrete element volumes of the whole discrete domain.

Taking into account the Eq. C.I.5, C.I.6 and C.I.7, the existence of voids does not affect the computation of volume fraction of inclusion:

$$f_V^I = \frac{V^o_{\text{Iset}}}{V^o_{\text{Total}}} = \frac{\dfrac{V^e_{\text{Iset}}}{f_v}}{\dfrac{V^e_{\text{Total}}}{f_v}} = \frac{V^e_{\text{Iset}}}{V^e_{\text{Total}}} \tag{C.I.8}$$

To simplify the Eq. C.I.8, the sum of discrete element volumes V^e_{Iset} and V^e_{Total} could be computed as follows:

$$V^e_{\text{Iset}} = N^e_I \times \overline{V^e} \tag{C.I.9}$$

$$V^e_{\text{Total}} = N^e_T \times \overline{V^e} \tag{C.I.10}$$

where N^e_I is the number of elements in *Inclusion set*, N^e_T is the total number of discrete element and $\overline{V^e}$ is the average volume of discrete elements.

Thus, Eq. C.I.8 could be simplified as follows, involving only element number:

$$f_V^I = \frac{V^e_{\text{Iset}}}{V^e_{\text{Total}}} = \frac{N^e_I}{N^e_T} \tag{C.I.11}$$

Herein, the Eq. C.I.11 need to be modified in order to match with the specific *Statistical Volume Element* of heterogeneous material. Indeed, in the present research, the interface bonds are considered to have properties of inclusion bonds (Sect C-C.I.1.1). In order to take into account this specification, the number of bonds should be involved. For this purpose, the number of elements is related to the number of bonds as follow:

$$N^e_I = \frac{2N^b_I}{cn} \quad ; \quad N^e_T = \frac{2N^b_T}{cn} \tag{C.I.12}$$

where, cn is the coordination number (paragraph B.I.3.2); N^b_I is the number of *inclusion bonds* and N^b_T is the total number of bonds.

Hence, the volume fraction could be computed as follows:

$$f_V^I = \frac{N^e_I}{N^e_T} = \frac{(\dfrac{2N^b_I}{cn})}{(\dfrac{2N^b_T}{cn})} = \frac{N^b_I}{N^b_T} \tag{C.I.13}$$

As mentioned above, in this study, the *interface bonds* are considered as *inclusions bonds* (Fig. C.I.5).

Therefore, the *interface bonds* and the *inclusion bonds* should be counted

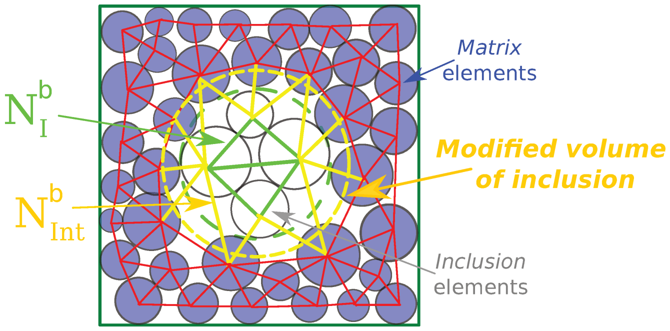

Fig. C.I.5: 2D illustration of computation of volume fraction of inclusion, taking into account the specific properties of *interface bonds*

together in order to compute more accurately the volume fraction $f_V^{I^*}$:

$$f_V^{I^*} = \frac{N_I^b + N_{Int}^b}{N_T^b} \tag{C.I.14}$$

where N_{Int}^b is number of interface bonds.

C.I.2.3 Application on undamaged heterogeneous material

After validation on homogeneous material (paragraph C.I.2.1), the direct calibration method was used to reproduce the evolution of Young modulus as function of temperature of heterogeneous material.

As discussed in paragraph A.I.3.3, the lower bound of HS model could describe well the Young's modulus of two-faces material when there is no damage. Therefore, the apparent Young's modulus obtained by DEM were compared to experimental data of two-phases model material and HS model. More specifically, cooling simulation of two-phases material with variation of Young's modulus of their constituents were carried out. Again, cooling were simulated from transition temperature T_g of glasses to 20°C. In addition, the tensile strength of glass matrices were set as infinite to avoid influence of damages. The purpose was to examined the proposed numerical process, taking into account the evolution intrinsic of constituents and the volume fraction of inclusion, through its application to two-phases materials. The comparison is reported in Fig. C.I.6.

In Fig C.I.6, at the beginning of cooling, since there is no damage, the HS-curves follow well the experimental data of Young's modulus for both two model materials. As expected, the DEM results are close to the entire HS- curves for the two model materials (Fig C.I.6). For samples of 15% alumina, DEM results

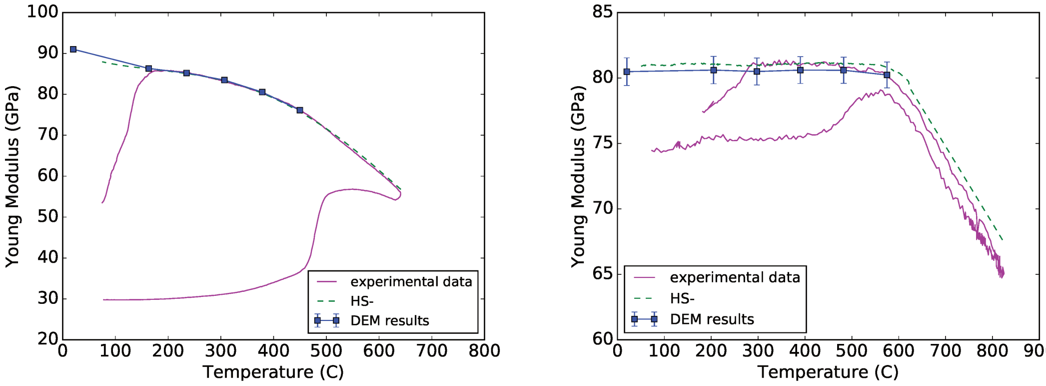

(a) Cofer glass-alumina (15%) (b) BA glass-alumina (15%)

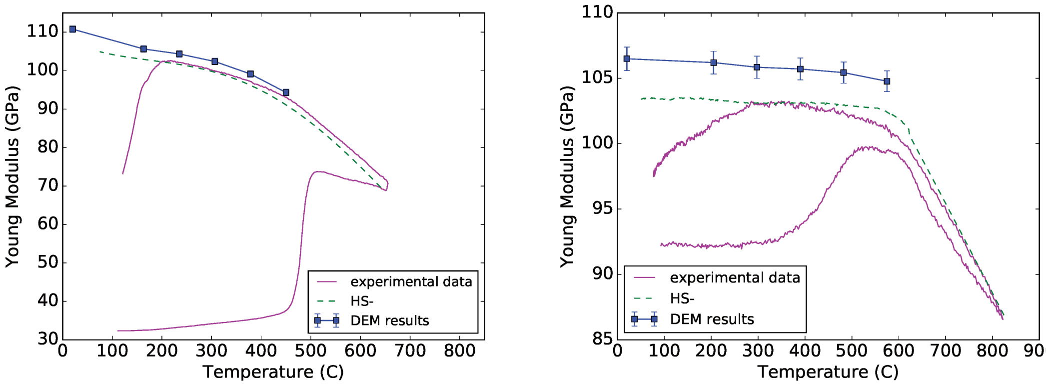

(c) Cofer glass-alumina (30%) (d) BA glass-alumina (30%)

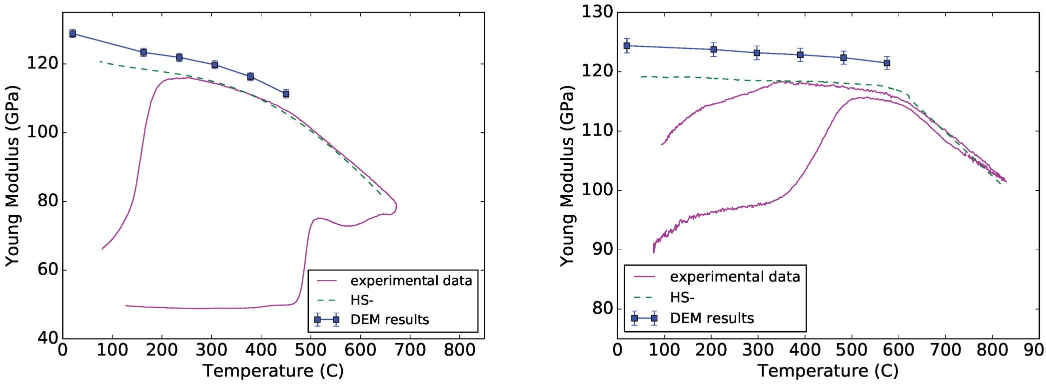

(e) Cofer glass-alumina (45%) (f) BA glass-alumina (45%)

Fig. C.I.6: Comparison between DEM results, experimental data and HS model: case of undamaged model materials

almost overlap HS- curves. However, the difference between DEM results and HS model increases in the case of 30% and 45% alumina. Although the reason of this observation is still questionable, it is perhaps interesting to investigate if the Periodic boundary conditions could reduce the differences. However, since this feature has not been available in the modeling platform yet, the *Statistical Volume Elements* were used to investigate the effect of thermal damages on thermomechanical properties of model materials.

Chapter C.II

Modeling of thermomechanical damages in model materials

As mentioned in Part A, the key advantage of DEM is to take into account complex damage phenomena to model behavior of refractories. Herein, the obtained DEM results on damaged model materials will be confronted with experimental data and HS model. This chapter is structured in 4 sections:

- Visualization of damage morphology;
- Evolution of Young's modulus during cooling;
- Thermomechanical properties at room temperature of damaged samples after cooling;
- Qualitative simulation of nonlinear tensile behavior due to thermal damages.

C.II.1 Qualitative simulation of thermal damages

In this section, the DEM results of thermal damage phenomena will be presented and compared with experimental observations for the two reference materials. More specifically, the initiation and propagation of thermal damages as well as the morphology of damage network will be discussed.

C.II.1.1 Micro-crack propagation

Fig. C.II.1 shows the crack propagation during cooling stage of Cofer glass-alumina. In this case, the CTE of alumina inclusion is lower than that of glass matrix. Hence, alumina inclusion contracts less than glass matrix and this impedes free contraction of Cofer glass. Therefore, orthoradial tensile stresses were generated within glass matrix whereas compressive stresses were generated within alumina inclusions (See paragraph A.I.1.2).

Firstly, as illustrated in Fig. C.II.1, multiple cracks propagate simultaneously along the radial direction of inclusions. This observation is compatible with the related stress state. Secondly, after extension, thermal cracks interact and connect with each other. Consequently, a crack network developed strongly within the *Statistical Volume Element*. Qualitatively, the topology of crack network obtained by DEM showed a good agreement with experimental observations that have been reported in literature (Fig. C.II.2).

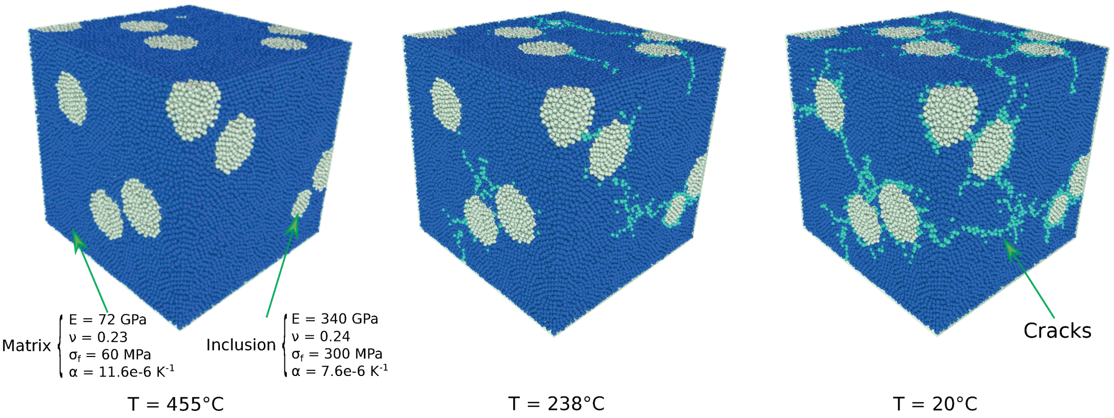

Fig. C.II.1: Crack propagation during cooling simulation of Cofer glass-alumina

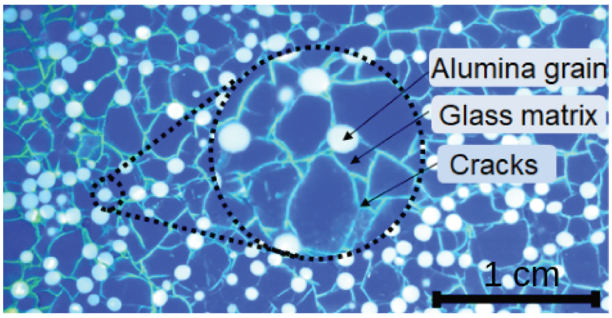

Fig. C.II.2: Microcracks within Cofer glass-alumina, highlighted by fluorescent UV dye [TD03]

C.II.1.2 Debonding at interfaces

Fig. C.II.3 shows the debonding phenomenon during cooling of BA glass-alumina. In this case, the CTE of alumina inclusion is higher than that of glass matrix. Thus, alumina inclusion contracts more than BA glass matrix. Therefore, radial tensile stresses were generated within glass matrix and tensile stresses were also generated within alumina inclusions (See paragraph A.I.1.2). In addition, tensile strength of alumina is much higher than that of glass matrix. Consequently, in DEM simulations, multiple damages occur simultaneously at the interface between the matrix and alumina inclusions (Fig. C.II.3). This observation is compatible with the corresponding stress state. Fig. C.II.4 shows the observation of debonding phenomenon within BA glass-alumina by Scanning Electron Microscopy (SEM) technique [Jol06]. Qualitatively, the DEM reproduced an adequate topology of damage network in comparison with experimental observations in [Jol06].

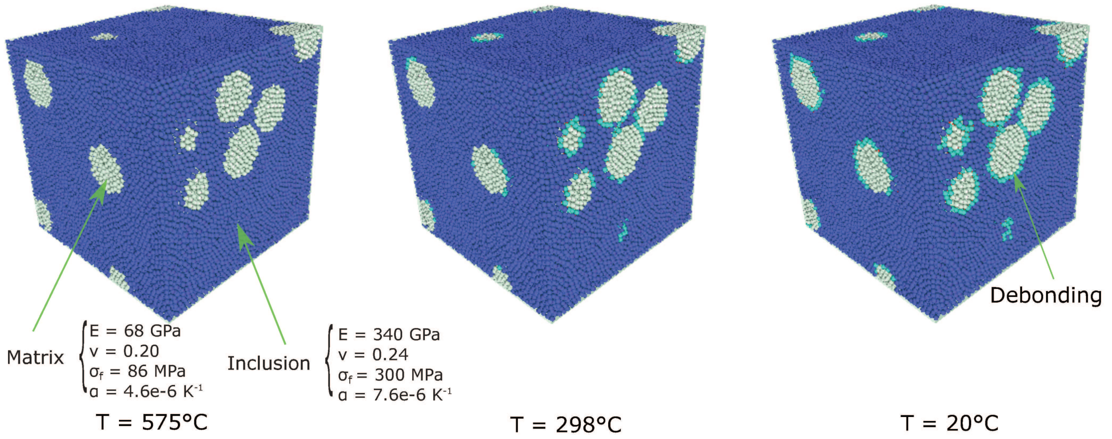

Fig. C.II.3: Development of debonding phenomena during cooling of BA glass-alumina

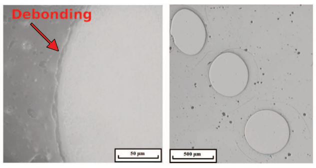

Fig. C.II.4: Interfacial debonding within two-phases material by SEM [Jol06]

C.II.2 Mechanical properties versus temperature

C.II.2.1 Determination of tensile strength of glass matrices

In the present research, the thermomechanical properties of model material reported in [TD03] were used in order to performed DEM simulations: Young's modulus, Poisson's ratio, CTE and tensile strength. Obviously, these thermomechanical properties of material are key input parameters that govern the results of numerical simulations. Generally, quantitative numerical simulations are difficult to carry out if robust experimental value of tensile strength is missing. In addition, for ceramic material, the value of tensile strength depends strongly on the dimension of sample and characterization technique. Therefore, in this study, the chose of experimental value of tensile strength of glass is still questionable.

In [TD03], for cofer glass and BA glass, the author estimated their tensile strength σ_f by using analytical expression of thermal stress [Sel61]:

$$\sigma_f = \frac{(\alpha_m - \alpha_p)\Delta T}{\dfrac{1+\nu_m}{2E_m} + \dfrac{1-2\nu_p}{E_p}} \tag{C.II.1}$$

where ΔT is the critical variation of temperature that initiate thermal damages within the matrix.

Typically, ΔT could be computed by the difference between T_g of glass and the critical temperature T_c, from which thermal damages appears significantly within the glass. In practice, T_c could be detected by a brutal decrease of Young's modulus during cooling. By using this method, tensile strength of Cofer glass and BA glass were estimated as 60 MPa and 86 MPa, respectively [TD03]. Later on, in [Jol06], the author determined tensile strength of BA glass by 4 point bending test. The dimension of sample were 4x4x50 mm^3.

These values of tensile strength of glasses are summarized in Tab. C.II.1.

Tab. C.II.1: Tensile strength of glasses by different techniques

	Value (MPa)	Technique	Reference
Cofer	60	Analytical formula	[TD03]
BA	86	Analytical formula	[TD03]
BA	45	4 Points Bending test	[Jol06]

In the present study, these values of tensile strength of glasses were used in order to perform DEM simulations.

C.II.2.2 Model material with radial-propagated crack

In this paragraph, the results of cofer glass-alumina composite are discussed. Again, the apparent Young's modulus during cooling obtained by DEM were compared to experimental data of two-phases model material and HS model (Fig. C.II.5).

As a remark, the measurement of Young's modulus during the final stage of cooling is usually not possible due to failure of the alumina cement used to stick the sample to the waveguide because of thermal expansion mismatch between this alumina cement and the sample. Therefore, in the results of Tessier-Doyen [TD03], the Young's modulus was measured at room temperature after the thermal cycle. Hence, the final evolution at the end of cooling is plotted in dotted line. In Fig. C.II.5, experimental value of Young's modulus at 20°C is averaged results of 3 samples.

Herein, two values of tensile strength of Cofer glass were used for DEM simulation. The left column (Fig. C.II.5(a), C.II.5(c) and C.II.5(e)) corresponds to tensile strength proposed in [TD03], based on analytical model of thermal stress [Sel61], i.e. $\sigma_f = 60$ MPa. The right column (Fig. C.II.5(b), C.II.5(d) and C.II.5(f)) corresponds to higher value of tensile strength, i.e. $\sigma_f = 90$ MPa. The purpose is to observe the dependence of numerical results on input value of tensile strength.

Considering the DEM results, at the beginning of cooling, since material is free of damage, the numerical results is very close to the experimental curve and HS- curve. Then, since the thermal stresses increase as the temperature decreases, damages occur and cause an important decrease of Young's modulus. The DEM results has a similar tendency with experiment data: the drop of Young's modulus due to micro-cracks increase as the alumina content increases (Fig. C.II.5). This observation is quite reasonable because the increase of alumina content promotes micro-crack network and therefore, increases the drop of Young's modulus. Regarding the value of tensile strength, firstly, $\sigma_f = 60$ MPa gives more relevant results of Young's modulus at room temperature, in comparison with experimental data. Secondly, in case of $\sigma_f = 90$ MPa, the damages occurred at lower temperature than in case of $\sigma_f = 60$ MPa. However, with both these two values, damages occurred at higher temperature during cooling, in comparison with experimental results. This observation is still questionable in the present research. As a perspective, it is perhaps interesting to investigate further the dependence of numerical results on periodic boundary conditions and configuration of virial stress concept.

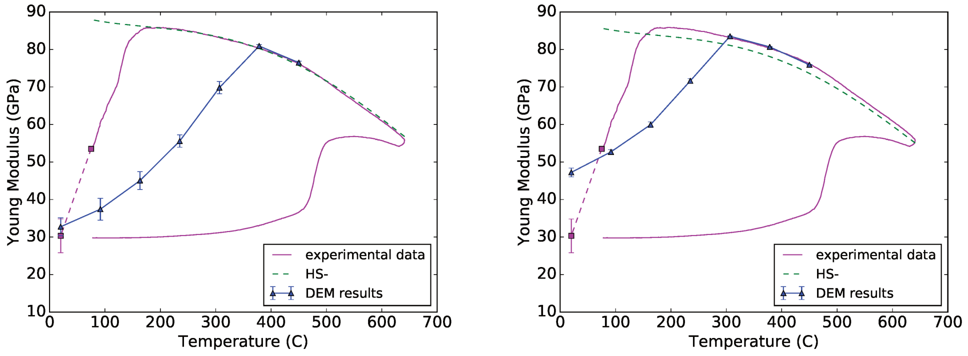

(a) 15% alumina, $\sigma_f = 60$ MPa (b) 15% alumina, $\sigma_f = 90$ MPa

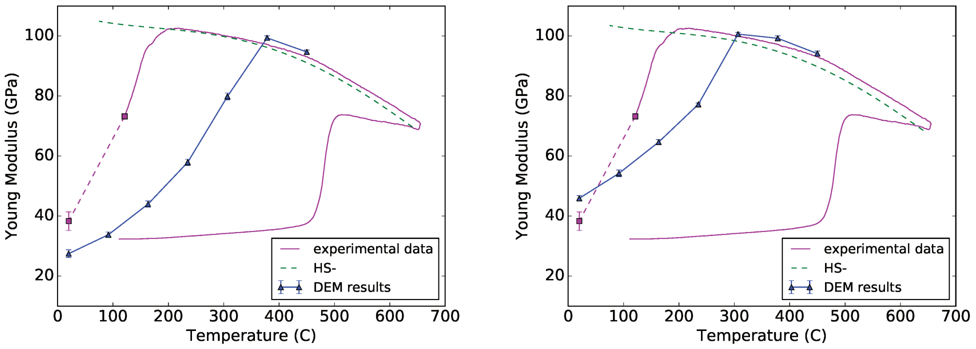

(c) 30% alumina, $\sigma_f = 60$ MPa (d) 30% alumina, $\sigma_f = 90$ MPa

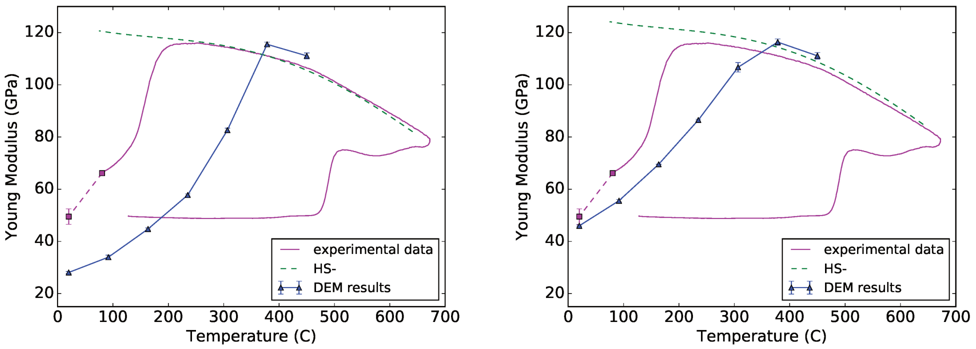

(e) 45% alumina, $\sigma_f = 60$ MPa (f) 45% alumina, $\sigma_f = 90$ MPa

Fig. C.II.5: Comparison between DEM results, experimental data and HS model: Young's modulus versus temperature during cooling (Cofer glass-alumina composite)

C.II.2.3 Model material with debonding at interfaces

In this paragraph, the results of BA glass-alumina composite are discussed. Again, the apparent Young's modulus during cooling obtained by DEM were compared to experimental data of two-phases model material and HS model (Fig. C.II.6).

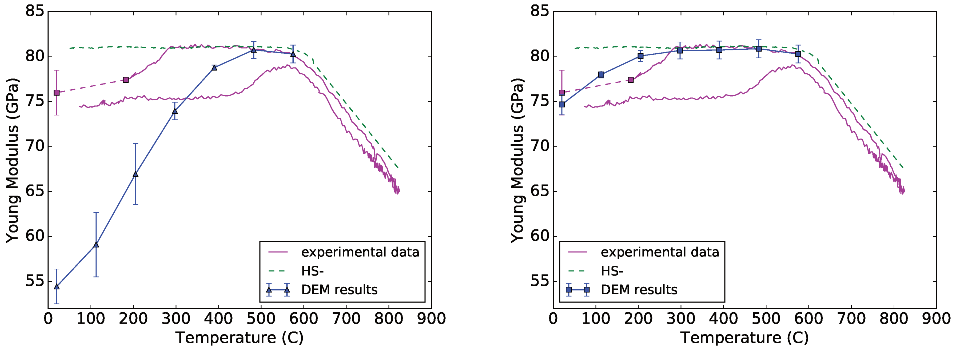

(a) 15% alumina, $\sigma_f = 45$ MPa (b) 15% alumina, $\sigma_f = 86$ MPa

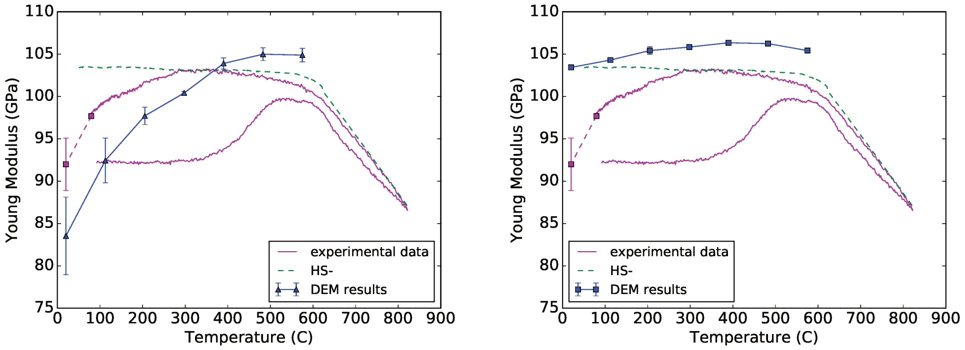

(c) 30% alumina, $\sigma_f = 45$ MPa (d) 30% alumina, $\sigma_f = 86$ MPa

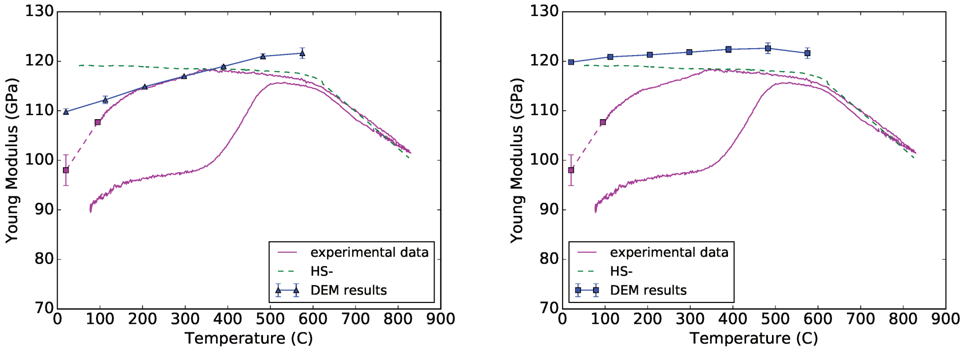

(e) 45% alumina, $\sigma_f = 45$ MPa (f) 45% alumina, $\sigma_f = 86$ MPa

Fig. C.II.6: Comparison between DEM results, experimental data and HS model: Young's modulus versus temperature during cooling (BA glass-alumina composite)

Similarly to the case of Cofer glass-alumina, the Young's modulus at the end of experimental cooling was measured at room temperature, after the thermal cycle. In this paragraph, two values of tensile strength of BA glass were used. The left column (Fig. C.II.6(a), C.II.6(c) and C.II.6(e)) corresponds to tensile strength that were measured by 4 points bending test in [Jol06], i.e. $\sigma_f = 45$ MPa. The right column (Fig. C.II.6(b), C.II.6(d) and C.II.6(f)) corresponds to tensile strength proposed in [TD03], based on analytical model of thermal stress [Sel61], i.e. $\sigma_f = 86$ MPa.

As a first remark, DEM results show that, in case of debonding, the Young's modulus drops less than in the case of micro-crack. This tendency is comparable with experimental data. These observations are reasonable since in debonding case, thermal damages do not connect and do not interact with each other as in the case of micro-cracking.

The second remark is related to the dependence of DEM results on value of tensile strength of BA glass. As shown in Fig. C.II.6(a) and C.II.6(b), for case of 15% alumina, the DEM results obtained with $\sigma_f = 45$ MPa is less relevant than that obtained with $\sigma_f = 86$ MPa, in comparison with experimental data. However, for cases of 30% and 45% alumina, the tensile strength value proposed by Joliff give more relevant value of Young's modulus at 20°C, in comparison with experimental data. Indeed, the tensile strength value proposed by Tessier-Doyen seems to underestimate the effect of damage on Young's modulus in case of high alumina content.

Finally, for both two values of tensile strength, in case of 45% alumina, the Young's modulus decreases less than in cases of lower alumina contents. This remark is not observed in experimental data. Hence, as a perspective, further investigation should be carried out in order to clarify this remark.

C.II.3 Influence of volume fraction of inclusion on thermomechanical properties of materials

In this Section, the effect of thermal damages on thermomechanical properties at room temperature of model materials is evaluated, considering different volume fractions of alumina: 15%, 30% and 45%. The DEM results were confronted with both experimental data and HS model in order to evaluate their accuracy. Two different simulation configurations were examined: *'DEM non damaged samples'* and *'DEM damaged samples'*.

The *'DEM non damaged samples'* configuration corresponds to the case where the tensile strength of each phase was set to infinity. Hence, no damage occurred during thermomechanical loading. More specifically, the numerical samples were submitted to a numerical cooling from T_g of glasses to 20°C in order to measure CTE. Then, tensile tests were performed to measure the apparent Young's modulus (paragraph C.I.1.2).

In the *'DEM damaged samples'* configuration, failure threshold of discrete elements were set to reproduce tensile strength of glasses. Indeed, the lower values of tensile strength shown in Tab. C.II.1 were chosen for both Cofer and BA glass. Thus, the tensile strength of Cofer glass and BA glass were set at 60 MPa and 45 MPa, respectively. Similarly to previous configuration, the apparent Young's modulus and CTE of thermally damaged samples were measured.

C.II.3.1 Model material with radial-propagated crack

In this paragraph, the results of cofer glass-alumina composite are discussed (Fig. C.II.7)

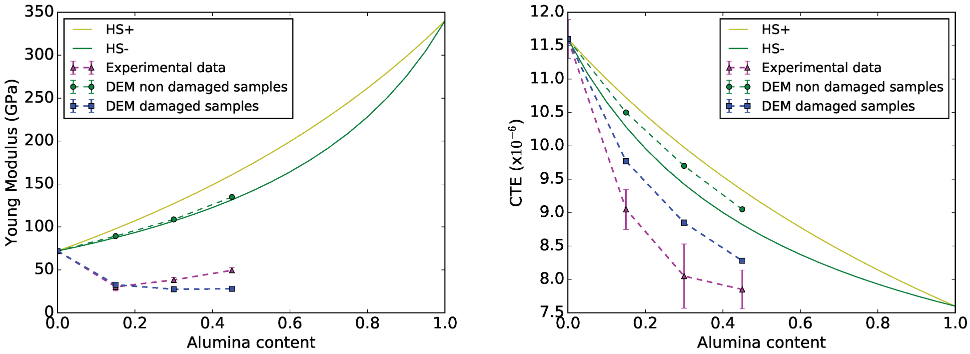

(a) Young's modulus (b) CTE

Fig. C.II.7: Comparison between DEM results, experimental data and HS model: apparent thermomechanical properties after cooling (Cofer glass-alumina)

Regarding the *'DEM non damaged sample'* configuration, the numerical curves are consistent with HS model for both CTE and Young's modulus. Moreover, in Fig. C.II.7(a), the numerical results of undamaged sample almost overlap the HS-curve, which could predict accurately elastic properties of undamaged material (paragraph A.I.3.3). These results allowed to confirmed the accuracy of numerical simulation in the case of undamaged two-phases material.

Regarding the *'DEM damaged samples'* configuration, both numerical and experimental curves are lower than HS- curves, for both CTE and Young's modulus. This observation is consistent with experimental results reported in literature: damages could decrease the Young's modulus and the CTE of material [TD03, SZCX10]. Fig. C.II.7(a) shows that the numerical value is close to experimental value of apparent Young's modulus for the case of 15% alumina. However, for higher volume fraction of alumina, the numerical values are lower than experimental values. In Fig. C.II.7(b), the numerical results of damaged samples has the same tendency with experimental curve of CTE: the reduction of apparent CTE increases as the volume fraction of alumina increases.

C.II.3.2 Model material with debonding at interfaces

In this paragraph, the results of BA glass-alumina composite are discussed (Fig. C.II.8).

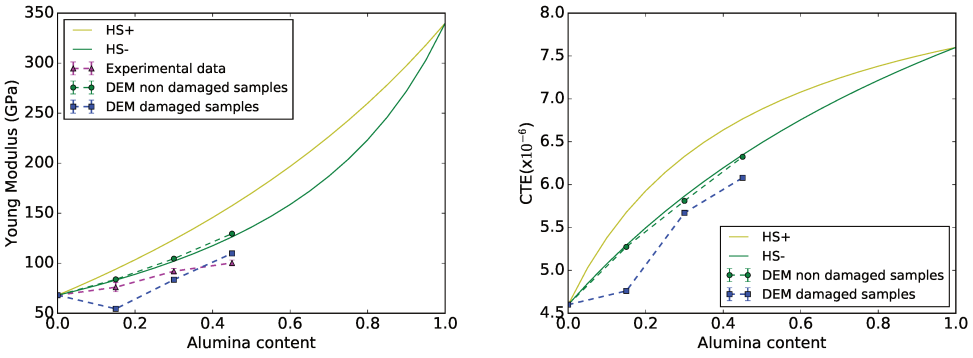

(a) Young's modulus

(b) CTE

Fig. C.II.8: BA glass-alumina: apparent thermomechanical properties after cooling

Considering the *'DEM non damaged samples'* configuration, numerical curves almost overlap the HS model for both Young's modulus and CTE. These results confirmed the accuracy of DEM simulation in case of undamaged material.

Considering the *'DEM damaged samples'* configuration, for both Young's modulus and CTE, the numerical results and experimental data have a similar tendency: thermomechanical properties at room temperature decrease in comparison with HS model, due to debonding phenomenon. As shown in Fig.

C.II.8(a), for the case of 15% alumina, the DEM results seems to overestimate the influence of debonding on the apparent Young's modulus. However, with higher volume fraction of alumina, the DEM values are quite close to the experimental values of the apparent Young's modulus of damaged samples. In Fig. C.II.8(b), numerical results show that there is a slight decrease of CTE due to debonding phenomenon. However, there is a lack of experimental curve since it is not available in the data of Tessier-Doyen [TD03]. Despite this lack of information, the obtained results allowed to quantify the occurrence of debonding phenomenon and it's effect on the apparent CTE.

C.II.4 Simulation of nonlinear behavior of model materials

In this section, DEM results of nonlinear tensile behavior due to thermal damages are discussed. In literature, several experimental researches reported that thermal damages could change the tensile behavior from linear to nonlinear: decrease of Young's modulus, decrease of stress-at-peak and increase of strain-to-rupture [Hug92, GK07, GB11, Bel15]. Since the influence of micro-crack is more important than that of debonding, hereafter, only results of Cofer glass-alumina is presented.

In this investigation, thermally damaged samples after cooling simulation were subjected to tensile test in order to observe stress-strain curve. Here, the average normal stress σ_{xx} of sample is computed as follows:

$$\sigma_{xx} = \frac{F_{xx}}{A} \tag{C.II.2}$$

where: F_{xx} is the applied tensile force and A is the area of cross section of sample.

In addition, the fracture threshold were set to reproduce tensile strength of Cofer glass, i.e. $\sigma_f = 60$ MPa. In other words, damages generated during cooling were allowed to propagate during these tensile test. This numerical process is comparable with experimental researches in [GK07, GB11]. Three volume fraction of alumina are considered: 15%, 30% and 45%.

Tensile simulations were carried out for damaged samples obtained at 3 instants of cooling: when T = T_g = 455°C, when T = 238°C and when T = 20°C. The purpose was to investigate the relationships between thermal damage levels and mechanical behavior of model material. The stress-strain curves of Cofer glass-alumina composite are shown in Fig. C.II.9.

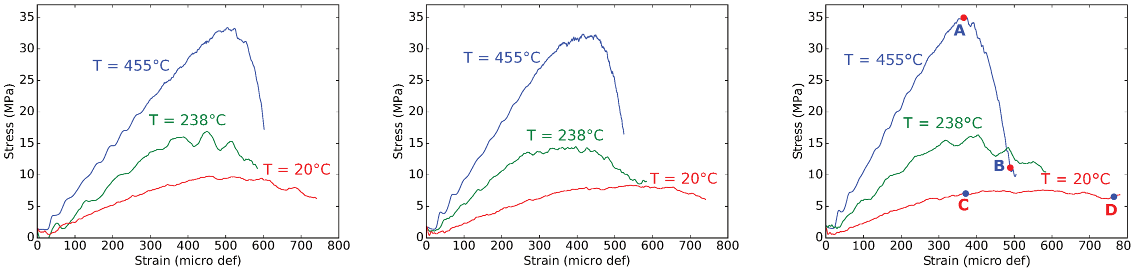

(a) 15% alumina (b) 30% alumina (c) 45% alumina

Fig. C.II.9: Development of nonlinear behavior during cooling

As shown in Fig. C.II.9, firstly, based on the slope of stress-strain curves before their peaks, the Young's modulus of material decreases as temperature decreases. Secondly, the stress-at-peak decreases as temperature decreases. These observations are reasonable because during cooling, micro-crack network extends as the temperature decreases and therefore, promotes the evolution of tensile behavior. Regarding the post-peak behavior, results of samples with 30% and 45% alumina are more relevant than that of sample with 15% alumina, in comparison with experimental observation: strain-to-rupture increases as temperature decreases. Finally, a gradual change from linear behavior (when T = 455°C) to nonlinear behavior (when T = 238°C and when T = 20°C) could be clearly observed. To be more detailed, tensile behavior of undamaged sample at T=T_g is not completely linear (Fig. C.II.9). However, as presented in part B, DEM is able to reproduce linear tensile behavior of fragile homogeneous material (Fig. B-B.I.13(a)). To explain this observation, the median cross section of sample that contain the direction of the tensile stress is plotted in order to highlight damage level of samples (Fig. C.II.10).

In Fig. C.II.10, median cross section of specific points during mechanical loading are showed, i.e. A, B, C, D points in Fig. C.II.9. As illustrated, for sample at T=455°C, after the peak, there is several macroscopic cracks normal to the applied tensile stress Fig. C.II.10(b). This explains a slight nonlinearity of tensile behavior of sample at T=455°C, which is initially undamaged. This observation suggests that the insertion of inclusions could slightly affect the tensile behavior. For sample at T=20°C, at the peak, there is high level of damages resulting from previous complete cooling and the current maximum mechanical loading (Fig. C.II.10(c)). Thus, damages progress between C and D points however, the difference is difficult to observe. This explains the flat curve of

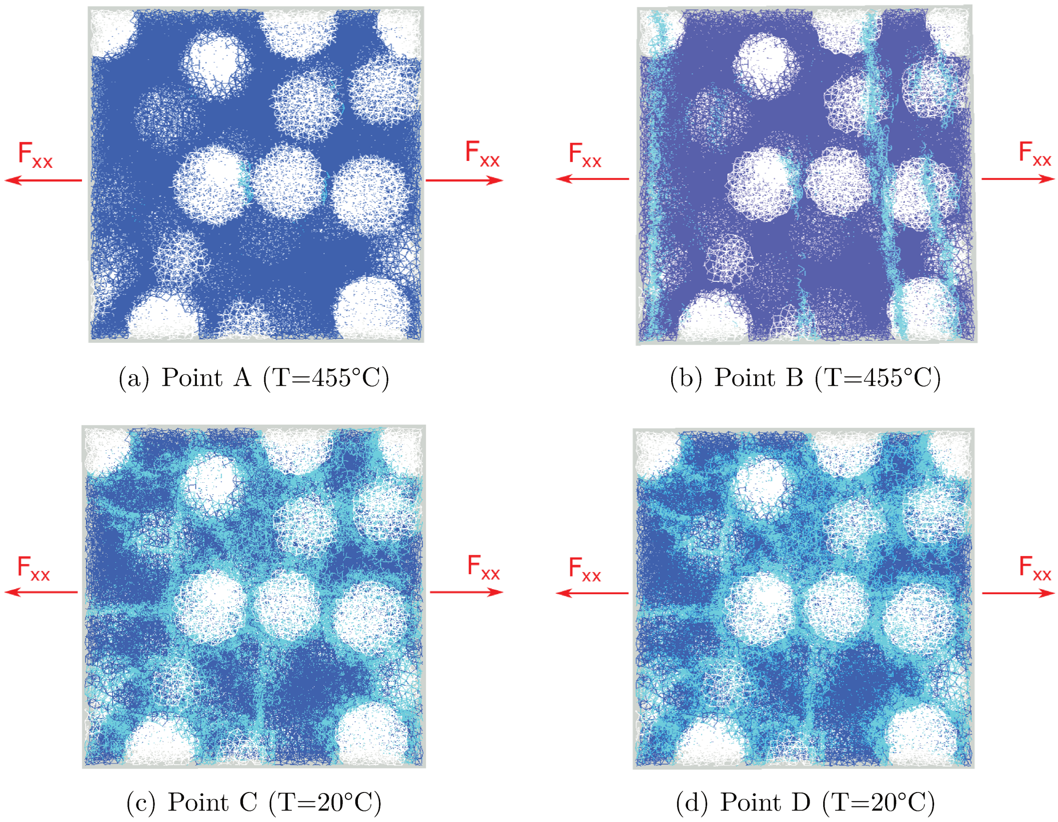

(a) Point A (T=455°C)

(b) Point B (T=455°C)

(c) Point C (T=20°C)

(d) Point D (T=20°C)

Fig. C.II.10: Median cross section that contains the direction of the tensile stress: view with bonds only (corresponds to specific points in Fig. C.II.9(c))

post-peak behavior that could be observed in the case of pre-cracked material.

Consequently, the obtained DEM results exhibits good agreements with experimental observations reported in literature [TD03, GK07, GB11]. Numerical investigation confirms the possibility to improve the thermal shock resistance of refractories by managing their microstructures: decreasing of Young's modulus and increasing of nonlinear behavior.

C.II.5 Conclusion

The main objective of this part was to model thermal damage phenomena and their influence on apparent behavior of model materials, i.e. Cofer glass-alumina and BA glass-alumina. In this part, the methodology to create *Statistical Volume Element* of heterogeneous material was described. The methodology to reproduce evolution of Young's modulus of model materials as function of temperature by using direct calibration method was also proposed. The accuracy of these methodologies were examined by confrontation of DEM results with experimental data in [TD03] and HS model. Indeed, *'DEM non damaged samples'* configuration globally matched with HS model, which could predict accurately thermomechanical properties of undamaged heterogeneous material. Moreover, ability of DEM to model thermal damage was examined. Damage morphologies obtained with DEM are comparable with experimental observations reported in literature, for both micro-cracking and debonding phenomena [TD03, GB11]. DEM results of influence of thermal damages show a good agreement with experimental data: the Young's modulus and the CTE of material decrease as the thermal damages develop within the material. The influence of thermal damages becomes more significant when the volume fraction of alumina increases. In addition, DEM results reported a gradual change of tensile behavior of model material from linear to nonlinear during cooling. In literature, up to now, there is a lack of numerical and analytical researches on this problematic. The obtained results in part C show that investigation of these phenomena by DEM is very promising. Although some improvements still needs to be carried out in the future works, the proposed numerical approach could help to improve the thermal shock resistance of refractories by better designing their microstructures.

General conclusion and perspectives

In many industries, refractories are subjected to severe working conditions: extra high temperature, brutal thermal shock, mechanical loading and corrosion. Among these conditions, the high local thermal stresses induced by thermal shocks can lead to critical failure for many industrial cases, even if the other required properties are satisfied. Therefore, thermal shock resistance is a key parameter of refractories to enhance their lifetime. For the last decades, experimental researches has proved that the thermal shock parameter is related to the local crack growth resistance mechanisms as well as the non-linearity of their tensile behavior. More specifically, in several cases, by introducing properly micro-damages within the microstructure of such materials, their thermal shock resistance could be tuned positively: decreasing of Young modulus, decreasing of CTE, decreasing of strength, increasing of strain-to-rupture and increasing of fracture energy. However, up to now, the method of applying these phenomena to improve the thermal shock resistance of refractories has not been fully understood and is not predictable. In this context, the numerical approaches could help and give insights for experimental researches.

The present thesis aimed at investigating the relationships which exist between the microstructure of refractories and their thermomechanical properties by developing an efficient and reliable modeling platform. For this purpose, the developed modeling platform must be able to reproduce complex morphology of micro-crack within continuous media in order to predict the apparent properties of damaged material. Generally, in thermomechanical area, numerical methods can be classified into continuous methods and discrete methods. Despite significant successes of several continuous methods, e.g. XFEM (eXtended Finite Element Method), PFM (Phase Field Method), their applications for complex crack phenomena still, up to now, remain problematic. To overcome limitations of continuous methods for the present research, the discrete methods is a good candidate thanks to the ability to describe discontinuities. Moreover, in this class of method, initiation of crack could be simply handled by breaking interaction between elements. In the present research, the variant of the Discrete Element Method (DEM) developed by André *et al.* [ACI15, JATI15] and the associated DEM modeling platform *GranOO* were chosen.

The *Granular Object Oriented Workbench (GranOO)* has been developed since 2010 by the collaboration of 3 French laboratories. This platform of discrete element modeling is based on explicit dynamic resolution algorithm to perform a wide range of numerical experiments. In this modeling platform, the Cohesive Beam Model (CBM) has been implemented in order to model continuous media.

However, similarly to other discrete methods which were initially developed for granular media, the CBM faces two main challenges to model continuous media. Firstly, the calibration of microscopic parameter is still a major challenge for DEM until present due to the lack of research dedicated for this problematic. Indeed, the calibration process is very tedious and time-consuming, however it is inevitable each time the modeled material is changed. Secondly, stress computations of DEM applied to continuous media has not been fully developed.

To overcome the first challenge, a *direct calibration method* has been developed in the present research in order to facilitate the DEM simulation. More specifically, novel macro-to-micro relationships were established to enable direct deduction of local input parameters from thermomechanical properties of considered material. This method does not depend on sample shape, discrete element number, loading conditions and thus, can be considered as constitutive law of numerical material. This proposed direct calibration method was validated through its application to classical mechanical simulation tests: uniaxial tensile test, hydrostatic compression test, Brazilian test and torsion test. This allows to skip the classical trial-and-error calibration method, which is very complicated and time consuming.

The second challenge of DEM is related to the lack of stress tensor consideration because, the DEM is force-displacement method and it was initially applied for granular media. To deal with this issue, the virial stress concept has been developed in *GranOO* platform since 2013 [JAD+13, AJI+13]. In the present research, the virial stress concept was studied and improved in order to enable quantitative simulation of complex damage phenomena within continuous media. Firstly, the dependence of accuracy on the computation range (neighbor levels) was investigated by comparison between virial stress tensor and theoretical computation. This comparison demonstrated that *'neighbor level 2'* could ensure a good compromise between accuracy and computational time. Secondly, two different local fracture criteria were examined: Rankine criterion and Hydrostatic criterion. The latter criterion give more adequate post-peak behavior for brittle material: a brutal drop towards 0 of Young's modulus after macroscopic fracture. Therefore, Hydrostatic criterion was qualified for the present study. Finally, the proposed configuration of virial stress concept was validated through different loading conditions: Brazilian test and torsion test. The obtained results demonstrated that virial stress could reproduce adequate stress states and crack morphologies for the considered numerical tests.

In term of application, the main objective of the development of *GranOO* modeling platform was to model the thermal damages in some simplified model materials and to examine their effect on apparent properties of damaged materials. In the present research, 2 model materials developed by Tessier-Doyen *et al.* were used, i.e. Cofer glass alumina and BA-glass alumina composites. In the first step, a single-inclusion configuration was used for cooling simulation. More specifically, the comparison with FEM and Lauke's analytical approach demonstrated the accuracy of DEM and virial stress concept to simulate thermal stress and the associated damage phenomena. In the second step, to model heterogeneous materials, *Statistical Volume Elements* were generated by using the methodology proposed by André *et al.* [ALTDH17]. This methodology consists of distributing randomly a predefined volume fraction of spherical inclusions within a cubic discrete domain. Thanks to the proposed *direct calibration method*, the modulation of local parameters allows to reproduce the evolution of Young's modulus of these heterogeneous composites as a function of temperature. The obtained results were then validated by confrontation with experimental data and HS model. Indeed, DEM results of undamaged configuration matched with HS model, which could predict accurately thermomechanical properties of undamaged heterogeneous composites. Regarding thermal damages simulation, damage morphologies obtained with DEM are consistent with experimental observations, for both micro-cracking and debonding phenomena. Quantitatively, thermal damages modeled by DEM exhibits a good agreement with experimental data: the Young's modulus and the CTE of model materials decrease as the thermal damages develop within their microstructure. The influence of thermal damages becomes more significant when the volume fraction of alumina increases. Finally, DEM results allowed to reproduce the change in tensile behavior of model material from linear to non linear due to micro-cracking. These important results demonstrated the ability of the proposed DEM approach to take into account the effect of microscopic damages on macroscopic properties in a multi-scale approach.

The present research should be considered as a first step of a long term objective: development of a reliable modeling platform to give insights for experimental approach in order to enhance thermal shock resistance of industrial refractories. Consequently, the perspectives of this work could be numerous. From technical point of view, 3 investigations should be considered: voids within discrete domain in the current *GranOO* version, necessity to increase discretization level of discrete domain and potential interest to implement periodic boundary conditions.

Firstly, artificial voids between spherical discrete elements could be removed thanks to Voronoi-based discrete elements in the new version of *GranOO*. Secondly, the increase of discretization level could be managed thanks to increase of computer performance or by application of suitable computational strategy. This strategy could be conducted by modulation of discrete element size (using small size of discrete element in critical zone and coupling with classical FEM computation in other areas). This allows to discretize some specific zones of discrete domain with higher element number, e.g. the interfacial zone in heterogeneous materials. Thirdly, the periodic boundary conditions has demonstrated its efficiency in FEM to study heterogeneous material. Hence, it is perhaps interesting to implement the periodic boundary conditions in *GranOO* and examine its impacts.

In the present research, the proposed DEM approach does not take into account some specific phenomena: surface energy consumed during crack propagation and energy dissipation due to friction mechanism between crack lips (between discrete element in DEM). The role of these phenomena should be taken into account by improving the current DEM approach.

Appendix: Data analysis by least square method

In order to define the analytical expressions of micro-to-macro relationships in Cohesive Beam Model, data of macroscopic responses need to be generated from a series of simulations with reasonable ranges of microscopic parameters. In this study, the relationships between microscopic and macroscopic elastic parameters of CBM were deduced from 8,000 simulations of uniaxial tensile tests, whose the configuration is described in section B-B.I.4.3.a. Hence, the nonlinear least squares method was used to analyze the data issued from tensile test simulations. The nonlinear least squares method is the form of least squares analysis, used to fit a set of m observations with a non-linear function including n unknown coefficients ($m > n$). In order to obtain an approximate solution, the coefficients of the non-linear functions are refined by successive iterations.

Let us consider, for example, a set of m data points, (x_1, y_1) , (x_2, y_2),..., (x_m, y_m), and a model function $y = f(x, \boldsymbol{\beta})$, that depends on variable x and n coefficients, $\boldsymbol{\beta} = (\beta_1, \beta_2, ..., \beta_n)$, with $m \geq n$. The non-linear least squares method allows to find the vector $\boldsymbol{\beta}$ of coefficients such that the model function fits best the given data in the least square sense. In other words, the sum of squares

$$S = \sum_{i=1}^{m} r^2$$

is minimized. The residuals r_i are given by :

$$r_i = y_i - f(x_i, \boldsymbol{\beta}) \quad \text{for} \quad (i = 1, 2, ..., m)$$

The minimum value of S occurs when the gradient is zero. Since the model contains n coefficients, there are n gradient equation:

$$\frac{\partial S}{\partial \beta_i} = 2\sum_i r_i \frac{\partial r_i}{\partial \beta_i} = 0 \quad (j = 1, 2, ..., n)$$

In a nonlinear system, the derivatives $\frac{\partial r_i}{\partial \beta_j}$ are functions of both the independent variable x and the vector $\boldsymbol{\beta}$ of coefficients. Thus, these gradient equations do not have a closed solution. Consequently, initial values are chosen as solution for the coefficients. Then, the coefficients are refined iteratively, that is, the values are obtained by successive approximation.

In the present study, the routine named `optimize.curve_fit`, which is based on the Levenberg-Marquardt algorithm [Mor78, Lev44], is selected to find the fitting solutions. This implementation, included by Python library, is very robust and has strong convergence properties. By analyzing the data extracted from 8,000 simulations of uniaxial tensile tests, the fitting functions that best describe the macro-to-micro relationships are determined.

Bibliography

[ACI15] D. André, J-L. Charles, and I. Iordanoff. *3D Discrete Element Workbench for Highly Dynamic Thermo-mechanical Analysis: GranOO*. Wiley, 2015. 29, 34, 35, 50, 51, 141

[AIlCN12] Damien André, Ivan Iordanoff, Jean luc Charles, and Jérome Néauport. Discrete element method to simulate continuous material by using the cohesive beam model. *Computer Methods in Applied Mechanics and Engineering*, 213–216(0):113 – 125, 2012. vi, 34, 46, 51, 52, 54, 56

[AJI$^+$13] Damien André, Mohamed Jebahi, Ivan Iordanoff, Jean luc Charles, and Jérôme Néauport. Using the discrete element method to simulate brittle fracture in the indentation of a silica glass with a blunt indenter. *Computer Methods in Applied Mechanics and Engineering*, 265(0):136 – 147, 2013. 29, 34, 54, 60, 64, 142

[ALS81] Thomas E Adams, Dennis J Landini, and Clifford A Schumacher. Micro- and macrocrack growth in alumina refractories. *American Ceramic Society Bulletin*, 60(7):730–5, 1981. 9

[ALTDH17] Damien André, Bertrand Levraut, Nicolas Tessier-Doyen, and Marc Huger. A discrete element thermo-mechanical modelling of diffuse damage induced by thermal expansion mismatch of two-phase materials. *Computer Methods in Applied Mechanics and Engineering*, 318:898–916, 2017. 54, 57, 58, 114, 143

[And12] D. André. *Modélisation par éléments discrets des phases d'ébauchage et de doucissage de la silice*. PhD thesis, Université Bordeaux 1, 2012. 41, 58, 73

[ARRW02] Cemail Aksel, Brian Rand, Frank L Riley, and Paul D Warren. Mechanical properties of magnesia-spinel composites. *Journal of the European Ceramic Society*, 22(5):745–754, 2002. 12

[AW03] Cemail Aksel and Paul D Warren. Thermal shock parameters [r, r$'''$ and r$''''$] of magnesia–spinel composites. *Journal of the European Ceramic Society*, 23(2):301–308, 2003. 12

[Bax04] S. Baxendale. *Testing of refractory materials*. CRC Press, 2004. 7

[BB99] Ted Belytschko and Tom Black. Elastic crack growth in finite elements with minimal remeshing. *International journal for numerical methods in engineering*, 45(5):601–620, 1999. 27

[BDP^{+}17] Y Belrhiti, JC Dupre, O Pop, A Germaneau, P Doumalin, M Huger, and T Chotard. Combination of brazilian test and digital image correlation for mechanical characterization of refractory materials. *Journal of the European Ceramic Society*, 37(5):2285–2293, 2017. 87

[Bel15] Younès Belrhiti. *Etude de matériaux réfractaires à comportement mécanique non linéaire par mesure de champs de déformations*. PhD thesis, 2015. Thèse de doctorat dirigée par Huger, Marc et Chotard, Thierry Matériaux céramiques et traitements de surface Limoges 2015. 10, 136

[Ber16] Levraut Bertrand. *Thermo-mechanical modeling of heterogeneous materials - Towards the development of refractories improvement numerical tools*. PhD thesis, Université de Limoges, 2016. 19, 78

[BFJ^{+}09] A Bobet, A Fakhimi, S Johnson, J Morris, F Tonon, and M Ronald Yeung. Numerical models in discontinuous media: review of advances for rock mechanics applications. *Journal of Geotechnical and Geoenvironmental Engineering*, 135(11):1547–1561, 2009. 29

[BFM08] Blaise Bourdin, Gilles A Francfort, and Jean-Jacques Marigo. The variational approach to fracture. *Journal of elasticity*, 91(1-3):5–148, 2008. 28

[BHLV14] Michael J Borden, Thomas JR Hughes, Chad M Landis, and Clemens V Verhoosel. A higher-order phase-field model for brittle fracture: Formulation and analysis within the isogeometric analysis framework. *Computer Methods in Applied Mechanics and Engineering*, 273:100–118, 2014. 28

[BLR11] Blaise Bourdin, Christopher J Larsen, and Casey L Richardson. A time-discrete model for dynamic fracture based on crack regularization. *International journal of fracture*, 168(2):133–143, 2011. 28

[Bra81] RC Bradt. Problems and possibilities with cracks in ceramics. In *Proc. 11 th International Conf. on Science of Ceramics held at Stenungsund, Sweden, June 14-17, 1981. Edited by R. Carlsson and S. Karlsson. Swedish Ceram. Soc., Gothenburg, Sweden, 1981.*, page 349, 1981. 9

[BVS$^+$12] Michael J Borden, Clemens V Verhoosel, Michael A Scott, Thomas JR Hughes, and Chad M Landis. A phase-field description of dynamic brittle fracture. *Computer Methods in Applied Mechanics and Engineering*, 217:77–95, 2012. 28

[CLPG18] Rémi CURTI, Philippe Lorong, guillaume POT, and Stéphane Girardon. How to model orthotropic materials by the Discrete Element Method (DEM): random sphere packing or regular cubic arrangement? *Computational Particle Mechanics*, page 24, 2018. 30

[CLTC05] James K Carson, Simon J Lovatt, David J Tanner, and Andrew C Cleland. Thermal conductivity bounds for isotropic, porous materials. *International Journal of Heat and Mass Transfer*, 48(11):2150–2158, 2005. 20

[CMS07] Net al Cho, CD Martin, and DC Sego. A clumped particle model for rock. *International Journal of Rock Mechanics and Mining Sciences*, 44(7):997–1010, 2007. 29, 50

[CS79] P. A. Cundall and O. D. L. Strack. A discrete numerical model for granular assemblies. *Geotechnique*, 29:47–65, 1979. 31, 49

[Cun71] Peter A Cundall. A computer model for simulating progressive, large-scale movement in blocky rock system. In *Proceedings of the International Symposium on Rock Mechanics, 1971*, 1971. 29, 31

[DKR02] G. A. D'Addetta, F. Kun, and E. Ramm. On the application of a discrete model to the fracture process of cohesive granular materials. *Granular Matter*, 4(2):77–90, 2002. 51

[DR06] G. A. D'Addetta and E. Ramm. A microstructure-based simulation environment on the basis of an interface enhanced particle model. *Granular Matter*, 8(3):159–174, 2006. 51

[Ebe10] D. Eberly. *Game physics*. Elsevier, Morgan Kaufmann, second edition edition, 2010. 39

[EW12] Nazife Erarslan and David John Williams. Experimental, numerical and analytical studies on tensile strength of rocks. *International Journal of Rock Mechanics and Mining Sciences*, 49:21 – 30, 2012. 88, 89

[Fai64] C. Fairhurst. On the validity of the 'brazilian' test for brittle materials. *International Journal of Rock Mechanics and Mining Sciences & Geomechanics Abstracts*, 1(4):535 – 546, 1964. 88

[FGE07] Florian Fleissner, Timo Gaugele, and Peter Eberhard. Applications of the discrete element method in mechanical engineering. *Multibody System Dynamics*, 18(1):81, Jun 2007. vi, 32, 33

[Fin70] JL Finney. Random packings and the structure of simple liquids. i. the geometry of random close packing. *Proceedings of the Royal Society of London. A. Mathematical and Physical Sciences*, 319(1539):479–493, 1970. 46

[Flo18] LA Florio. Development of novel heat conduction interaction model for solid body thermal contact in cfd based particle flow simulations. *Chemical Engineering Science*, 192:448–466, 2018. 58

[FM98] Gilles A Francfort and J-J Marigo. Revisiting brittle fracture as an energy minimization problem. *Journal of the Mechanics and Physics of Solids*, 46(8):1319–1342, 1998. 28

[FV07] Ali Fakhimi and Tomas Villegas. Application of dimensional analysis in calibration of a discrete element model for rock deformation and fracture. *Rock Mechanics and Rock Engineering*, 40(2):193, 2007. 69

[GB11] Renaud Grasset-Bourdel. *Structure/property relations of magnesia-spinel refractories: experimental determination and simulation*. PhD thesis, Limoges, 2011. v, 10, 12, 13, 14, 136, 138, 139

[GF74] Keishi Gotoh and J. L. Finney. Statistical geometrical approach to random packing density of equal spheres. *Nature*, 252:202–205, 1974. 46, 48

[GGS78] G.A. Gogotsi, Ya.L. Groushevsky, and K.K. Strelov. The significance of non-elastic deformation in the fracture of heterogeneous ceramic materials. *Ceramurgia International*, 4(3):113 – 118, 1978. 9

[GJ16] Vijay Goyal and Rafael Jorge. Micro-scale crack propagation using the extended finite element method. In *57th AIAA/ASCE/AHS/ASC Structures, Structural Dynamics, and Materials Conference*, page 0729, 2016. vi, 27, 28

[GK07] M Ghassemi Kakroudi. *Comportement thermomécanique en traction de bétons réfractaires: influence de la nature des agrégats et de l'histoire thermique*. PhD thesis, Ph. D. University of Limoges, France, 2007. v, vii, 10, 11, 12, 15, 16, 17, 108, 136, 138

[Gog93] G. A. Gogotsi. *The Significance of Non-Elastic Deformation in the Thermal Shock Fracture of Heterogeneous Ceramic Materials*, pages 279–291. Springer Netherlands, Dordrecht, 1993. 9

[HAD$^+$17] Cédric Hubert, Damien André, L Dubar, I Iordanoff, and JL Charles. Simulation of continuum electrical conduction and joule heating using dem domains. *International Journal for Numerical Methods in Engineering*, 110(9):862–877, 2017. 34

[Har81] A.S. Hardy. *Elements of Quaternions*. Ginn, Heath, & Company, 1881. 39

[Has62] Zvi Hashin. The elastic moduli of heterogeneous materials. *Journal of Applied Mechanics*, 29(1):143–150, 1962. 19

[Has63] DPH Hasselman. Elastic energy at fracture and surface energy as design criteria for thermal shock. *Journal of the American Ceramic Society*, 46(11):535–540, 1963. 7, 8

[Has69] DPH Hasselman. Unified theory of thermal shock fracture initiation and crack propagation in brittle ceramics. *Journal of the American Ceramic society*, 52(11):600–604, 1969. 7, 8

[HDD04] Sébastien Hentz, Frédéric V Donzé, and Laurent Daudeville. Discrete element modelling of concrete submitted to dynamic loading at high strain rates. *Computers & structures*, 82(29-30):2509–2524, 2004. 29

[Her88] H. J. Herrmann. Proceedings of the nato advanced study institute, cargèse, corsica, france, 18-31 july, 1988. In *Random Fluctuations and Pattern Growth: Experiments and Models Random Fluctuations and Pattern Growth: Experiments and Models*, volume 157 of *NATO Science Series E*, pages 149–160. Stanley, Harry Eugene; Ostrowsky, N., 1988. 51

[HGF14] H Haddad, M Guessasma, and J Fortin. Heat transfer by conduction using dem–fem coupling method. *Computational Materials Science*, 81:339–347, 2014. 58

[HJ77] Heinz Hübner and W Jillek. Sub-critical crack extension and crack resistance in polycrystalline alumina. *Journal of Materials Science*, 12(1):117–125, 1977. 9

[HLG$^+$15] Hamza Haddad, W Leclerc, M Guessasma, C Pélegris, N Ferguen, and E Bellenger. Application of dem to predict the elastic behavior of particulate composite materials. *Granular Matter*, 17(4):459–473, 2015. 60

[HNKK17] Zoltán Halász, Akio Nakahara, So Kitsunezaki, and Ferenc Kun. Effect of disorder on shrinkage-induced fragmentation of a thin brittle layer. *Physical Review E*, 96(3):033006, 2017. 50

[Hon59] G Hondros. The evaluation of poisson's ratio and the modulus of materials of low tensile resistance by the brazilian (indirect tensile) test with particular reference to concrete. *Australian J. Appl. Sci.*, 10(3):243–268, 1959. 89

[Hre41] Alexander Hrennikoff. Solution of problems of elasticity by the framework method. *J. appl. Mech.*, 1941. 30

[HS63] Zvi Hashin and Shmuel Shtrikman. A variational approach to the theory of the elastic behaviour of multiphase materials. *Journal of the Mechanics and Physics of Solids*, 11(2):127–140, 1963. 19

[Hug92] Marc Huger. *Oxydation et endommagement d'origine thermique, evalues par techniques ultrasonores a haute temperature, de composites sic/c/sic non proteges*. PhD thesis, 1992. Thèse de doctorat dirigée par Gault, Christian Sciences appliquées Limoges 1992. 10, 136

[HWP17] Zhenyu Han, Dion Weatherley, and Ruslan Puscasu. A relationship between tensile strength and loading stress governing the onset of mode i crack propagation obtained via numerical investigations using a bonded particle model. *International Journal for Numerical and Analytical Methods in Geomechanics*, 41(18):1979–1991, 2017. 69

[ID03] A. Ibrahimbegovic and A. Delaplace. Microscale and mesoscale discrete models for dynamic fracture of structures built of brittle material. *Computers & Structures*, 81(21):1255–1265, 2003. 31

[IK54] GR Irwin and JA Kies. Welding research supplement 19. 1954. 9

[Inc12] Itasca Consulting Group Inc. Particle flow code in 2 dimensions. 2012. 50

[Inc18] Itasca Consulting Group Inc. PFC 6.0 manual documentation. 2018. vi, 49

[JAD$^+$13] Mohamed Jebahi, Damien André, Frédéric Dau, Jean luc Charles, and Ivan Iordanoff. Simulation of vickers indentation of silica glass. *Journal of Non-Crystalline Solids*, 378:15 – 24, 2013. 142

[JATI15] Mohamed Jebahi, Damien André, Inigo Terreros, and Ivan Iordanoff. *Discrete element method to model 3D continuous materials*. John Wiley & Sons, 2015. vi, 29, 30, 33, 34, 35, 38, 40, 41, 46, 56, 58, 59, 60, 61, 64, 141

[JDIG17] Mohamed Jebahi, Frédéric Dau, Ivan Iordanoff, and Jean-Pierre Guin. Virial stress–based model to simulate the silica glass densification with the discrete element method. *International Journal for Numerical Methods in Engineering*, 112(13):1909–1925, 2017. 60

[Jeb13] Mohamed Jebahi. *Discrete-continuum coupling method for simulation of laser-inducced damage in silica glass*. PhD thesis, Bordeaux 1, 2013. 25

[JLZ$^+$18] Shengqiang Jiang, Xu Li, Li Zhang, Yuanqiang Tan, Ruitao Peng, and Rui Chen. Discrete element simulation of sic ceramic containing a single pre-existing flaw under uniaxial compression. *Ceramics International*, 44(3):3261–3276, 2018. 29

[Jol06] Yoann Joliff. *Etude expérimentale et numérique des propriétés d'élasticité de matériaux modèles hétérogènes*. PhD thesis, Limoges, 2006. viii, 6, 11, 18, 20, 22, 37, 109, 110, 111, 128, 129, 133

[KD08] Jan Kozicki and Frederic V Donze. A new open-source software developed for numerical simulations using discrete modeling methods. *Computer Methods in Applied Mechanics and Engineering*, 197(49-50):4429–4443, 2008. 50

[KH96] F. Kun and H. J. Herrmann. A study of fragmentation processes using a discrete element method. *Computer Methods in Applied Mechanics and Engineering*, 138(1-4):3–18, 1996. 51

[Kin55] W David Kingery. Factors affecting thermal stress resistance of ceramic materials. *Journal of the American Ceramic Society*, 38(1):3–15, 1955. 10

[KM10] Charlotte Kuhn and Ralf Müller. A continuum phase field model for fracture. *Engineering Fracture Mechanics*, 77(18):3625–3634, 2010. 28

[LCH74] DR Larson, JA Coppola, and DPH Hasselman. Fracture toughness and spalling behavior of high-al2o3 refractories. *Journal of the American Ceramic Society*, 57(10):417–421, 1974. 8

[Lev44] Kenneth Levenberg. A method for the solution of certain non-linear problems in least squares. *Quarterly of applied mathematics*, 2(2):164–168, 1944. 71, 146

[LG14] A Lisjak and G Grasselli. A review of discrete modeling techniques for fracturing processes in discontinuous rock masses. *Journal of Rock Mechanics and Geotechnical Engineering*, 6(4):301–314, 2014. 29

[LHG17] W. Leclerc, H. Haddad, and M. Guessasma. On the suitability of a discrete element method to simulate cracks initiation and propagation in heterogeneous media. *International Journal of Solids and Structures*, 108:98 – 114, 2017. 50

[LSB00] B Lauke, T Schüller, and W Beckert. Calculation of adhesion strength at the interface of a coated particle embedded within matrix under multiaxial load. *Computational materials science*, 18(3-4):362–380, 2000. 96, 100, 102, 104

[LZG+18] Guangzhong Liu, Dai Zhou, Jiamin Guo, Yan Bao, Zhaolong Han, and Jiabao Lu. Numerical simulation of fatigue crack propagation interacting with micro-defects using multiscale xfem. *International Journal of Fatigue*, 109:70 – 82, 2018. 27

[McK96] JC McKim. Programming by contract. *Computer*, 29(3):109–111, 1996. 41

[MDB99] Nicolas Moës, John Dolbow, and Ted Belytschko. A finite element method for crack growth without remeshing. *International journal for numerical methods in engineering*, 46(1):131–150, 1999. 27

[MHSA15] Christian Miehe, M Hofacker, L-M Schänzel, and Fadi Aldakheel. Phase field modeling of fracture in multi-physics problems. part ii. coupled brittle-to-ductile failure criteria and crack propagation in thermo-elastic–plastic solids. *Computer Methods in Applied Mechanics and Engineering*, 294:486–522, 2015. 28

[Mor78] Jorge J Moré. The levenberg-marquardt algorithm: implementation and theory. In *Numerical analysis*, pages 105–116. Springer, 1978. 71, 146

[MS88] D.B. Marshall and M.V. Swain. *Crack resistance curves in magnesia-partially-stabilized zirconia*, pages 399–407. 1988. 9

[MSU15] Christian Miehe, Lisa-Marie Schaenzel, and Heike Ulmer. Phase field modeling of fracture in multi-physics problems. part i. balance of crack surface and failure criteria for brittle crack propagation in thermo-elastic solids. *Computer Methods in Applied Mechanics and Engineering*, 294:449–485, 2015. 28

[MWH10] Christian Miehe, Fabian Welschinger, and Martina Hofacker. Thermodynamically consistent phase-field models of fracture: Variational principles and multi-field fe implementations. *International Journal for Numerical Methods in Engineering*, 83(10):1273–1311, 2010. 28

[NAH19] Truong-Thi Nguyen, Damien André, and Marc Huger. Analytic laws for direct calibration of discrete element modeling of brittle elastic media using cohesive beam model. *Computational Particle Mechanics*, Mar 2019. 94

[Nak65] Junn Nakayama. Direct measurement of fracture energies of brittle heterogeneous materials. *Journal of the American Ceramic Society*, 48(11):583–587, 1965. 8

[NBR$^+$17] Thanh-Tung Nguyen, José Bolivar, Julien Réthoré, Marie-Christine Baietto, and Marion Fregonese. A phase field method for modeling stress corrosion crack propagation in a nickel base alloy. *International Journal of Solids and Structures*, 112:65–82, 2017. vi, 28, 29

[Ngu15] Thanh Tung Nguyen. *Modeling of complex microcracking in cement based materials by combining numerical simulations based on a phase-field method and experimental 3D imaging*. PhD thesis, Paris Est, 2015. v, 28

[NI15] Mijo Nikolic and Adnan Ibrahimbegovic. Rock mechanics model capable of representing initial heterogeneities and full set of 3d failure mechanisms. *Computer Methods in Applied Mechanics and Engineering*, 290:209–227, 2015. 29

[NKIM18] Mijo Nikolic, Emir Karavelić, Adnan Ibrahimbegovic, and Predrag Miščević. Lattice element models and their peculiarities. *Archives of Computational Methods in Engineering*, 25:753–784, 07 2018. 31

[NT18] Michał Nitka and Jacek Tejchman. A three-dimensional meso-scale approach to concrete fracture based on combined dem with x-ray μct images. *Cement and Concrete Research*, 107:11–29, 2018. 29

[PB99] E. P. (Egor Paul) Popov and (author.) Balan, Toader A. *Engineering mechanics of solids*. Upper Saddle River, N.J. : Prentice Hall, second edition edition, 1999. 8

[PC04] D.O. Potyondy and P. A. Cundall. A bonded-particle model for rock. *International Journal of Rock Mechanics and Mining Sciences*, 41(8):1329–1364, 2004. Rock Mechanics Results from the Underground Research Laboratory, Canada. 33, 49

[PL01] T. Pöschel and S. Luding. *Granular Gases*, volume Vol. 564 of *Lecture Notes in Physics*. Pöschel, Thorsten; Luding, Stefan, 2001. 46

[PM10] Kim Pham and Jean-Jacques Marigo. The variational approach to damage: I. the foundations. *Academie des Sciences. Comptes Rendus. Mecanique*, 338(4):191–198, 2010. 28

[PS05] T. Pöschel and T. Schwager. *Computational granular dynamics.* Springer, 2005. 39

[RAHA13] Mahmood Reza Rahimi, Nader Azizi, Seyyed Hossein Hosseini, and Goodarz Ahmadi. Cfd study of hydrodynamics behavior of a vibrating fluidized bed using kinetic-frictional stress model of granular flow. *Korean Journal of Chemical Engineering*, 30(3):761–770, 2013. 60

[Rit88] RO Ritchie. Mechanisms of fatigue crack propagation in metals, ceramics and composites: role of crack tip shielding. *Materials Science and Engineering: A*, 103(1):15–28, 1988. 9

[RLK19] Mohammad Rezanezhad, Seyed Ahmad Lajevardi, and Sadegh Karimpouli. Effects of pore-crack relative location on crack propagation in porous media using xfem method. *Theoretical and Applied Fracture Mechanics*, 103:102241, 2019. 27

[RMJ04] E Rougier, A Munjiza, and NWM John. Numerical comparison of some explicit time integration schemes used in dem, fem/dem and molecular dynamics. *International journal for numerical methods in engineering*, 61(6):856–879, 2004. 39

[Roe56] F. C. Roesler. Brittle fractures near equilibrium. *Proceedings of the Physical Society. Section B*, 69(10):981, 1956. 34, 59

[ROLK11] Jerzy Rojek, Eugenio Onate, Carlos Labra, and Hubert Kargl. Discrete element simulation of rock cutting. *International Journal of Rock Mechanics and Mining Sciences*, 48(6):996–1010, 2011. 69

[Roo06] Mohsen Roosefid. *Etude du comportement thermomécanique de deux bétons réfractaires silico-alumineux: applications à une poche d'aciérie*. PhD thesis, Grenoble INPG, 2006. 15

[SAKK07] E Sarris, Z Agioutantis, K Kaklis, and SK Kourkoulis. Numerical simulation of the cracked brazilian disc under diametral compression. In *Bifurcations, Instabilities, Degradation in Geomechanics*, pages 403–430. Springer, 2007. 89

[Sch97] Joachim Schöberl. Netgen an advancing front 2D/3D-mesh generator based on abstract rules. *Computing and visualization in science*, 1(1):41–52, 1997. 98

[Sel61] Jorgen Selsing. Internal stresses in ceramics. *Journal of the American Ceramic Society*, 44(8):419–419, 1961. 129, 130, 133

[SG96] E. Schlangen and E.J. Garboczi. New method for simulating fracture using an elastically uniform random geometry lattice. *International Journal of Engineering Science*, 34(10):1131 – 1144, 1996. vi, 31, 51

[SG97] E. Schlangen and E.J. Garboczi. Fracture simulations of concrete using lattice models: Computational aspects. *Engineering Fracture Mechanics*, 57(2):319 – 332, 1997. 30, 31

[SMAA09] Miloud Souiyah, Andanastuti Muchtar, Abdulnaser Alshoaibi, and AK Ariffin. Finite element analysis of the crack propagation for solid materials. *American Journal of Applied Sciences*, 6(7):1396, 2009. v, 27

[Str88] Gilbert Strang. *Linear algebra and its applications*. Harcourt, Brace, Jovanovich, Publishers, 3rd ed edition, 1988. 64

[SvM92a] E. Schlangen and J. G. M. van Mier. Simple lattice model for numerical simulation of fracture of concrete materials and structures. *Materials and Structures*, 25(9):534–542, 1992. 51

[SVM92b] E Schlangen and JGM Van Mier. Simple lattice model for numerical simulation of fracture of concrete materials and structures. *Materials and Structures*, 25(9):534–542, 1992. 51

[SZCX10] Zhong-he Shui, Rui Zhang, Wei Chen, and Dong-xing Xuan. Effects of mineral admixtures on the thermal expansion properties of hardened cement paste. *Construction and Building Materials*, 24(9):1761–1767, 2010. 135

[TD03] Nicolas Tessier-Doyen. *Etude expérimentale et numérique du comportement thermomécanique de matériaux réfractaires modèles.* PhD thesis, Université de Limoges, 2003. v, viii, ix, 6, 11, 18, 19, 20, 21, 22, 23, 24, 37, 78, 95, 96, 109, 110, 111, 113, 117, 119, 127, 129, 130, 133, 135, 136, 138, 139

[TIC13] Inigo Terreros, Ivan Iordanoff, and Jean-Luc Charles. Simulation of continuum heat conduction using dem domains. *Computational Materials Science*, 69:46–52, 2013. 34

[Tim82] S. P. Timoshenko. *History of strength of materials: with a brief account of the history of theory of elasticity and theory of structures.* Dover, New York, NY, 1982. 52

[TSVA15] Alejandro Torres-Sánchez, Juan M Vanegas, and Marino Arroyo. Examining the mechanical equilibrium of microscopic stresses in molecular simulations. *Physical review letters*, 114(25):258102, 2015. 60

[TYS09] Yuanqiang Tan, Dongmin Yang, and Yong Sheng. Discrete element method (dem) modeling of fracture and damage in the machining process of polycrystalline sic. *Journal of the European ceramic society*, 29(6):1029–1037, 2009. 29

[WC17] Min Wang and Ping Cao. Calibrating the micromechanical parameters of the PFC2D (3D) models using the improved simulated annealing algorithm. *Mathematical Problems in Engineering*, 2017, 2017. 50

[Wit91] EA Witmer. Elementary bernoulli-euler beam theory. *MIT Unified Engineering Course Notes, MIT*, 1992:114–164, 1991. 58

[WJK+04] QZ Wang, XM Jia, SQ Kou, ZX Zhang, and P-A Lindqvist. The flattened brazilian disc specimen used for testing elastic modulus, tensile strength and fracture toughness of brittle rocks: analytical and numerical results. *International Journal of Rock Mechanics and Mining Sciences*, 41(2):245–253, 2004. 88

[WKC12] Yan Wang, Pawel Keblinski, and Zhenqian Chen. Viscosity calculation of a nanoparticle suspension confined in nanochannels. *Physical Review E*, 86(3):036313, 2012. 60

[WX16] Shunchuan Wu and Xueliang Xu. A study of three intrinsic problems of the classic discrete element method using flat-joint model. *Rock Mechanics and Rock Engineering*, 49(5):1813–1830, 2016. 29

[YF06] Edwige Yeugo-Fogaing. *Caractérisation à haute température des propriétés d'élasticité de réfractaires électrofondus et de bétons réfractaires*. PhD thesis, Limoges, 2006. 15

[YJL06] Budong Yang, Yue Jiao, and Shuting Lei. A study on the effects of microparameters on macroproperties for specimens created by bonded particles. *Engineering Computations*, 23(6):607–631, 2006. 69

[ZH15] Tingting Zhou and Chuanzhen Huang. Simulation of crack propagation in single phase ceramic tool materials. *Computational Materials Science*, 104:177–184, 2015. 29

[Zho03] Min Zhou. A new look at the atomic level virial stress: on continuum-molecular system equivalence. *Proceedings of the Royal Society of London. Series A: Mathematical, Physical and Engineering Sciences*, 459(2037):2347–2392, September 2003. 60

[ZYR$^+$18] Gao-Feng Zhao, Qiuyue Yin, Adrian R. Russell, Yingchun Li, Wei Wu, and Qin Li. On the linear elastic responses of the 2d bonded discrete element model. *International Journal for Numerical and Analytical Methods in Geomechanics*, 0(0), 2018. 48

Abstract: The present thesis aimed at investigating the relationships between the microstructure of refractories and their thermomechanical properties in order to increase their thermal shock resistance. In particular, numerical modeling were carried out in order to better understand the design of microstructure involving damages due to thermal expansion mismatch during processing. For this purpose, experimental results on simplified materials were used as reference for this numerical approach. In order to obtain quantitative results of complex phenomena, new developments of an existing discrete element modeling platform, namely *GranOO*, were carried out. More specifically, direct calibration method of input parameters and improvement of virial stress concept were proposed. This DEM approach was then applied to reproduce thermal damages during cooling of simplified materials and to examine their effects on macroscopic properties. The obtained DEM results of evolution of Young's modulus and thermal expansion coefficient as a function of temperature exhibited similar tendencies with experimental results.

Keywords: Discrete Element Method, refractory materials, thermal shock resistance, micro-cracking, thermal expansion mismatch.

Résumé : Cette thèse avait pour objectif d'étudier les relations entre la microstructure de matériaux réfractaires et leurs propriétés thermomécaniques afin d'améliorer leur résistance aux chocs thermiques. En particulier, des modélisations numériques ont été réalisées afin de mieux comprendre la conception de la microstructure liée à des endommagements dus au différentiel de dilatation thermique. A cette fin, des résultats expérimentaux de matériaux simplifiés ont été utilisés comme référence pour l'approche numérique. Afin d'obtenir des résultats quantitatifs des phénomènes d'endommagement complexes, de nouveaux développements ont été apportés à une plate-forme de modélisation d'éléments discrets existante, nommée *GranOO*. Entre autre, une méthode de calibration direct des paramètres locaux ainsi une amélioration du concept de contrainte viriel ont été proposées. Ensuite, l'approche DEM a été appliquée afin de reproduire les endommagement thermiques lors du refroidissement des matériaux simplifiés et d'examiner leurs effets sur les propriétés apparentes. Les résultats obtenus de l'évolution du module de Young et du coefficient de dilatation thermique en fonction de température ont montré des tendances similaires avec les résultats expérimentaux.

Mots clés : Méthode des Éléments Discrets, matériaux réfractaires, résistance au choc thermique, micro-fissuration, différentiel de dilation thermique.